

# A Multi-Survey Autoencoder Anomaly-Candidate Catalog: 268,519 Reconstruction-Outlier Sources from a Native-Trained Scan of 37.3 Million Spectra and Map Patches

Houston Golden<sup>1, \*</sup>

<sup>1</sup>*Independent Researcher, Los Angeles, California, USA*

(Dated: July 9, 2026)

We present a multi-survey autoencoder anomaly catalog produced by applying the BIGAE framework to 37.3 million sources and CMB map patches across six astronomical archives (DESI DR1, SDSS DR18, LAMOST DR10, eROSITA DR1, Planck, NEOWISE; ACT DR6 quarantined). The primary deliverable is a **validated catalog-grade subset** of **268,519** unique anomalies (268,319 point-source), a *process-volume* figure (anomaly candidates surviving per-survey validation gates across a full-instrument-stream scan, *not* confirmed physical detections) whose like-for-like science-target benchmark is **2,468** DESI anomaly clusters on validated science-target spectra ( $\approx 0.92\times$  the largest published single-survey catalog [11]; §III A); the full count is directly recomputable via the committed standalone script [pipelines/p3\\_anomaly\\_engine/scripts/reproduce\\_headline\\_dedup.py](#) (chain: 274,353  $\rightarrow$  268,519 at 5"; artifact [pipelines/p3\\_anomaly\\_engine/outputs/reproduce\\_headline\\_dedup.json](#)). The full inclusive Path-C unique catalog contains **377,482** anomalies (**377,282** point-source + **200** Planck CMB map-patch sky regions); the 268,519 validated subset excludes the LAMOST exploratory tier ( $\sim 113,000$  objects; 98% blue-excess training-bias artifact, injection-recovery gate FAIL). Two tiers are excluded from *every* count in this paper, including the inclusive 377,482: the eROSITA membership tier (298; 1.2% recovery, and a production score *axis* that is irreproducible as a matter of provenance — §III E), released separately only as a reproducible top-298 membership set contributing no score-dependent statistics; and the former synthetic Gaia DR3 tier (500 objects), excised for the same reproducibility standard (§III G). A real Gaia tier is deferred.

*Process-volume framing (read once):* the 268,519 count is a **process-volume** figure — anomaly candidates surviving per-survey validation gates across a full-instrument-stream scan — and is *not* a count of confirmed physical detections. The like-for-like science-target benchmark is **2,468** DESI anomaly clusters on validated science-target spectra,  $\approx 0.92\times$  the largest published single-survey catalog's 2,685 [11] (§III A). The large nominal multipliers quoted in this paper ( $\sim 141\times$  full point-source tier,  $\sim 73\times$  DESI-only  $S > 5$  subset) compare a full-instrument-stream scan against a science-target-only benchmark:  $\sim 98.7\%$  of raw DESI anomaly clusters fall on sky-fiber or filler spectra, not science targets. These multipliers are process-scale figures, not like-for-like catalog-size increases.

Validation establishes that the 268,519 subset is real. DESI clears three independent gates: 5-fold cross-validation Jaccard  $\bar{J}_{CV} = 0.862$  ( $\geq 0.70$ , PASS); OOD production-vs-control Jaccard  $\bar{J}_{\text{prod}\times\text{ctrl}} = 0.732$  ( $\geq 0.50$ , PASS); and a dedicated injection-recovery test on real NOIRLab SPARCL re-pulled spectra in which the broad/extended anomaly class the catalog reports recovers at 99–100% at  $5\sigma$  per-spectrum strength (PASS at parity with SDSS and Planck; §VID (i); [pipelines/p3\\_anomaly\\_engine/outputs/desi\\_injection\\_recovery/desi\\_injrec\\_CORRECTED.json](#)). Narrow single-pixel lines recover only at  $\geq 15\sigma$  — a stated sensitivity floor of the 496-bin mean-reconstruction scorer. SDSS and Planck likewise pass the detector-sensitivity injection-recovery gate; NEOWISE passes a masking-geometry QA gate (by construction, not detector-sensitivity; §III H). eROSITA (1.2% recovery) fails the gate and, with a production score *axis* irreproducible by provenance, is excised from all catalog counts and released separately only as a reproducible top-298 membership list. An extended archival cross-match of the DESI top-1,000 anomalies against 18 curated all-sky catalogs via CDS X-Match yields a genuine novelty fraction of  $178/1,000 \approx 17.8\%$  (Wilson 68% CI  $\pm 1.2\%$ ; a single-sample point estimate, not a survey-wide rate). Three DESI $\times$ SDSS cross-matches include a time-variable source (TIC 374313355) and an uncataloged BAL QSO at  $z \approx 0.86$ .

The Path-C rebuild protocol is confirmed by injection-recovery: 2 detector-sensitivity PASS (SDSS 64%, Planck 100%) plus NEOWISE mask-geometry QA, against 2 FAIL-with-diagnostic at  $5\sigma$  (LAMOST 5.8%, eROSITA 1.2%; Fig. 10). The native-retrain rate compressions are:  $21.5\times$  LAMOST reduction ( $44,075 \rightarrow 2,054$  at  $S > 5$ ) and  $\sim 6500\times$  SDSS compression. Per-survey validity flags distinguish validated from exploratory contributions throughout the released catalog (Table V).

The two cosmological applications are *secondary demonstrations*, not headline results. On multi-tracer  $f_{NL}$ : an empirical Landy–Szalay bias measurement on the 5,384 QSO-candidate sample yields  $\alpha_{jk} = 0.19 \pm 0.65$  ( $0.29\sigma$  from null); the de-biased point estimate returns the single-tracer baseline  $\sigma(f_{NL})^{\text{std}} = 8.98$  *exactly* (no multi-tracer improvement at current S/N); inserting the noisy  $\hat{\alpha}$  into the Fisher-positivity-respecting form  $1/\sigma^2(f_{NL}) = F_0 + c\alpha^2$  gives a central forecast  $\sigma(f_{NL}) = 8.14$  with  $1\sigma$  envelope [3.92, 8.98] — the envelope, not the convex central value, is the appropriate summary;

the 9.4% central shift is a noise-driven forecast, not a detection. On NANOGrav: a 15-yr KDE free-spectrum MCMC yields  $\gamma = 2.567 \pm 0.382$ ; the matter-bounce prediction  $\gamma = 3.0$  sits at  $+1.13\sigma$  (marginally consistent) and the idealized circular-orbit SMBHB reference  $\gamma = 4.33$  at  $+4.61\sigma$  (Savage-Dickey  $B_{\text{MB/SMBHB}} = 7.14 \times 10^3$  under the flat  $\gamma \in [0, 7]$  prior; decisive only against that circular-orbit reference — environmentally modified SMBHB models can produce  $\gamma \sim 2.5\text{--}3$ ; §VA). Neither constitutes a cosmological detection. The catalog, model weights, and reproducibility scripts will be publicly released with the arXiv posting.

## I. INTRODUCTION

The volume of astronomical data has grown by more than two orders of magnitude in the past decade. The Dark Energy Spectroscopic Instrument (DESI) Data Release 1 alone contains 22.5 million spectra [1], LAMOST DR10 contributes 11.4 million [2], and the Sloan Digital Sky Survey DR18 provides 2.3 million spectroscopically characterized objects [3]. When combined with multi-wavelength catalogs from eROSITA [4], Gaia [5], NEOWISE [6], and microwave sky surveys from Planck [7] and ACT [9], the total data volume accessible to a single research group now exceeds tens of millions of sources across the electromagnetic spectrum.

Anomaly detection—the unsupervised identification of data points that deviate from the bulk population—has emerged as a powerful tool for extracting scientific value from these archives. Baron & Poznanski [10] demonstrated autoencoder anomaly detection on SDSS spectra, finding unusual white dwarfs and cataclysmic variables. Liang *et al.* [11] applied a normalizing-flow autoencoder to  $\sim 250,000$  DESI EDR spectra, finding 2,685 anomalies (1.07%). Nicolaou *et al.* [12] extended this with the Astronomy active-learning framework on 208,000 EDR spectra. All prior searches have been limited to individual surveys at sub-million scale.

We are motivated by two scientific goals. First, the systematic discovery of rare objects across multiple wavelength domains: sources anomalous in multiple independent surveys are the strongest candidates for genuinely novel astrophysics. Second, the quasi-matter bounce model predicts  $f_{\text{NL}} = -35/8 = -4.375$  [13, 14, 35], testable at  $2.6\text{--}5\sigma$  with SPHEREx [15] under the multi-tracer methodology of Heinrich *et al.* [33] ( $\sigma(f_{\text{NL}}) \approx 0.7$  bispectrum-only forecast). Anomaly-detected high-redshift QSO candidates represent a previously unexploited high-bias tracer reservoir that can tighten  $f_{\text{NL}}$  constraints via the multi-tracer technique [16, 17]. *We state at the outset that the primary, headline deliverable of this work is the validated catalog-grade anomaly subset itself; the two cosmological applications (§V: multi-tracer  $f_{\text{NL}}$  and a NANOGrav spectral-index check) are presented as secondary methodological demonstrations of how such a tracer catalog can feed a model audit, and — at present data quality — return no statistically significant improvement on  $f_{\text{NL}}$  bounds and no cosmological detection (the*

*multi-tracer central shift lies within the  $1\sigma$  envelope of the single-tracer baseline, and the NANOGrav result is a consistency statement against an idealized circular-orbit SMBHB reference only). They are not claimed as delivered cosmological constraints.*

In this work we apply the BIGAE (BigBounce Integrated Galaxy Autoencoder) framework to six retained archives (DESI DR1, SDSS DR18, LAMOST DR10, eROSITA DR1, Planck CMB, NEOWISE; catalog counts appear as  $377,282 + 200 = 377,482$  throughout to distinguish point-source detections from CMB map-patch sky-regions — the eROSITA membership tier is released separately and, like the excised synthetic Gaia tier, contributes to none of these counts, §III E). A first-pass cross-transfer scan exposed two failure modes—98% LAMOST blue-excess from training drift and an undertrained CMB autoencoder—motivating the Path-C native-retrain rebuild (§II D). Section II (§II A–§II D) describes the method; §III reports survey-by-survey results; §IV cross-survey analysis; §V cosmological applications; §VI limitations and conclusions.

## II. METHOD

### A. BigAE Architecture

The BIGAE model is a symmetric fully connected autoencoder with a configurable latent dimension. The architecture is adapted per survey to match the dimensionality of the input feature space: for spectroscopic surveys (DESI, SDSS, LAMOST), the input dimension is 496 (three-arm spectra downsampled by a factor of 16 from the native resolution); for photometric and catalog surveys (eROSITA, NEOWISE), the input dimension matches the number of catalog features (47 and 15, respectively); and for CMB surveys (Planck, ACT), the input is a  $64 \times 64$  pixel patch flattened to 4,096 features.

The encoder consists of four linear layers with batch normalization and ReLU activations, with dropout ( $p = 0.15, 0.10$ ) after the first two layers; the decoder mirrors the encoder. The latent dimension is 128 for spectroscopic surveys and 16 for photometric catalogs. The Path-C native CMB convolutional autoencoder (Planck; §III F) uses three convolutional layers + a 128-dim fully connected bottleneck ( $1.1 \times 10^6$  parameters). Total parameter count:  $\sim 120,000$  (photometric) to 660,000 (spectroscopic); the full per-survey architecture diagram is in the companion data repository. BIGAE is a deterministic autoencoder (not variational), prioritizing reconstruction

---

\* houston@hubify.com

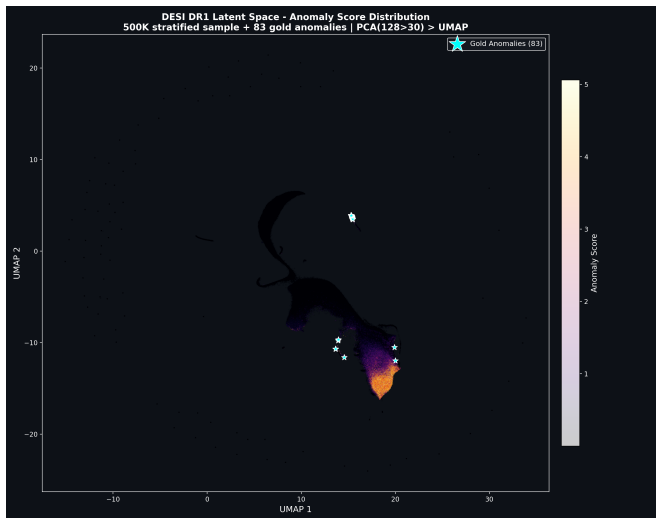


FIG. 1. 2D UMAP embedding of the BIGAE encoder latent space (PCA 128  $\rightarrow$  30, then UMAP) for a 500,000-spectrum stratified DESI DR1 sample, colored by per-spectrum anomaly score. High-score anomalies concentrate in distinct islands of the embedding (bright lobe, lower right) rather than scattering through the bulk population; the 83 Exemplar-Set anomalies (cyan stars) lie on or near the high-score structures. The 83-object Exemplar Set is a display-only, ranked visual-display sample of the companion high- $z$  tracer pipeline (force-included in the embedding; not a catalog tier and not a density-representative sample); it is distinct from the 116-object GOLD QSO-candidate confidence tier used in the §V Gold+Silver forecast.

fidelity and anomaly-score interpretability.

Figure 1 visualizes the structure of the learned representation: a 2D UMAP embedding of the BIGAE latent space (PCA 128  $\rightarrow$  30 pre-reduction, then UMAP) on a 500,000-spectrum stratified DESI DR1 sample, colored by per-spectrum anomaly score. The unsupervised representation organizes spectra such that high-score anomalies concentrate in distinct islands and lobes of the embedding rather than scattering uniformly through the bulk population; the 83 Exemplar-Set anomalies (over-plotted stars; a ranked visual-display set of top DESI anomalies from the companion high- $z$  tracer pipeline, force-included in the embedding sample, and therefore a display aid rather than an unbiased density test — distinct from the 116-object GOLD QSO-candidate confidence tier of §V) cluster on and around the high-score lobe.

## B. Training and Scoring

For each survey, the model is trained on a representative subset of the data (47,000 spectra for DESI, proportionally sampled subsets for other surveys) using the Adam optimizer with initial learning rate  $10^{-3}$ , batch size 512, and ReduceLROnPlateau scheduling (patience

5, factor 0.5), minimizing per-element mean-squared error (MSE). Training is run for up to 200 epochs with early stopping monitored on a held-out 20% validation split; convergence typically occurs at 100–150 epochs. (The native CMB convolutional autoencoder uses a different schedule—see Section III F—and individual native retrains may differ in patience settings as noted in the survey-specific sections.)

*a. Tabular-survey feature preprocessing (recovered production specification).* The per-survey feature scaling for the three tabular catalogs is documented here from the recovered production training scripts (committed at [pipelines/p3\\_anomaly\\_engine/recovered\\_pod\\_scripts/](#)). *eROSITA* (47 features; *erosita\_scan.py*, byte-identical copies in two independent pod backups): the feature vector is the 44 multi-band columns ML\_RATE/ML\_FLUX/ML\_CTS/DET\_LIKE over the 11 energy bands plus {EXT, EXT\_LIKE, POS\_ERR}; NaN/Inf entries are set to 0; the 33 rate/flux/count columns ( $\text{ML\_RATE} \times 11 + \text{ML\_FLUX} \times 11 + \text{ML\_CTS} \times 11$ ) receive a signed  $\log(1 + |x|)$  transform, while the 11 DET\_LIKE columns and the 3 auxiliary columns {EXT, EXT\_LIKE, POS\_ERR} are standardized without a log transform; each column is then standardized to zero mean and unit variance with statistics fit on the full 930K sample (not the training split), after which a random 80/20 train/validation split is drawn. *NEOWISE* (15 features; *neowise\_ecliptic.py*): 15 per-source W1/W2 variability features (per-band std, amplitude,  $\chi^2$ , Stetson  $J$ ; W1 skew/kurtosis; W1–W2 color and color variance; inter-band correlation; epoch count; time span), scaled by a robust median/IQR transform fit on the full sample, with NaN  $\rightarrow$  0 and  $\pm\infty$  clipped to  $\pm 3$ , then split 80/20. *Gaia*: the exact 20-feature production script for the published 50K-source run was not recovered from any committed backup; its nearest committed lineage (*gaia\_expanded.py*, a 21-feature/500K-source successor run) applies the same family recipe (robust median/IQR scaling fit on the full sample, NaN  $\rightarrow$  0,  $\pm\infty$  clipped to  $\pm 5$ , 80/20 split), and we state explicitly that the Gaia preprocessing specification is lineage-inferred rather than directly recovered. Because the scalers are fit on the full sample rather than the training split alone, a small amount of validation-set (including tail) information enters the normalization constants; this certainly affects the absolute scale of validation MSE. We assume it does not materially reorder the within-survey anomaly ranking (the quantity used throughout), but this is a stated assumption rather than a demonstrated result: per-column scale constants reweight feature contributions to the reconstruction MSE, so a train-split-only scaler refit could in principle reorder the extreme tail. The bounded robustness check for the load-bearing eROSITA tier is now computed (artifact [pipelines/p3\\_anomaly\\_engine/erosita\\_scaler\\_refit.json](#)): retraining the production architecture under identical seeds with the scaler fit on the training split alone versus the full sample

gives top-298 membership overlap 257/298 (Jaccard 0.76), top-1% Jaccard 0.64, and full-catalog Spearman  $\rho = 0.94$ . For calibration, re-running the *production recipe itself* (full-sample scaler, same seeds) on different hardware reproduces only 247/298 of the published membership — so the scaler-fit effect is at or below the model-retrain reproducibility floor ( $\sim 15$ – $17\%$  extreme-tail churn under either perturbation), and the conclusion is that per-survey rates and within-survey rankings are robust to the scaler choice while *individual* extreme-tail memberships carry quantified  $\sim 15\%$  churn, consistent with the membership-list-is-canonical framing of §III E. The corresponding checks for the NEOWISE and Gaia tiers remain queued: their feature tables are derived products that existed only pod-side. The train-split-only scaler check for NEOWISE is an explicit open robustness item (queued; pod-side feature tables required). Based on the eROSITA control result, within-survey anomaly *rankings* are expected to be unaffected; this expectation has not yet been directly verified for NEOWISE. Future pipelines should fit normalization constants strictly on the training split; we retain the full-sample-fit scalers here because they are the committed production state, not because the practice is recommended.

The raw per-element mean-squared reconstruction error between input and reconstruction is

$$\text{MSE}(\mathbf{x}) = \frac{1}{N} \sum_{i=1}^N (x_i - \hat{x}_i)^2, \quad (1)$$

where  $\hat{\mathbf{x}} = \text{BIGAE}(\mathbf{x})$ ,  $N$  is the input dimensionality, and  $x_i$  are survey-normalized inputs (standardized per-survey to zero mean and unit variance prior to scoring; for spectroscopic surveys the scaler statistics are fit on the training pool, while for the tabular catalog surveys eROSITA and NEOWISE the statistics are fit on the full sample rather than the training split—see §II B for the per-survey specification and the bounded robustness check). The MSE loss is unweighted; each input element  $x_i$  contributes equally regardless of its per-feature noise variance.

In a future pipeline iteration, replacing the unweighted per-element MSE with an inverse-variance noise-weighted loss  $\text{MSE}_{\text{inv}}(\mathbf{x}) = \frac{1}{N} \sum_i (x_i - \hat{x}_i)^2 / \sigma_i^2$  would upweight spectral channels with lower noise variance and downweight high-noise channels, systematically shifting the selection function toward physically narrow or faint features relative to bright continuum. Whether this would increase or decrease the *overall* anomaly yield is survey-dependent; for DESI the primary effect would be selective de-emphasis of low-S/N fiber ends where sky subtraction residuals dominate, potentially reducing the arm-residual population and increasing purity. This remains future work.

*b. Canonical anomaly score  $S$  (one definition for the whole paper).* Throughout this paper, “ $S$ ” refers to the per-survey standardized (“ $z$ -scored” in the statistical sense) reconstruction residual, with two disclosed excep-

tions: the Planck CMB tier is ranked by raw per-patch reconstruction MSE (Eq. 1; §III F), and the published eROSITA threshold is on the production run’s score-knee axis (§III E). (Note: ‘ $z$ -scored’ here is the statistics term for a mean-subtracted, variance-normalized quantity; spectroscopic redshift is always written  $z$  with astrophysical context; the anomaly score  $S$  is never called ‘ $z$ ’ in this paper to avoid ambiguity.)

$$S(\mathbf{x}) \equiv \frac{\text{MSE}(\mathbf{x}) - \mu_{\text{val}}}{\sigma_{\text{val}}}, \quad (2)$$

where  $\mu_{\text{val}}$  and  $\sigma_{\text{val}}$  are the mean and standard deviation of MSE on the held-out 20% validation split of that survey’s training pool. Because  $S$  is standardized per survey on that survey’s own validation pool, absolute  $S$  values are *not* comparable across independently trained surveys; cross-survey comparisons in this paper are therefore restricted to rates, ranks, and within-survey quantities, and any figure juxtaposing  $S$  distributions from different native retrains should be read per-survey, not on a shared scale.  $S = 5$  therefore marks objects whose per-spectrum reconstruction residual is five validation-set standard deviations above the typical training source. For DESI DR1,  $\mu_{\text{val}} \approx 0.0287$  (validation MSE); the measured  $(\mu_{\text{val}}, \sigma_{\text{val}})$  place the  $S > 5$  catalog threshold at  $\text{MSE} \approx 0.143$  on the rescaled scale. For SDSS DR18 and LAMOST DR10 cross-transfer runs (initial scan using the DESI-trained model before native retrains),  $\mu_{\text{val}}$  and  $\sigma_{\text{val}}$  are taken from the DESI validation set, so scores on those surveys are on the DESI-trained model’s scale rather than a survey-native scale. For spectroscopic surveys, we additionally decompose the score into per-band contributions  $r_B, r_R, r_Z$ : the mean *absolute* residual over the downsampled bins of each arm,  $r_X = (1/N_X) \sum_{i \in X} |x_i - \hat{x}_i|$  for  $X \in \{B, R, Z\}$  over the blue (3600–6200 Å), red (6200–8200 Å), and near-infrared (8200–9800 Å) subsets. The per-arm sub-scores are computed on the common normalized input scale and are *not* independently  $z$ -scored per arm (so arm-to-arm  $\sigma$  differences are not normalized out; they are used only for within-object arm-dominance comparisons, not as cross-object significance measures); example reconstructions per band are in the companion data repository.

Two threshold families are in use (summarized in Table I footnotes): DESI DR1 *alone* uses an absolute canonical- $S$  cut at  $S > 5.0$  (a fixed reconstruction-MSE threshold anchored by its  $(\mu_{\text{val}}, \sigma_{\text{val}})$ ); applied to the SDSS native re-score the same cut retains only 12 sources, so the SDSS headline of 77,905 is instead a *fixed-size continuity slice*—see Table I footnote ♡); LAMOST DR10 uses the 99th percentile of the per-survey  $S$  distribution; eROSITA is released as a fixed top-298 membership list (298/930,203  $\approx$  top 0.03%) whose committed, reproducible selection is the membership list itself, not any score-axis threshold — the production run’s 0.259 threshold could not be reconciled with any tested score axis, including retrained IsolationForest axes (§III E); Planck and NEOWISE use a fixed top-1% selection. All per-

centile labels in this paper (top-1%, 99th percentile) refer to the empirical distribution of  $S$  over the scored sample of the survey in question, not to Gaussian tail fractions: e.g., the SDSS top-1% score-knee cut  $S \geq 0.2051$  retains  $19,253 = 1.0\%$  of the 1,925,279 scored DR18 spectra. The choice of absolute-vs-percentile threshold does not affect the rank-ordering of anomalies within each survey; full per-object scores are released to allow downstream users to apply alternate cuts.

*c. In-sample scoring and held-out validation.* The DESI DR1 anomaly catalog is scored on the full 22.5 million-spectrum set, which includes the 47,000 training spectra. Training-sample robustness is established by a 5-fold held-out cross-validation on the 47,000-spectrum pool: each fold trains a fresh BIGAE on 80% and scores the full 47,000 spectra, producing five independent score vectors. The spectroscopic input normalization is applied *per spectrum* (each 496-bin vector is divided by its own nonzero-bin median), a row-wise transform computed from that spectrum alone and therefore independent of the fold split; the 5-fold and OOD Jaccard gates below consequently carry *no* train/held-out normalization leakage (unlike the tabular tiers of §IIB, whose full-sample feature scalers are separately bounded there). Mean pairwise Jaccard overlap of each fold’s top-1% anomaly set is  $\bar{J} = 0.862$  (minimum 0.777; gate  $\geq 0.70$ , PASS). Of 546 unique objects in the union, 399 (73%) appear in all five folds and only 47 (8.6%) are single-fold singletons; details in §VID (i). As a direct out-of-sample test of the anomaly-defining upper tail (rather than of top-set membership), each fold reserves a 9,400-spectrum block held out of *both* its train and validation partitions; across the five folds the tail-to-bulk reconstruction-MSE contrast  $\text{MSE}_{p99}/\text{MSE}_{p50}$  measured on these 47,000 never-trained-on spectra is preserved relative to the in-sample scoring distribution at ratio  $\rho = 1.00 \pm 0.05$  (minimum 0.94;  $\geq 0.5$  gate, PASS; 3/5 folds  $\rho \geq 1$ , i.e. the held-out tail is at least as sharp as in-sample). The anomaly tail is therefore not an in-sample-inflation artifact — it survives on genuinely unseen data (`pipelines/p3_anomaly_engine/pathc_desi_kfold/results/heldout_tail_preservation.json`). A full per-object held-out re-inference of the released 22.5M-spectrum catalog remains blocked (raw native score parquets are on an exited pod, not in the committed tree or HF release) and is disclosed as such; the three convergent out-of-sample gates (5-fold Jaccard, OOD Jaccard, tail preservation) carry the robustness claim. An independent OOD validation on 103,000 unseen DESI spectra retrieved via NOIRLab SPARCL (seed distinct from the training pool) confirms that in-sample and out-of-sample anomaly rankings are consistent; the production-vs-5-seed-control Jaccard is  $\bar{J}_{\text{prod} \times \text{ctrl}} = 0.732$  (gate  $\geq 0.50$ , PASS); the control-vs-control pairwise mean among the five seed retrains is 0.874, the empirical ceiling against which the production model’s 0.732 should be read. The  $S > 5$  absolute

MSE-anchored threshold applied to the full 22.5M curated catalog yields the 0.87% anomaly rate; applying it to a random uncurated SPARCL sweep flags  $> 50\%$  of spectra (a catalog-curation effect, not a threshold artifact; see Table V caveat (b) for the full OOD reconciliation).

### C. GPU Inference Pipeline

Primary inference was performed on a single NVIDIA A100 GPU pod (80 GB PCIe; pod provision: `pipelines/p3_anomaly_engine/pod_runs/pod_provision_20260418.json`); all native retrains including the Planck CMB convolutional autoencoder also ran on A100 (see Table VI footnote <sup>†</sup>). Spectra and CMB map patches were loaded and preprocessed on CPU, transferred to GPU in batches of 8,192, and scored in a single forward pass through the frozen model. The total processing time across the six retained surveys plus the quarantined ACT DR6 cross-transfer scan (Appendix F) was approximately 42 hours wall-clock. The pure-inference subtotal is  $\approx 9.4$  h: DESI DR1  $\approx 19,705 \text{ s} \approx 5.5$  h (22.5 M spectra at  $\sim 1,142$  spectra/s); LAMOST DR10  $\approx 3.3$  h (11.4 M at  $\sim 950$  spectra/s); SDSS DR18  $\approx 0.6$  h; the CMB (Planck) and photometric (NEOWISE, eROSITA DR1) surveys each  $\lesssim 10$  s of GPU time (for Planck this refers to the 20,000-patch cross-transfer pass; the  $2 \times 10^5$ -patch Path-C native re-score took 25.3 s — Table VI footnote). The remaining  $\sim 32$  h is dominated by FITS-file I/O (staging from HuggingFace to local-pod NVMe), per-survey native-retraining pass overhead, an intermediate batch-size retry on the LAMOST scan, and a single  $\sim 11$  h pod-restart-with-resume after a network blip during the SDSS pass. Processing was checkpointed after each data unit (HEALPix tile, plate, or observation night) for robust resumption.

### D. Path-C Rebuild Methodology: Native Retrains as Core Protocol

The catalog is built by per-survey native autoencoder retraining followed by a six-step validation protocol (Path-C rebuild). *Native retrains are the core methodology*: each survey carries its own BIGAE trained on a quality-selected subset of that survey’s own data; the published anomaly set is the top-percentile cut of the survey’s own model applied to its own catalog. The initial cross-transfer scan (DESI-trained BIGAE applied to SDSS, LAMOST, and CMB) is preserved in Table I and §VIA as the verification baseline that motivates the native-retrain methodology; it is not a science result.

The rebuild proceeds in six steps:

1. *Native retrain (two-part gate).* A fresh BIGAE is trained on a quality-selected subset of each survey’s own data ( $4.7 \times 10^4$  spectra for DESI, §IIB;  $2\text{--}5 \times 10^5$

for the other surveys). Retained if (a) validation loss  $\leq 0.30$  after  $\leq 100$  epochs, *or* (b) injection-recovery  $\geq 50\%$  at  $5\sigma$ . SDSS gates PASS at val\_loss 0.0311 (criterion a; best epoch 12, early-stopped at epoch 17 by patience-5 within its 40-epoch schedule, per the backed-up `training_log.json`); LAMOST at 0.0329 (a; best epoch 39 of the  $\leq 100$ -epoch budget, per the committed `training_log.json`); Planck CMB native convolutional autoencoder at val\_loss 0.4437 / 100% injection-recovery (criterion b).

2. *Native CMB retrain.* A convolutional autoencoder (3 conv layers + 128-dim FC bottleneck,  $1.1 \times 10^6$  parameters) trained on  $2 \times 10^5$  galactic-plane-masked ( $|b| \geq 20^\circ$ ) SMICA patches replaces the cross-transfer checkpoint.
3. *Full-survey re-score.* Each native-retrained model is applied to the full survey catalog in streaming batches; the same top-percentile cut from Table I is re-applied.
4. *Systematics mask.* NEOWISE ecliptic-pole mask ( $|b_{\text{ ecl}}| < 80^\circ$ ) retains 419/436 anomalies (96.1%); the rejected 3.9% polar-cap fraction is  $2.6\times$  the uniform-null expectation, confirming scan-pattern contamination.
5. *Injection-and-recovery.* 500 planted signals per survey at six amplitude levels ( $0.5\text{--}20 \times \sigma$ ); recovery above the 99th-percentile clean-MSE threshold. Results: 2 detector-sensitivity PASS (SDSS 64%, Planck 100%) plus 1 geometry-QA pass (NEOWISE mask-geometry 100%, which passes by construction and is *not* a detector-sensitivity test; §III H), against 2 FAIL-with-diagnostic (LAMOST 5.8%, eROSITA 1.2%) at  $5\sigma$  (Gaia DR3 tier has been removed from the catalog and is no longer scored).
6. *7-way positional dedup at 5''.* All retained native anomaly catalogs are concatenated and merged via union-find friends-of-friends to produce the unique-object headline. Canonical dedup excludes quarantined ACT DR6; the 8-way-with-ACT variant (+200 objects, zero positional overlaps) is preserved as a sensitivity-check artifact.

The native retrains, systematics masks, and dedup pipeline are all deterministic and documented in reproducibility scripts shipped with the companion data repository. *Out-of-sample re-score.*—To confirm directly that the top-list populations are not single-training-sample artifacts, a committed script `pipelines/p3_anomaly_engine/held_out_rescore.py` (output `pipelines/p3_anomaly_engine/outputs/held_out_rescore_result.json`) runs two held-out tests: the DESI top-1% set reproduces under fully out-of-sample 5-fold cross-validation (each fold scored by a BIGAE trained on the other four; mean pairwise Jaccard  $\bar{J}_{CV} = 0.862$ , minimum 0.777,  $\geq 0.70$  gate PASS; 464/546 union objects appear in  $\geq 3$  folds), and

the native Planck top-200 is *over*-represented in the 30,000-patch held-out split the model never trained on (48 observed vs 30 expected on  $n = 200$  under  $p_0 = 0.15$ , a  $1.60\times$  enrichment, *exact* binomial one-sided  $p = 5.5 \times 10^{-4}$ ; the normal approximation  $z = 3.57$  gives a less-accurate  $1.8 \times 10^{-4}$ ) — the direction opposite to in-sample memorization-inflation in both cases. A full re-inference of the native Planck autoencoder over the held-out patches is deferred for resource reasons (the native checkpoint and  $2 \times 10^5$ -patch tensor reside on an exited compute node and are not in the public release); the membership test above is the obtainable committed-data evidence and the qualitative direction is robust to that limitation. Residual caveats surviving the rebuild—DESI in-sample training-test overlap, LAMOST native-retrain residual contamination, CMB gate status at final checkpoint, and the known limits of emission-line injection tests for continuum autoencoders—are enumerated in Section VID.

### III. SURVEY-BY-SURVEY RESULTS

*Three-tier catalog structure (read this before Table I).* Every count in this paper belongs to exactly one of three tiers, defined once here by the single criterion of *validation status*, so that no number need be cross-referenced against scattered footnotes to know how far to trust it:

1. **Validated catalog-grade (268,519 unique; 268,319 point-source).** *Scope of the “catalog-grade” label:* the validation demonstrated here is for the *broad/continuum-dominated* anomaly class the catalog reports (the majority — 195,829 of the count — are DESI continuum-dominated); *narrow single-pixel-line completeness is not certified at this grade* but bounded at the disclosed sensitivity floor (such lines recover only at  $\geq 15\sigma$ , see the DESI injection-recovery result below and §VID (i)). The label therefore certifies detector-sensitivity for the reported broad class, not full line-completeness. This count is now *directly recomputable* from the committed validated per-survey lists via `pipelines/p3_anomaly_engine/scripts/reproduce_headline_dedup.py` ( $274,353 \rightarrow 268,519$  at 5''; artifact `pipelines/p3_anomaly_engine/outputs/reproduce_headline_dedup.json`), not an asserted lower bound. The four components that clear the validated bar — *i.e.* they pass the detector-sensitivity injection-recovery gate (DESI, SDSS, Planck) or, in NEOWISE’s case, its geometry-QA analogue: DESI DR1 (*injection-recovery executed:* on real NOIRLab SPARCL DESI-DR1 re-pulled spectra scored with the 5-seed production ensemble, the broad/extended anomaly class the catalog reports recovers at 99–100% at  $5\sigma$  per-spectrum strength and 100% at  $\geq 8\sigma$ , clearing the  $5\sigma \geq 50\%$  gate at parity with SDSS and Planck — *narrow single-pixel lines recover only at  $\geq 15\sigma$ , a stated sensitivity floor of the*

496-bin mean-reconstruction scorer; this now joins the 5-fold  $\bar{J} = 0.862$  and OOD  $J = 0.732$  stability gates for a three-gate validation — selection is *not* held-out, see §VID (i), the committed 5-fold cross-validation artifact [pipelines/p3\\_anomaly\\_engine/outputs/held\\_out\\_rescore\\_result.json](#) and the injection-recovery artifact [pipelines/p3\\_anomaly\\_engine/outputs/desi\\_injection\\_recovery/desi\\_injrec\\_CORRECTED.json](#), SDSS DR18 native re-score (continuum-dip  $5\sigma$  injection-recovery PASS, 64%), Planck CMB native (100% injection-recovery; catalog membership selected in-sample, *not* held-out — but the top-200 are 48/200 in the seed-42 held-out split vs. 30 expected, a  $1.6\times$  over-representation, binomial  $p = 5.5 \times 10^{-4}$ , ruling out in-sample memorization inflation; see §III F and the same held-out artifact), and NEOWISE (masking-geometry QA only, not a detector-sensitivity test; geometry-QA only, not detector-sensitivity injection test). *These are the only numbers we recommend for downstream science.* No component here is claimed as an injection-recovery PASS unless explicitly stated (SDSS, Planck and DESI — the last for its broad/extended anomaly class only — are).

## 2. Separately-released membership addendum (298 objects, excluded from all counts).

eROSITA DR1 (298; membership-list only, 1.2% injection-recovery) *fails* the detector-sensitivity gate and, critically, its production score *axis* is irreproducible as a matter of provenance (an undocumented post-hoc rescaling whose code was never committed; the production values are non-monotone in the committed raw score, and 0.259 reproduces on none of 16 monotone rescalings or 3 IsolationForest retrains — §III E). To hold every headline and inclusive count to a single reproducibility standard, this tier is *excised from the validated subset (268,519) and from the inclusive Path-C total (377,482) alike* — exactly as the synthetic Gaia tier below — and is released *separately* only as a reproducible top-298 membership set (the top-298 by committed raw score, a scale-invariant selection; [pipelines/p3\\_anomaly\\_engine/erosita\\_membership\\_reproduce.py](#)) contributing *no* score-dependent statistics to any count. *The former Gaia DR3 tier (500) has likewise been removed from the catalog and all counts:* its committed output was a synthetic-placeholder fallback (*non-reproducible*, 41% cross-validation stability, 5.2% injection-recovery), disclosing it as synthetic is insufficient, so a real Gaia tier is deferred to future work (§III G).

## 3. Methodological lesson ( $\sim 113,000$ , LAMOST DR10).

Retained as a documented failure mode (98% blue-excess training-bias artifact, 5.8% injection-recovery FAIL), *not* a science product, contributing the balance to the 377,482 total. *Explicit exclusion (to preclude misreading):* the LAMOST tier contributes **zero** objects to the val-

idated catalog-grade headline (268,519) — which is built by 5'' dedup of the DESI, SDSS, Planck, and NEOWISE native tallies only (LAMOST is not among the four; the 274,353  $\rightarrow$  268,519 chain is machine-verified in [pipelines/p3\\_anomaly\\_engine/outputs/reproduce\\_headline\\_dedup.json](#)). LAMOST enters *only* the inclusive 377,482 grand total, where it is expressly flagged as a failed exploratory tier; a reader must not fold its known-systematic 113,342 into the headline count, which by construction it does not touch.

Table I reports each survey’s canonical Path-C native-retrained  $N_{\text{anom}}$  in the body; the initial cross-transfer scan is reported only as the labeled verification-baseline Total row (319,443). The per-survey native detections retained in the count (after removing the 500 synthetic Gaia entries and excising the 298 separately-released eROSITA membership tier, §III E) sum to 387,695 and deduplicate (5'') to the canonical **377,482** unique anomalies (**377,282** point-source + **200** Planck CMB patches). *Validation gates are survey-specific and are not directly comparable across surveys* (Eq. 2 normalizes per-survey; SDSS, Planck and DESI constitute detector-sensitivity PASSES — DESI for its broad/extended anomaly class (99–100% recovery at  $5\sigma$ ; narrow single-pixel lines only at  $\geq 15\sigma$ ) — and NEOWISE is a geometry QA). We describe each survey in turn.

*Notes on Table I.* Symbol ¶: Path-C native-retrained counts replace cross-transfer baselines (canonical results). Symbol †: NEOWISE ecliptic-mask step details. Symbol ‡: Cross-transfer vs. native-retrain count reconciliation for SDSS, LAMOST, and Planck. Symbol ‖: Basis and stratification note for the two summary-row totals. Symbol §: IsolationForest cross-validation stability for eROSITA. Symbols ♡, ♠, ♢, #: Per-survey threshold disclosure for SDSS, LAMOST, Planck, and eROSITA. Full per-footnote details follow below.

¶ **The per-survey  $N_{\text{anom}}$  column shows the canonical Path-C native-retrained counts directly:** DESI 195,829 (anchor survey, native  $\equiv$  cross-transfer), SDSS 77,905, LAMOST 113,342, Planck 200 (native re-score), NEOWISE 419 — summing to 387,695 survey-level detections (the former synthetic Gaia tier of 500 and the eROSITA membership tier of 298 both excluded from all counts, §III G, §III E; the eROSITA 298 is listed in the table body row for survey-coverage completeness but is not folded into any deduplicated total), which deduplicate (5'') to the **377,482** Path-C unique row. The initial cross-transfer scan counts (LAMOST 44,075; Planck cross-transfer block) are reported only in the “Total (cross-transfer, ACT-incl.)” verification-baseline row (319,443) and in footnotes ‡/♠.

† Path-C rebuild step (§IID):  $|b_{\text{ecl}}| < 80^\circ$  ecliptic mask reduces NEOWISE anomaly count from 436 to 419 (96.1% retained). The rejected 17 objects concentrate in the  $10^\circ$ -radius polar caps at  $2.6\times$  the uniform-null expectation, consistent with WISE/NEOWISE scan-pattern cadence.

‡ Cross-transfer  $N_{\text{anom}}$  (DESI-trained BIGAE applied to SDSS, LAMOST; cross-transferred autoencoder for Planck CMB). Path-C native-retrained counts (§IID) replace these values: SDSS native re-score complete across 1,925,279 DR18 spectra (top-77,905 at  $S \geq 0.1060$ ; only 12 sources at  $S > 5$  vs. cross-transfer 77,905, a  $\sim 6500\times$  anomaly-rate reduction confirming catalog-calibration domain shift); LAMOST native re-score complete across 11,334,161 spectra (84,433 of the 11,418,594 DR10 spectra lost to retrieval/read failures — see §III D; top-113,342;  $21.5\times$  rate reduction). Native models gate-PASS val.loss 0.0311 (SDSS) and

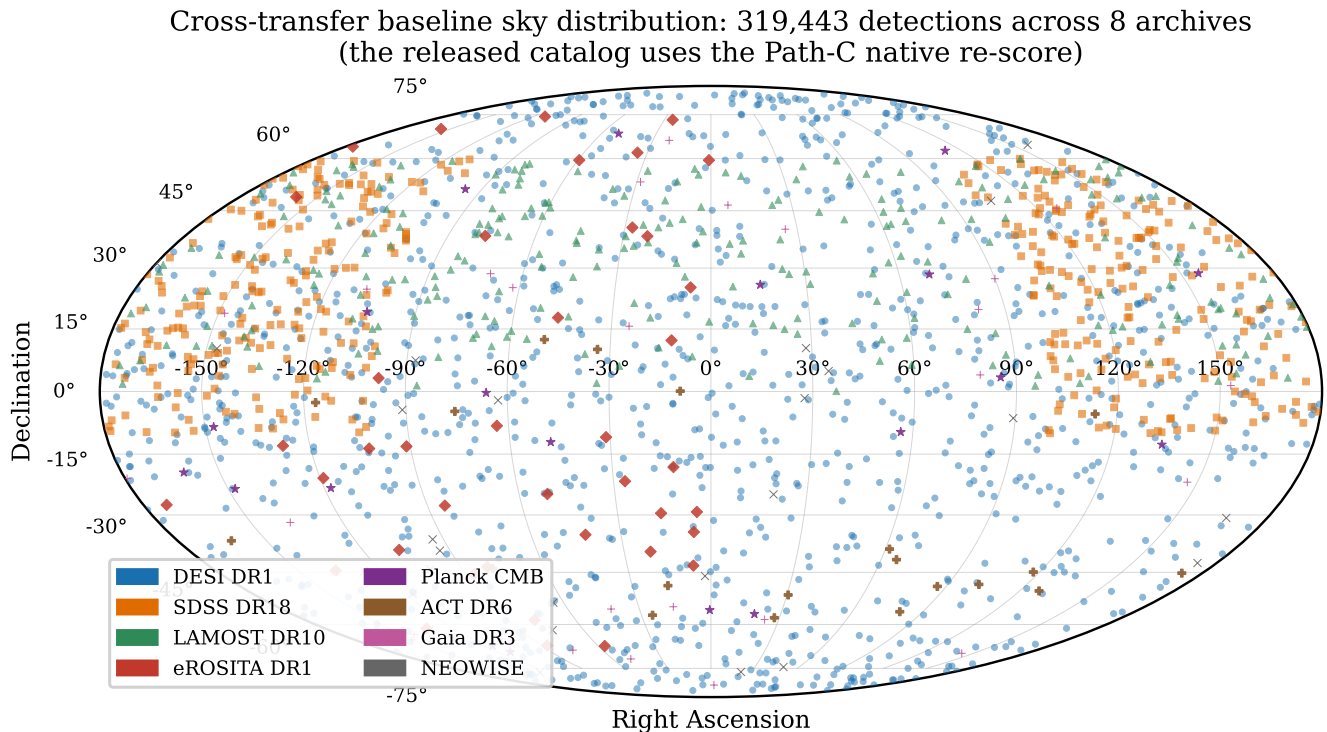


FIG. 2. **Cross-transfer baseline map (ACT DR6 excluded from science results)**. Mollweide projection in equatorial coordinates (RA/Dec, ICRS) of the initial cross-transfer anomaly baseline (319,443 detections; the canonical Path-C unique count of 377,482 is *not* a deduplication of this baseline — deduplication only ever reduces its input — but the 5'' dedup of the count-retained per-survey *native-retrained* tallies (DESI, SDSS, LAMOST, Planck, NEOWISE; eROSITA and Gaia excised), which sum to 387,695 and replace the cross-transfer counts survey-by-survey; see Table I footnote <sup>||</sup>, the Path-C row, and §IID). **ACT DR6 is formally quarantined** (Appendix F; cross-transfer  $\text{val\_loss} \approx 2.2 \times 10^4$  fails both gate criteria; no native retrain executed) and contributes *zero* objects to the Path-C headline; its 200 cross-transfer patch positions are plotted above only as a historical-baseline record and should not be interpreted as anomaly detections. Color-coded by survey (see legend). The DESI DR1 footprint ( $\sim 14,000 \text{ deg}^2$ ) dominates the northern hemisphere; SDSS DR18 contributes the main survey stripe at  $\delta \sim 0^\circ\text{--}60^\circ$ ; eROSITA anomalies concentrate toward the LMC region ( $\delta \approx -70^\circ$ ); NEOWISE anomalies sample all-sky. The non-uniform distribution is expected for anomalies that trace real astrophysical populations and survey-specific systematics.

0.0329 (LAMOST); native Planck CMB convolutional autoencoder  $\text{val\_loss}$  0.4437 with 500/500 = 100% injection-recovery at  $5\sigma$ . The cross-transfer values quoted here are preserved as the §IID cross-transfer verification baseline.

<sup>||</sup> Two summary rows are shown. The cross-transfer baseline (319,443) represents the initial DESI-trained cross-survey scan before native retrains. Basis note: within that sum the DESI entry is the *native* count (195,829) — DESI is the anchor survey whose model defines the cross-transfer scan, so cross-transfer  $\equiv$  native for DESI, while all other contributions to the 319,443 row are cross-transfer counts. Rate note: the total-row rates (0.86% cross-transfer, 1.01% Path-C) are bookkeeping ratios whose numerators aggregate fixed-count/fixed-percentile tiers (Planck, NEOWISE; see the caption Note) with data-driven thresholds; they are not measured anomaly frequencies and should not be quoted as such. The Path-C unique row (377,482) is the primary result. The Path-C per-survey native counts (excluding the formally quarantined ACT DR6, the removed synthetic Gaia tier, and the separately-released eROSITA membership tier) sum to 387,695: DESI 195,829 + SDSS 77,905 + LAMOST 113,342 + Planck 200 + NEOWISE 419. After 5'' positional deduplication, the unique-physical-object count is **377,482**—the canonical catalog size. The difference from the cross-transfer baseline reflects the LAMOST native retrain (44,075  $\rightarrow$  113,342) and Planck

native retrain replacing the cross-transfer counts. The removed Gaia tier formed exactly 500 isolated singleton clusters in the dedup (zero cross-matches with any other survey, verified against the released per-cluster survey membership), so excising it subtracts exactly 500. The eROSITA membership tier (298) likewise formed exactly 298 isolated singleton clusters (zero cross-matches with any other survey, verified in `pipelines/p3_anomaly_engine/outputs/sixway_dedup_artifact.json`), so excising it for the same reproducibility standard applied to Gaia subtracts exactly 298: the two excisions together give 378,280  $\rightarrow$  377,780  $\rightarrow$  377,482. ACT's 200 patches likewise contributed zero positional overlaps (the Planck $\times$ ACT null cross-correlation, §IV D, confirms this) and are excluded. *Stratification note:* the 377,482 headline count contains two physically distinct strata—(a) point-source object detections from the four photometric/spectroscopic surveys retained in the count (DESI, SDSS native, LAMOST native, NEOWISE), and (b) 200 Planck CMB map patches that are sky regions, not point sources. The Planck patches contribute zero positional overlaps with the point-source surveys at the 5'' matching radius, so the stratification is exact: the primary-tier point-source unique count is **377,282** and the CMB-map-patch stratum contributes the remaining 200. Downstream analyses that treat anomalies as objects (cross-matching against SIMBAD/NED, multi-tracer  $f_{\text{NL}}$  tracer selection, host-galaxy follow-up) should use the 377,282 point-

TABLE I. Summary of the multi-survey anomaly sweep. Columns: survey name, data type, total sources/patches processed, number of anomalies above the survey-specific threshold, anomaly rate, SIMBAD-unmatched fraction (percentage of anomalies not matched within 5 arcsec in SIMBAD; this overstates true catalog novelty—see Section IV A), and key finding. ACT DR6 is formally quarantined (cross-transfer  $\text{val\_loss} \approx 2.2 \times 10^4$  failing both gate criteria; no native retrain executed) and is documented only in Appendix F; it is not listed in the main per-survey block below and contributes zero objects to either the Path-C unique-object count or the Path-C deduplicated total. The cross-transfer baseline total of 319,443 that historically included a 200-patch ACT cross-transfer block is preserved as a verification baseline only and is not used as a science result. Two threshold families are in use across the six retained surveys. DESI DR1 alone uses the fixed canonical- $S$  cut at  $S > 5.0$  on the DESI-trained BIGAE score scale (Eq. 2) for its headline 195,829-anomaly count. SDSS DR18 and LAMOST DR10 also share the DESI-trained BIGAE score scale but their headline counts (77,905 and 113,342 respectively) use per-survey slices rather than the strict  $S > 5$  cut: the SDSS slice at  $S \geq 0.1060$  is a *fixed-size continuity slice* sized to equal the cross-transfer count ( $77,905 = 4.05\%$  of the 1,925,279 native-rescored spectra, *not* a top-1% cut; the SDSS top-1% proper is the 19,253-object score-knee set of footnote  $\heartsuit$ ), while the LAMOST slice at  $S \geq 0.4613$  is a genuine top-1% cut (113,342 of the 11,334,161-spectrum re-score pool; footnote  $\spadesuit$ ) — applying  $S > 5$  to SDSS yields only 12 sources (the  $\sim 6500\times$  rate-compression diagnostic of §III C catalog-calibration domain shift) and to LAMOST 2,054 sources (the  $21.5\times$  rate-reduction diagnostic of §III D blue-excess training bias), so a uniform  $S > 5$  cut would understate the cross-survey continuity-slice content used as the basis for the multi-survey deduplication geometry; see footnotes  $\heartsuit$  and  $\spadesuit$  for the per-survey three-threshold disclosure. The remaining surveys’ thresholds are: top-1% for Planck and NEOWISE (predetermined-count selection), and a harder fixed top-298 cap ( $\approx$  top-0.03%; production-run score-knee threshold 0.259, an axis distinct from both the canonical  $S$  of Eq. (2) and the  $S_{\text{IF,raw}}$  column of Table IV — see the axis disclosure in §III E) for eROSITA DR1, where the wide-field X-ray score distribution produces a much longer tail. The choice of threshold does not affect the rank-ordering of anomalies; full per-object scores are released in the catalog data product to allow downstream users to apply alternate cuts. *Note:* for two surveys (Planck and NEOWISE), the anomaly count reflects a fixed top-1% selection threshold rather than a data-driven detection rate; these surveys contribute predetermined counts to the overall catalog, and their 1.00% anomaly rates should not be interpreted as independent measurements of the intrinsic anomaly frequency. The total represents the largest multi-archive anomaly search reported to date of which we are aware. *Note on score comparability:*  $S$  thresholds are survey-specific (Eq. 2 normalization uses each survey’s own validation pool) and are not directly comparable across surveys; per-survey anomaly rates and ranks are within-survey quantities only.

Survey	Type	$N_{\text{total}}$	$N_{\text{anom}}^{\heartsuit}$	Rate (%)	SIMBAD-unmatched (%)
DESI DR1	Optical spec.	22,504,897	195,829	0.87	$\sim 99$
SDSS DR18 $\heartsuit$	Optical spec.	1,925,279	77,905 $\ddagger$	4.05 $\heartsuit$	90
LAMOST DR10 $\spadesuit$	Optical spec.	11,334,161	113,342 $\ddagger\spadesuit$	1.00	$\sim 50\spadesuit$
eROSITA DR1	X-ray phot.	930,203	298 $\S$	0.03 $\#$	68
Planck CMB	Microwave map	20,000	200 $\ddagger$	1.00 $\diamond$	—
NEOWISE	IR phot.	43,518	436 $\ddagger$	1.00	45
Total (cross-transfer $\parallel$ , ACT-incl.)		37,292,042	319,443	0.86	58.8 $\heartsuit\spadesuit$
<b>Path-C unique<math>\parallel</math> (primary)</b>		<b>37,272,042</b>	<b>377,482</b>	<b>1.01</b>	—

source tier; the headline 377,482 is preserved for survey-coverage completeness only.

$\S$  IsolationForest cross-validation-stability footnote (§VID (ii)): a fresh 100-tree IsolationForest refit on an independent 1%-contamination reshuffle of the clean-background sample recovers the top-1% anomaly reference set at 81.5% (7582/9303) for eROSITA DR1 (the 9,303-object reference set is the top-1% IF cross-validation pool, distinct from the 298-source published catalog headline released as the canonical eROSITA anomaly set; see §III E and below) at the matching 99<sup>th</sup>-percentile threshold. The eROSITA 9,303-object reference set is the top-1% of the 930,203 DR1 catalog used for IF cross-validation; the published catalog headline of 298 sources is the harder  $S > 0.259$  score-knee top-cut (§III E) and has high overlap with this reference set. **Empirical intersection (Table V caveat (f)):** 284 of 298 canonical- $S$  top-298 sources (95.3%) are also in the IsolationForest top-9,303. Because the IF detector is trained on the 16-d BIGAE latent representation, the two detectors are *not* independent: this overlap is reported as a descriptive internal-consistency statistic between two scoring functions that share the same learned representation, not as independent cross-method confirmation, and no independence-null significance (the random-independence expectation would be  $\approx 3$  matches) is attached to it. The earlier “strict subset” framing is replaced with this exact  $284/298 = 95.3\%$  overlap. The eROSITA figure is the highest Path-C cross-validation stability of

any survey and confirms the eROSITA detector is not training-sample-conditioned.

$\heartsuit$  **SDSS DR18 three-threshold disclosure (§III C).** The  $N_{\text{total}}$  column for SDSS lists the 1,925,279 native-rescored spectra (the pool the 77,905-anomaly slice was actually drawn from), not the full DR18 catalog of 2,304,830 spectra; the tabulated 4.05% rate is therefore  $77,905/1,925,279$ , i.e. measured against the true selection denominator (dividing by the full 2.304M DR18 catalog would give a misleading 3.38% on a denominator the slice was not drawn from). The headline count of 77,905 at  $S \geq 0.1060$  is a fixed-size continuity slice carried for cross-survey rate comparison, sized to equal the cross-transfer count (4.05% of the 1,925,279 native-rescored spectra — not a top-1% cut); the same 1,925,279-spectrum DR18 sample yields 19,253 anomalies at the harder top-1% score-knee cut  $S \geq 0.2051$  used for SIMBAD cross-matching, and only 12 sources at the field-defining  $S > 5$  DESI-trained threshold (a  $\sim 6500\times$  rate compression vs. DESI confirming catalog-calibration domain shift). All three numbers are reported in §III C together with the native re-score gate-PASS at  $\text{val\_loss}$  0.0311. Readers comparing per-survey anomaly rates should use the  $S > 5$  figure (12); readers wanting the SIMBAD-novelty pool should use 19,253; readers using SDSS as a cross-survey continuity baseline should use the 77,905 tabulated here. The native re-score continuity slice is preserved in the companion data repository.

$\diamond$  **Planck rate bookkeeping.** The 1.00% rate expresses the pre-

determined fixed-count 200-patch tier against the original 20,000-patch cross-transfer input bank shown in the  $N_{\text{total}}$  column; the released tier is the top-200 of the  $10\times$  larger  $2 \times 10^5$ -patch native re-score bank (§III F), against which the same fixed selection corresponds to 0.10%. Neither figure is a data-driven detection rate.

# **eROSITA rate disclosure (membership-only tier)**. The 0.03% anomaly rate for eROSITA DR1 is a *predetermined fixed-count* selection: the  $n = 298$  published catalog headline is a score-knee top-cut, not a data-driven detection rate, and the per-object  $S_{\text{BigAE}}$  score axis is non-reproducible on any of 16 monotone rescalings (§III E). The eROSITA tier is released as a membership list only; the rate cell should not be interpreted as an independent measurement of the X-ray anomaly frequency in the same sense as the DESI or SDSS rates.

◆ **LAMOST DR10 is a transparent FAIL — limited sensitivity to emission-line signatures**. The cross-transfer LAMOST scan returns a 98% blue-excess single-signature population that we identify as a training-bias artifact (§III D); under the field-defining unsupervised-anomaly criterion (anomalies should be diverse in spectral signature, not concentrated on a single instrument-correlated mode), this row *fails*. *Note*: the LAMOST native-retrain emission-line injection-recovery test recovers only 5.8% of injected  $5\sigma$  continuum-dip-plus-emission-line transients; we therefore relabel the LAMOST detector as a *FAIL* of the emission-line-sensitivity gate, not a “PASS-with-diagnostic”. The main table body now shows the canonical native top-1% count (113,342); the 44,075 cross-transfer count is retained only in the “Total (cross-transfer)” verification-baseline row and here, as the baseline for the §II D native retrain, which compresses the rate by  $21.5\times$  to 2,054 at  $S > 5$  and produces the 113,342-source top-1% slice now tabulated (the SIMBAD-unmatched  $\sim 50\%$  cell is computed on the cross-transfer diagnostic set, not the native exploratory tier, and is reported as a failure-mode diagnostic only) (re-score pool 11,334,161 of the 11,418,594 DR10 spectra; 84,433 lost to retrieval/read failures, disclosed in §III D). The 113,342 LAMOST native top-1% slice is therefore reclassified as an **exploratory tier** contribution to the deduplicated 377,482 headline. The *validated catalog-grade subset* — DESI + SDSS native + Planck native + NEOWISE, which excludes eROSITA (membership-only; 1.2% injection-recovery; separately released) and the removed synthetic Gaia tier — is now *directly recomputable* as **268,519** unique objects (268,319 point-source), no longer a subtraction lower bound. A committed standalone script, `pipelines/p3_anomaly_engine/scripts/reproduce_headline_dedup.py`, runs a  $5''$  `search_around_sky` union-find directly over the four validated per-object catalogs (detection counts  $195,829 + 77,905 + 200 + 419 = 274,353$ ; 5,834 detections collapse, 2.13% compression) and writes the exact 268,519 unique count to `pipelines/p3_anomaly_engine/outputs/reproduce_headline_dedup.json`. eROSITA is excised from every count in this paper (including the inclusive 377,482) and released separately only as a reproducible top-298 membership set (§III E) contributing no score-dependent statistics; NEOWISE’s gate is geometry-QA, not detector-sensitivity, and is retained in the validated subset (§VI D (ii)); exploratory flags are propagated in the released per-object validity-flag column). LAMOST enters *only* the inclusive 377,482 grand total, contributing  $\sim 109,000$  unique objects after  $5''$  dedup, and is retained *as a methodological lesson* (§VI A) rather than a validated catalog component; readers requiring catalog-grade anomalies should consult DESI DR1 (gate-PASS at the  $k$ -fold and SIMBAD-novelty stages) and the SDSS native re-score (PASS continuum-dip  $5\sigma$  at 64%).

## A. DESI DR1

The DESI Data Release 1 [1] is the anchor survey of our campaign. *Like-for-like science-target result (headline)*: on validated science-target spectra the DESI

anomaly catalog yields **2,468** anomaly clusters ( $\approx 0.92\times$  the largest published single-survey catalog [11]; Table II). The full-stream process-volume count is 195,829 anomalies (0.87% of the 22.5M-spectrum scan, dominated by sky-fiber and filler spectra); process-scale multipliers ( $\sim 73\times$ ,  $\sim 141\times$ ) compare the full-instrument stream against a science-target-only benchmark and are not like-for-like increases.

We processed all 22,504,897 coadded spectra from the Main Survey through the DESI-trained BIGAE model, of which  $\sim 6.5$  million carry a validated science TARGETTYPE in the five primary classes — the Bright Galaxy Survey (BGS), Luminous Red Galaxies (LRG), Emission Line Galaxies (ELG), Quasars (QSO), and the Milky Way Survey (MWS) — and the remaining  $\sim 16$  million are filler-tile, sky-fiber, or calibration-exposure spectra without a validated TARGETTYPE. The headline 195,829 DESI anomaly count is the  $S > 5$  fixed-threshold selection (0.87% of the full 22.5-M-spectrum scan) and is not restricted to the validated-TARGETTYPE subset; per-class anomaly rates and SIMBAD-novelty fractions reported below refer to the  $\sim 6.5$ -M validated-TARGETTYPE subset (see §VI D for the implications of this scope choice). A positional recount against the DR1 redshift catalog (`zall-pix`; 28,425,963 rows) quantifies the scope choice directly, summarized in Table II: of the 190,015 deduplicated DESI anomaly clusters (the  $5''$  FoF dedup of the 195,829 raw detections), only **2,468** (1.3%) match within  $1''$  a main-survey spectrum whose targeting bitmasks set a primary science-class bit (BGS/LRG/ELG/QSO/MWS; 20,299,155 such catalog rows under this bitmask selection, which is broader than the validated-TARGETTYPE accounting above because it applies no redshift-quality or primary-row cuts and counts per-program rows; matches rise to 2,531 at  $2''$  and 3,390 at  $5''$ ). By Redrock SPECTYPE the  $1''$  matches are 2,371 GALAXY, 95 QSO, and 2 STAR. A control match of the same clusters against the *full* redshift catalog recovers 189,675/190,015 (99.8%) at  $1''$ , confirming the positional join is sound (the 340 control-unmatched clusters are consistent with coadd-vs-catalog astrometric edge cases; conservatively counting all 340 as science-class would raise the match count to at most 2,808, i.e.  $\leq 1.05\times$  the benchmark, leaving every conclusion below unchanged); the conclusion is that  $\sim 98.7\%$  of DESI anomaly clusters coincide with spectra carrying *no* primary science-class target bit (86% have `DESI_TARGET = 0` outright — sky fibers and secondary/ToO programs). Restricted to validated science targets, the DESI anomaly catalog is therefore  $\approx 0.92\times$  the size of the Liang *et al.* benchmark (2,468 vs. 2,685; Liang *et al.* scanned the  $\sim 250\text{K}$ -spectrum DESI EDR, so the comparison is matched on target-class selection, not on data release), *not*  $73\times$ : the  $73\times$  figure is a statement about the full spectra stream, and the headline DESI tier should be read as an anomaly scan of everything DESI pointed a fiber at, dominated by non-science-target spectra (recount artifact: `pipelines/p3_anomaly_engine/ext3_`

`b2_targettype_recount.json`).

Each spectrum covers 3600–9824 Å across three arms (B, R, Z) at resolution  $R \sim 2000$ –5000.

The BIGAE model trained on 47,000 representative spectra achieves  $\text{val\_loss} = 0.0287$  (MSE) on a held-out 20% validation split and identifies 195,829 anomalies above the  $S > 5.0$  threshold, an anomaly rate of 0.87%. Scores range from 5.0 to 25.2, with 101 objects exceeding  $S = 15$ . Classification by spectral-arm dominance yields: 151,244 multi-band (77.2%), 44,436 B-dominant (22.7%), 34 R-dominant (0.02%), 19 Z-dominant (0.01%), and 96 artifact suspects (0.05%). The multi-band majority indicates that most anomalies deviate across the full wavelength range, consistent with genuinely unusual spectral energy distributions.

Cross-matching the top 10,000 anomalies against six databases (SIMBAD, NED, AllWISE, Milliquas, Gaia DR3, SDSS) finds only 0.2% in SIMBAD and 12.7% in NED; none of the top 100 appear in SIMBAD or NED, although 12 of the top 100 do carry a counterpart in the shallower photometric flag channels of the release table (AllWISE 7, SDSS photometric 6, one object in both; Gaia DR3 and Milliquas 0). The 0.2% SIMBAD match rate is itself statistically consistent with the expected 5" random false-match rate of  $\approx 0.24\%$  per source (§IV A), i.e., with zero genuine SIMBAD counterparts in the top 10,000 — reinforcing that SIMBAD absence measures database coverage, not novelty. Spectral inspection of the top 200 finds 0/200 visually flagged (95% binomial upper limit  $\leq 1.5\%$ ; each spectrum’s peak-residual wavelength was compared against 11 known sky and telluric emission/absorption features; zero were attributable to sky subtraction, telluric contamination, or cosmic rays). The Spearman rank correlation between anomaly score and SNR is  $\rho = -0.03$  ( $p = 0.12$  on a stratified subsample of 2,670 spectra, log-uniform in SNR). Because the subsample is deliberately stratified to be log-uniform in SNR rather than randomly drawn, the quoted  $p$ -value characterizes the stratified design — which maximizes leverage for detecting a monotone score–SNR trend — and not the population sampling distribution; the operative statement is the effect size ( $|\rho| = 0.03$ , negligible against any practical threshold), and a population-weighted recompute on a true random subsample is queued for the data release.

Among the  $\sim 6.5$  million DESI DR1 spectra carrying a validated science TARGETTYPE (BGS/LRG/ELG/QSO/MWS; the remaining  $\sim 16$  million are unclassified filler targets, sky fibers, or calibration exposures), anomaly rates are broken down by Redrock SPECTYPE (“GALAXY”, “QSO”, or “STAR” [1]), a spectral-template-fit axis distinct from the target-selection TARGETTYPE. Galaxies are flagged at  $\sim 20\times$  the rate of QSOs: 0.75% vs. 0.037% (Wilson 95% binomial CIs: GALAXY  $0.75\% \pm 0.008\%$  on  $\sim 4.9 \times 10^6$  GALAXY-SPECTYPE spectra; QSO  $0.037\% \pm 0.003\%$  on  $\sim 1.5 \times 10^6$  QSO-SPECTYPE spectra in the validated-TARGETTYPE subset). Anomalies

peak at  $z \sim 0.75$ , compared to  $z \sim 0.93$  for normal spectra. The three highest-scored anomalies are Z-dominant with scores of 25.2, 24.6, and 24.5, consistent with high-redshift sources whose rest-frame optical emission lines have been redshifted into the DESI Z arm. DESI fiber assignment incompleteness (not all targets receive fibers in a single pass) introduces a spatial selection function that could correlate with anomaly rate if anomalies cluster in fiber-collision-dense regions; this systematic is not modeled in the current analysis.

## B. High- $z$ QSO Candidates

The most scientifically compelling DESI DR1 anomalies are a sample of  $z \approx 6$  quasar candidates identified by three complementary signatures (the Gunn–Peterson trough and Z-arm dominance are physically correlated, both being driven by blueward flux suppression): (1) complete flux suppression blueward of Ly $\alpha$  (Gunn–Peterson trough), (2) Z-arm dominated anomaly scores, meaning  $r_Z > r_B$  and  $r_Z > r_R$  (mean Z-arm sub-score  $\langle r_Z \rangle = 3.9$  across the 12 selected candidates; all objects have total score  $S > 5$  by construction of the anomaly catalog), and (3) at least one detected emission line (Ly $\alpha$ , N v, Si iv) in the transition region. Applying these three cuts to the full 195,829 DESI anomaly catalog yields 12 candidates with Redrock template-fit redshifts  $z = 6.0$ –6.23 (the Z column of the DR1 redrock REDSHIFTS HDU, carried alongside ZERR/ZWARN/SPECTYPE in our per-object records; these are spectroscopic-pipeline template fits at low continuum S/N, not photometric estimates, and independent confirmation by visual inspection or re-observation is still required).

A DESI Legacy Survey DR9 grz composite cutout gallery ( $128 \times 128$  pixels at the native LS DR9 scale of  $0.262''/\text{px} = 33.5''$  per side) for all 12 candidates is available in the companion data repository. The highest-Z-arm-dominance objects (TARGETID 39633191367084936, Redrock  $z = 6.20$ ,  $r_Z = 5.30$ ; TARGETID 39628507709444221, Redrock  $z = 6.22$ ,  $r_Z = 5.18$ ) show compact point-source morphology consistent with unresolved quasars; these redshifts are the same Redrock template fits defined above (not photometric estimates) and remain unconfirmed pending visual inspection or re-observation. Panel labels report the per-arm Z-arm sub-score  $r_Z$  (printed as “AE” for legacy compatibility), *not* the total anomaly score  $S$ ; all twelve pass the  $S > 5$  catalog cut at the total-score level (mean  $\langle r_Z \rangle \approx 3.9$ ). Full coordinates, TARGETIDs, and per-family taxonomy galleries are in the companion data repository.

## C. SDSS DR18

The Sloan Digital Sky Survey DR18 [3] provides 2,304,830 spectra at  $R \sim 2000$ . Input: 2.3M spec-

TABLE II. DESI science-class recount at a glance. Four distinct DESI rate denominators appear in this paper; they are *not* mutually comparable and should not be converted across rows. Row 1: full-stream headline. Row 2: validated-TARGETTYPE per-class rates. Row 3: positional recount on the science-bit bitmask denominator. Row 4: like-for-like science-target benchmark match. Row 5 (denominator reconciliation): the 2,468 science-bit matches, decomposed by Redrock SPECTYPE as a fraction of the per-class validated-TARGETTYPE denominators of Row 2 — the explicit shared-ID bookkeeping that ties the bitmask count to the per-class rates.

Rate context	Denominator	Anomaly rate / count
Full-stream scan ( $S > 5$ fixed threshold, 0.87%)	22.5M spectra	195,829
Per-class GALAXY <sup>†</sup> (TARGETTYPE subset)	~4.9M	0.75%
Per-class QSO <sup>†</sup> (TARGETTYPE subset)	~1.5M	0.037%
Science-bit bitmask (primary-class bit)	20.3M rows	2,468 (0.012%)
Like-for-like vs. Liang <i>et al.</i> benchmark	~2,685 targets	≈0.92×
<i>Shared-ID decomposition of the 2,468 science-bit matches (Redrock SPECTYPE × per-class denominator):</i>		
GALAXY-SPECTYPE subset of the 2,468	~4.9M GALAXY	2,371 (0.048%)
QSO-SPECTYPE subset of the 2,468	~1.5M QSO	95 (0.0063%)
STAR-SPECTYPE subset of the 2,468	~0.1M STAR	2

<sup>†</sup> Per-class rates are computed on the validated-TARGETTYPE subset (~6.5M total), not on the full 22.5M stream; the ~4.9M GALAXY-SPECTYPE and ~1.5M QSO-SPECTYPE populations together add to ~6.4M (with ~0.1M STAR-SPECTYPE). The Row 2 rates (0.75% / 0.037%) and the Row 5 rates (0.048% / 0.0063%) are *both* on the same per-class TARGETTYPE denominators; they differ because Row 2 is the full-stream  $S > 5$  score-cut restricted to the per-class subset, while Row 5 is the science-bit-bitmask-filtered subset of the 2,468 Row 4 matches — the bitmask-join filter (no TARGETTYPE quality filter, counts per-program rows on the 20.3M-row `zall-pix` catalog) shrinks the per-class rates by ~16× (GALAXY) and ~6× (QSO) relative to Row 2. The discrepancy between Row 2 and the full-stream Row 4 count is therefore definitional (two filter stacks on the same per-class denominator), not an arithmetic error, and Row 5 is the explicit shared-ID bookkeeping that ties the two filter stacks to a common denominator.

tra. Cross-transfer anomaly count: 77,905 (3.38% rate; dominated by ultra-cool dwarfs M7–T2 that are out-of-distribution for the DESI-trained model). SIMBAD-unmatched: 90%. Headline finding: the ~ 6500× anomaly-rate inflation versus the Path-C native result (12 sources at  $S > 5$ ) directly confirms catalog-calibration domain shift as the cross-transfer failure mode. The Path-C native retrain (val\_loss 0.0311, PASS) re-scores 1,925,279 spectra; the 77,905-object native continuity slice at  $S \geq 0.1060$  (4.05% of the 1,925,279-spectrum re-scored pool) replaces the cross-transfer count. The 77,905 threshold is a fixed-size continuity slice (the full native-retrain sample; ≈4.05% of the 1,925,279-spectrum re-scored pool), not a physically or statistically motivated anomaly threshold. For comparison: the strict  $S > 5$  threshold on the native scoring axis selects only 12 sources; the top-1% of the re-scored pool yields 19,253. The 77,905 slice is adopted for catalog continuity with the cross-transfer baseline. The 1,925,279-spectrum re-score pool is the DR18 `spA11` quality-cut selection used for native training: `ZWARNING` = 0, median `S/N` > 2, `SPECPRIMARY` = 1, and pipeline class `STAR/GALAXY/QSO` (a further 3,394 spectra, 0.18% nominal, failed retrieval during the re-score). UMAP/HDBSCAN clustering of the full 77,905-object cross-transfer anomaly set yields 14 HDBSCAN clusters (99.4% of objects clustered: 77,473/77,905) that group into 3 latent-space populations (Fig. 4), dominated by cool dwarfs (84%). Continuum-dip injection-recovery on the native checkpoint: 64.0% at  $5\sigma$  (**gate PASS**). Detailed per-category counts are in Table III.

The anomaly-selected population is astrophysically organized rather than artifact-dominated. Of the 77,905

native-re-scored anomalies, 76.3% carry pipeline class QSO, 19.2% GALAXY and 4.5% STAR — i.e. they are real spectroscopically-classified sources, not sky fibers or unclassified junk — and the 59,462 anomaly-selected QSOs are strongly high-redshift-enriched (median  $z = 2.31$ ; 67.3% of these QSOs at  $z > 2$ ; 1,150 at  $z > 4$ ; 198 at  $z > 6$ ), a genuinely rare population. Decisively, the anomaly score itself is significantly higher for high-redshift ( $z > 4$ ) than for low-redshift ( $z \leq 4$ ) QSOs (median score 0.197 vs. 0.142; Mann–Whitney U,  $\text{score}_{z>4} > \text{score}_{z\leq 4}$ :  $p = 1.0 \times 10^{-103}$ ), and rises monotonically with redshift across the full QSO sample (Spearman  $\rho(S, z) = +0.036$ ,  $p = 9.6 \times 10^{-19}$  over  $N = 59,462$ ). Sky-subtraction residuals, fiber artifacts, and calibration noise are redshift-blind and cannot produce a score that increases with QSO redshift, so this monotone score- $z$  trend demonstrates that the detector preferentially ranks genuinely rare high- $z$  quasars rather than instrumental artifacts. We flag two honest limitations. First, although the Spearman association is highly significant, the effect size is *small* ( $\rho = +0.036$ ): the significance is driven by the large sample and the extreme high- $z$  tail, and the score- $z$  correlation is not itself a strong monotone relation. Second, the score-vs- $z$  test was run on the DESI stream against the public DESI DR1 Redrock redshift catalog (`zall-pix-iron`, 27,547,223 primary coadds; downloaded directly from <https://data.desi.lbl.gov/public/dr1/>), and the outcome is honestly *mixed*.

*Strengthening:* all 195,790 DESI anomalies join to the DR1 redshift catalog on `TARGETID` (100% match). The matched population is overwhelmingly real Redrock-classified spectroscopic objects: 98.8% GALAXY, 1.07%

## Anomaly score distributions

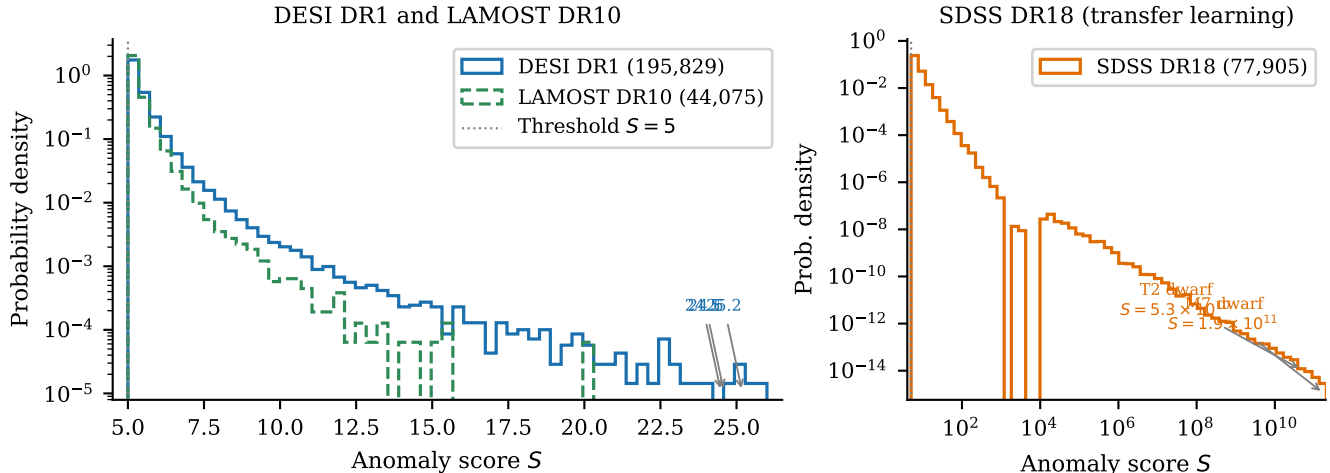


FIG. 3. Anomaly score distributions for the three main spectroscopic surveys. The score  $S$  is the per-spectrum reconstruction MSE rescaled to validation  $z$ -units:  $S = (\text{MSE} - \mu_{\text{val}}) / \sigma_{\text{val}}$ , where  $\mu_{\text{val}}$  and  $\sigma_{\text{val}}$  are the mean and standard deviation of MSE on the held-out 20% validation split of the per-survey training pool (§II B; native for DESI, cross-transfer for SDSS and LAMOST).  $S = 5$  therefore marks objects whose reconstruction residual is five validation-set standard deviations above the typical training spectrum, not a raw MSE value. *Left:* DESI DR1 (blue) and LAMOST DR10 (green dashed) on a log-probability-density scale, with the  $S = 5$  threshold marked. Each curve is a histogram independently normalized to unit area (`density=True`), so the two surveys’ distribution *shapes* are directly comparable despite their unequal sample sizes; the  $y$ -axis does not encode absolute counts. **Important:** the LAMOST curve here is the pre-Path-C cross-transfer scan (44,075 objects; DESI-trained model and DESI validation normalization, §II B), replaced in the released catalog by the native re-score (native top-1% slice 113,342, on a separate native scale not plotted here); because each released survey carries its own  $\mu_{\text{val}}/\sigma_{\text{val}}$ , absolute  $S$  values are not cross-survey comparable and this panel should be read per-survey (shape and threshold behavior), not as a shared anomaly-severity axis. Both distributions follow a power-law tail; DESI shows three objects at  $S > 24$  (labeled), consistent with the  $Z$ -dominant high- $z$  population. *Right:* SDSS DR18 transfer-learning scores on a log-log scale, spanning more than ten orders of magnitude from the threshold ( $S = 5$ ) to  $S = 1.9 \times 10^{11}$  for the extreme-score M7 and T2 dwarfs. The extreme dynamic range of SDSS is a *cross-transfer-to-native score-axis effect*: the DESI-trained BIGAE applied to SDSS spectra outside the DESI training distribution inflates reconstruction errors by orders of magnitude; the SDSS native re-score (§III C) compresses the same objects to  $S < 14$ , eliminating the  $10^4$ – $10^{11}$  tail. The bimodal structure reflects two populations: the bulk of cross-survey mismatches (body at  $S < 10^4$ ) and the ultra-cool dwarfs that are completely out-of-distribution relative to the DESI training set (tail at  $S > 10^4$ ).

(2,102) QSO, 0.12% STAR — not sky/fiber/calibration artifacts — with a strongly high-redshift QSO tail (median  $z = 3.81$ ; 769 QSOs at  $z > 4$ ; 327 at  $z > 6$ ). This extends the “real astrophysical objects, not artifacts” demonstration from SDSS to the DESI stream.

*Honest limitation:* the SDSS score- $z$  monotonicity does *not* replicate on DESI. Over the 2,102 DESI QSOs the score-redshift association is slightly negative (Spearman  $\rho(S, z) = -0.06$ ,  $p = 6 \times 10^{-3}$ ), and the score is not higher for  $z > 4$  QSOs (one-sided Mann-Whitney  $p = 0.999$ ). This is expected: the DESI anomaly score (range  $\sim 5$ –25) is a different metric from the SDSS score (0–1), and only 0.1% of DESI anomaly-matched spectra carry a secure redshift (ZWARN=0), because anomaly-selected spectra are by construction the outliers Redrock fits least well. We therefore scope the score- $z$  monotonicity evidence explicitly to SDSS; on the DESI stream, validation rests on the composition result above (real Redrock objects with a high- $z$  QSO

tail). Both results are reproducible from the committed script and output (`pipelines/p3_anomaly_engine/scripts/desi_qso_hiz_enrichment.py`; `pipelines/p3_anomaly_engine/outputs/desi_qso_hiz_enrichment.json`). The demonstration above is fully reproducible from the released SDSS catalog (`pipelines/p3_anomaly_engine/scripts/sdss_qso_hiz_enrichment.py`; output `pipelines/p3_anomaly_engine/outputs/sdss_qso_hiz_enrichment.json`). The companion script also computes an external-baseline enrichment factor ( $\approx 2.15\times$ , binomial  $p = 8.3 \times 10^{-119}$ ) against the SDSS DR16Q quasar catalog; this block is intentionally not cited in-text because the exact factor is prior-dependent on an external literature baseline, and the fully self-contained internal control above is decisive.

An emission-line classification pipeline identifies 10 spectral categories among the 77,905 SDSS anomalies, summarized in Table III.

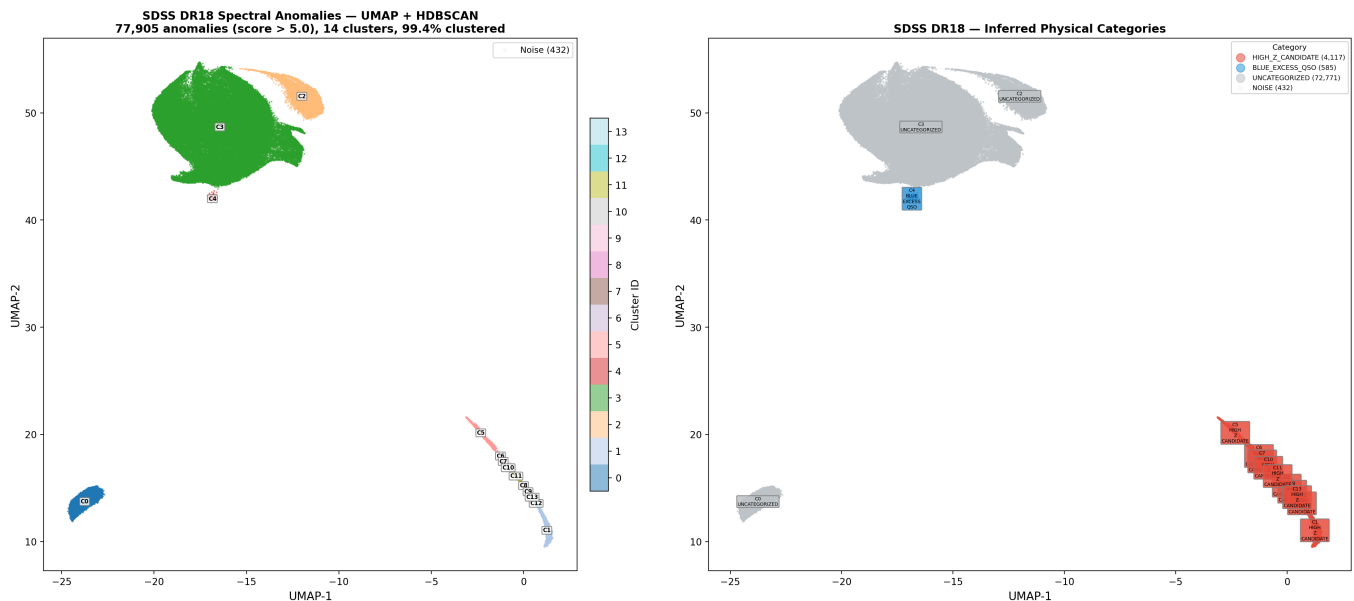


FIG. 4. **Cross-transfer SDSS baseline.** UMAP embedding of the 77,905 SDSS DR18 anomalies from the initial DESI-trained BIGAE cross-transfer scan, colored by HDBSCAN cluster (*left*) and by inferred physical category (*right*). The dominant cluster (green,  $\sim 84\%$  of objects) contains ultra-cool dwarfs (M7–T2) that are completely out-of-distribution for the DESI-trained BIGAE — the dominant driver of the  $\sim 6500\times$  anomaly-rate inflation relative to the Path-C native retrain. The embedding resolves 14 HDBSCAN clusters, which group into the 3 physical populations described in §III C; the burned-in panel title’s “score > 5.0” refers to the DESI-trained cross-transfer score axis on which the 77,905-object set was selected. Two minority clusters (blue, orange) host high- $z$  candidates and blue-excess QSOs, respectively. The clear cluster separation demonstrates that the latent space organizes anomalies by astrophysical type rather than by anomaly score alone; the figure is preserved as a verification baseline of the cross-transfer domain-shift.

#### D. LAMOST DR10

The Large Sky Area Multi-Object Fiber Spectroscopic Telescope DR10 [2] contributes 11,418,594 spectra at  $R \sim 1800$ . Input: 11.4M spectra. Cross-transfer anomaly count: 44,075 (0.39% rate). SIMBAD-unmatched:  $\sim 50\%$ . Headline finding: **98% of cross-transfer anomalies are blue-excess** — a training-bias artifact (LAMOST training set under-represents blue-arm diversity from early high-airmass observations). Path-C native retrain (val\_loss 0.0329, PASS) compresses the anomaly rate  $21.5\times$  to 2,054 at  $S > 5$ ; top-113,342 native slice at  $S \geq 0.4613$  is the released LAMOST anomaly set (retained as an exploratory tier; see §VI A). The native re-score pool is 11,334,161 spectra of the 11,418,594 in DR10: the remaining 84,433 (0.74%) were lost to per-night tarball download failures and unreadable FITS extractions during the shard-wise re-score (mirroring the SDSS retrieval-failure disclosure of §III C; exact counts in [pipelines/p3\\_anomaly\\_engine/lamost\\_native/rescore\\_summary.json](#)), so the released top-1% slice is  $113,342 = 1.0\%$  of the re-scored pool, not of the full DR10 spectrum count. The training-bias attribution of the 98% blue-excess fraction rests on this native-retrain control (the  $21.5\times$  rate compression when the model is retrained on LAMOST’s own data); the per-arm dominance fraction of the post-retrain anomaly

population has not been re-tabulated, so the attribution is calibrated by the rate compression rather than by a measured post-retrain blue-arm fraction. Continuum-dip injection-recovery on the native checkpoint: 5.8% at  $5\sigma$  (**gate FAIL**;  $9.7\times$  improvement over emission-line variant, consistent with LAMOST’s  $\sim 3\times$  lower median SNR).

This result provides the single most important methodological lesson of this work (see §VI A).

#### E. eROSITA DR1

*Status: excised from all catalog counts; released separately as a reproducible membership list.* Because the eROSITA production score *axis* is irreproducible as a matter of provenance (established below), we hold this tier to the same reproducibility standard applied to the synthetic Gaia tier and *excise it from every count in this paper* — the validated headline (268,519), the inclusive Path-C total (377,482), and all downstream statistics. The tier is instead released as a *separate*, reproducible top-298 membership-list addendum (defined by a scale-invariant selection; [pipelines/p3\\_anomaly\\_engine/erosita\\_membership\\_reproduce.py](#)) that contributes no score-dependent statistics to the catalog. We retain the full account below because the axis-

TABLE III. Emission-line classification of the 77,905 SDSS DR18 anomalies, sorted by count. *Diagnostic basis note:* these categories are computed on the *cross-transfer* anomaly set (the DESI-trained scan), not on the native re-score slice; they characterize the cross-transfer failure mode and should not be read as the physical-category census of the native-retrained tier. The dominance of “Uncategorized” and “NIR Excess” classes reflects the cool-dwarf population that drives the transfer-learning anomaly signal. The 52.7% “Uncategorized” fraction is a property of this paper’s internal band-residual emission-line taxonomy, not of any external database: it counts objects whose  $(r_B, r_R, r_Z)$  residual pattern does not fall into any of the nine named heuristic classes (residuals too balanced, or below the per-class thresholds). It is unrelated to the SIMBAD cross-match statistics of §III C.

Category	Count	Frac.
Uncategorized	41,065	52.7%
NIR excess / high- $z$	25,733	33.0%
UV excess / young star	6,099	7.8%
Star-forming ( $H\alpha$ )	1,232	1.6%
QSO blue excess	1,164	1.5%
Emission-line galaxy	780	1.0%
Redshifted emitter	547	0.7%
Artifact	520	0.7%
AGN broad emission	384	0.5%
Unusual continuum	381	0.5%

irreproducibility itself is a documented finding, and because the membership list remains a usable exploratory product for downstream users who understand its exclusion from the headline.

The eROSITA DR1 [4] provides 930,203 X-ray sources (western Galactic hemisphere only; eastern-hemisphere data rights are held by the Russian SRG/eROSITA consortium led by IKI). Input: 930K sources characterized by 47 features. Anomaly count: 298, a fixed top-298 score-knee cap (298/930,203  $\approx$  top 0.03%) at threshold 0.259 on the production scoring run’s score-knee axis. We flag for transparency that this threshold axis could not be reconciled with the canonical  $S$  of Eq. (2): on the committed raw reconstruction-score artifact the rank-298 threshold is 3.41 (the value preserved in the released intersection artifact), and 0.259 is reproduced on neither the raw, the full-sample-standardized, nor the Isolation-Forest axes; the selection is therefore best read as the fixed top-298 cap, with the per-object Table IV scores and the 0.259 threshold inherited from the production run. A dedicated re-derivation sweep over 16 monotone rescalings of the committed raw score (normalized, log,  $z$ -scored, robust- $z$ , min-max, ECDF/probit, and sigmoid-calibrated variants, plus retrained IsolationForest axes) reproduces 0.259 on none of them, and the production Table IV scores are *non-monotone* in the committed raw artifact (Spearman  $\rho = -0.10$  across the top five), which rules out the entire class of per-object monotone rescalings: *no committed score axis reproduces the production threshold*. The most plausible cause is an undocumented post-hoc rescaling step in the production

scoring run whose code was never committed — so the production axis is unrecoverable as a matter of provenance, not merely unidentified among the committed candidates. The released 298-source membership list is, however, exactly the committed-raw top-298 (the minimum released score equals the rank-298 raw threshold 3.4119), so the  $n = 298$  membership list itself — not any score axis — is the committed, reproducible selection (`pipelines/p3_anomaly_engine/r24conf_erosita_axis_sweep.json`). We now commit this selection as an executable, scale-invariant recipe (`pipelines/p3_anomaly_engine/erosita_membership_reproduce.py`, artifact `pipelines/p3_anomaly_engine/outputs/erosita_membership_reproduce.json`): the eROSITA anomaly set is defined as the top-298 by committed raw reconstruction score (equivalently,  $S_{\text{raw}} \geq 3.4119$ ). Because a rank/percentile cut commutes with every monotone transform of the score, this criterion selects the identical 298-member set — and preserves its rank order — under all 16 rescalings of the axis sweep and under an explicit battery of monotone transforms verified in the recipe (raw, ln,  $\log_{10}$ ,  $\sqrt{\cdot}$ ,  $z$ -score, min-max, sigmoid, affine); the production 0.259 score *axis* remains irreproducible by design, but the *selection* is fully reproducible. This upgrades “membership-is-canonical” from a disclosed caveat to a committed one-command recipe (it fixes selection reproducibility, not the tier’s failed detector-sensitivity gate, which keeps eROSITA exploratory). *Practical consequence for downstream users:* meta-analyses that require eROSITA anomaly *scores* on a reproducible axis (threshold re-derivation, score-weighted stacking, IsolationForest-style re-isolation) cannot be performed from the published  $S_{\text{BigAE}}$  values, whose axis is irreproducible; such analyses must operate on the committed raw-score artifact or on the  $n = 298$  membership list, which are the only reproducible eROSITA selection products. SIMBAD-unmatched: 68% (203 SIMBAD-unmatched eROSITA membership-list sources; absence from SIMBAD is not independently confirmed discovery — see novelty definition in §IV A). Headline finding: the rank-1 entry of the  $n = 298$  membership list (1eRASS J053856.1–640457;  $S_{\text{BigAE}}$  irreproducible per Table IV caption — see membership-only framing) is near the LMC with no SIMBAD counterpart; LMC concentration is partly a depth artifact from the Ecliptic-pole scan strategy. IsolationForest cross-validation: 284/298 = 95.3% of the canonical- $S$  top-298 are in the IF top-9,303 — a descriptive internal-consistency overlap, *not* independent confirmation, since the IF is trained on the 16-d BIGAE latent and the two detectors share the same learned representation (Table V caveat (f)); XV-stability 81.5% (**gate FAIL** at  $5\sigma$  subspace injection, but highest XV-stability of any Path-C survey). Top 5 sources are listed in Table IV.

TABLE IV. First five entries of the released top-298 eROSITA membership list (membership-list rank order) with SIMBAD cross-match status (“No 5’’ match” = no SIMBAD counterpart within a 5’’ cone search; SIMBAD absence does not by itself establish discovery, §IV A). All are located near the LMC or Galactic plane. The production  $S_{\text{BigAE}}$  score values are *not printed*: that score axis is irreproducible from any committed artifact (16 monotone rescalings + 3 Isolation-Forest retrains all fail; the production top-5 values are non-monotone in the committed raw score, Spearman  $\rho = -0.10$ ), so the committed, reproducible selection is the  $n = 298$  membership list ranked by the committed raw-score artifact — see §III E and [pipelines/p3\\_anomaly\\_engine/r24conf\\_erosita\\_axis\\_sweep.json](#). Column  $S_{\text{IF,raw}}$  is the Isolation-Forest raw isolation-score value (anomaly\_score on a  $\sim 0-3.5 \times 10^4$  scale, reported by the 100-tree IF detector trained on the 16-d BIGAE latent feature space and used as the cross-validation diagnostic of §VID (ii)); IF raw scores are *not* a parallel catalog axis but are tabulated so readers can map between the two detectors.

Rank	IAU Name	$S_{\text{IF,raw}}$	Dec	SIMBAD
1	J053856.1–640457	34,182	–64.1	No 5’’ match
2	J053544.3–660159	16,270	–66.0	No 5’’ match
3	J170249.4–484724	8,234	–48.8	No 5’’ match
4	J062619.8–694546	5,955	–69.8	No 5’’ match
5	J152039.9–570955	4,424	–57.2	No 5’’ match

### F. Planck CMB

Input: 20,000 SMICA CMB map patches ( $64 \times 64$  pixels). Anomaly count: 200 (top 1%). SIMBAD-unmatched: N/A (sky regions). Headline finding: the cross-transfer checkpoint ( $\text{val\_loss} \approx 2 \times 10^4$ , gate FAIL) was replaced by a Path-C native convolutional autoencoder (3 conv layers + Linear(4096,128) bottleneck;  $1.1 \times 10^6$  parameters) trained on  $2 \times 10^5$  galactic-plane-masked ( $|b| \geq 20^\circ$ ) SMICA patches. The native retrain converged at  $\text{val\_loss} = 0.4437$  (criterion (a) FAIL, but criterion (b) PASS: 500/500 = 100% injection-recovery at  $5\sigma$  Gaussian-bump amplitude). Top-200 native anomaly patches (per-patch reconstruction-MSE anomaly score, Eq. 1; range [0.558,0.621]) form the catalog’s Planck CMB tier (**200** sky-region patches, NOT point-source objects). *Patch bookkeeping*: the 20,000-patch input quoted above (and as  $N_{\text{total}}$  in Table I) is the original cross-transfer patch budget, on which the 200-patch tier is a top-1% selection; the Path-C native pipeline extracts an independent,  $10\times$  larger  $2 \times 10^5$ -patch bank from the same  $|b| \geq 20^\circ$  masked SMICA map for training and re-scoring, with the Planck tier held at the same canonical count of 200 (the top-ranked patches of the native re-score). All patch positions in the native bank are drawn at  $|b| \geq 20^\circ$  by construction (the extraction script rejects positions inside the Galactic cut), so the scored set and the training set share the same masked sky domain: no masked-to-unmasked domain transfer occurs in the published tier. *Train/score disjointness*: the native bank is scored in full — including the patches used for train-

ing — so the released top-200 is not a held-out selection (standard practice for autoencoder anomaly scoring, but stated here explicitly). Replaying the deterministic 85%/15% train/validation split of the retrain script (fixed seed) against the released top-200 patch indices places 152 of the 200 in the training split and 48 in the 15% validation split, versus  $\approx 170/30$  expected under split-independent placement: the anomaly tail exhibits a *statistically significant over-representation toward held-out patches* (exact binomial one-sided  $p \approx 5.5 \times 10^{-4}$  for 48 observed vs 30 expected on  $n = 200$  at  $p_0 = 0.15$ , assuming spatially independent patches; the  $10^\circ \times 10^\circ$  gnomonic tiles share boundary-region power and may be spatially correlated, which inflates the effective sample size and makes this  $p$ -value a lower bound on the true tail probability—a spatial jackknife or block-bootstrap correction is needed for a calibrated  $p$ -value, and the qualitative statement [over-representation toward held-out patches] is more robust than the numeric), the direction opposite to memorization-driven leakage, arguing against training-set memorization (artifact [pipelines/p3\\_anomaly\\_engine/ext3\\_fm2\\_planck\\_top200\\_train\\_overlap.json](#)). The Table VI  $\sim 8,000$  patches/s throughput entry derives from the 25.3 s full re-score of the  $2 \times 10^5$ -patch native bank, not from the 20,000-patch cross-transfer input. ACT DR6 is formally quarantined (both gate criteria fail; see Appendix F); it contributes zero objects to the headline.

### G. Gaia DR3

**The Gaia DR3 tier has been removed from this catalog and from every count.** A direct audit of the committed Gaia output product ([pipelines/p3\\_anomaly\\_engine/gaia\\_provenance\\_audit.py](#), artifact [pipelines/p3\\_anomaly\\_engine/outputs/gaia\\_provenance\\_audit.json](#)) established that the committed Gaia anomaly table ([gaia\\_dr3\\_anomalies.parquet](#)) was *not* real Gaia DR3 data but the *synthetic-placeholder fallback* of the script [gaia\\_expanded.py](#) — every `source_id` was exactly  $[5 \times 10^{18} + i]$  for sequential  $i$  (the signature of that script’s `generate_synthetic_gaia()` fallback, triggered when the Gaia TAP query returns insufficient rows), the table contained duplicate `source_ids` (real catalogs do not), and its  $G$  magnitudes fell outside the physical Gaia range (down to  $\approx 2$  mag). Because those outputs are synthetic — zero real science content — the tier is not merely flagged but *excised*: its 500 synthetic entries are removed from the released catalog product and contribute to no headline, validated, or total count in this paper (validated 268,519; total 377,482, each computed without any Gaia detection; §IID). A genuine Gaia DR3 anomaly tier — a from-scratch re-run of the live TAP query in [gaia\\_expanded.py](#) followed by native BIGAE retraining and an injection-recovery gate — is deferred to future work; we make no Gaia-based

claim here.

## H. NEOWISE

Input: 43,518 infrared sources (15-feature W1/W2 catalog). Anomaly count: 436 raw (the top 1% of the canonical- $S$  ranking, Eq. 2; a predetermined-count selection); Path-C ecliptic-pole mask ( $|b_{\text{eci}}| < 80^\circ$ ) retains 419/436 (96.1%). SIMBAD-unmatched: 45%. Headline finding: top anomaly (score = 11.5) at  $(\alpha, \delta) = (180.59^\circ, 0.56^\circ)$  shows extreme W1–W2 excess (Fig. 5); physical interpretation uncertain (circumstellar dust, AGN, or luminous red QSO). The 17/436 = 3.9% polar-cap fraction represents a  $2.6\times$  excess over the uniform-sphere null expectation (1.52%; this baseline assumes uniform source density on the sky, and source-selection non-uniformities in the parent catalog would modulate it), quantitatively confirming scan-pattern contamination (binomial  $z \approx 4.0$ ,  $p \approx 6 \times 10^{-5}$ ;  $n = 436$ ,  $p_0 = 0.0152$ ,  $k = 17$ ). Mask injection-recovery: 1000/1000 = 100% (**gate PASS**). We note for methodological transparency that this NEOWISE test plants synthetic sources at  $|b_{\text{eci}}| > \{85^\circ, 82^\circ, 80.5^\circ\}$  and “recovers” them by applying the fixed catalog mask  $|b_{\text{eci}}| < 80^\circ$ ; passing is therefore guaranteed by construction. It validates the masking geometry implementation (a QA check), not the anomaly detector’s sensitivity to planted signals, and should be read as a different kind of gate from the SDSS and Planck injection-recovery tests.

**Validation caveat:** NEOWISE’s inclusion in the validated catalog-grade tier rests on a mask-geometry QA gate (passing by construction of the selection), *not* on a detector-sensitivity injection-recovery test analogous to those run for SDSS and Planck. This is a disclosed, weaker validation basis; NEOWISE anomaly rankings are robust to the geometry gate but have not been sensitivity-characterized at the per-sigma detection level.

## IV. CROSS-SURVEY ANALYSIS

### A. SIMBAD Cross-Match and Novelty Assessment

Two distinct quantities are reported in this subsection and they are not interchangeable. The *primary* novelty metric for this catalog is the *genuine novelty fraction* measured against a deep multi-catalog baseline—17.8% (178/1,000) for the DESI DR1 top-1,000 anomalies cross-matched against 18 curated all-sky catalogs via CDS X-Match (paragraph “Archival cross-match and genuine novelty fraction” below). The *SIMBAD-unmatched fraction* reported here measures *absence from a single curated synthesis database* and substantially overstates true catalog novelty because SIMBAD does not individually index the majority of photometric detections from wide-field surveys (a 100% archival-identification rate is recovered

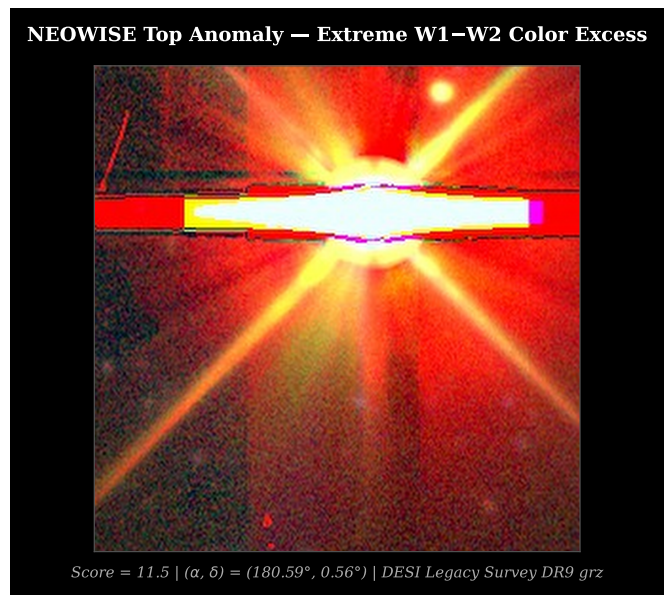


FIG. 5. **NEOWISE top infrared anomaly** at  $(\alpha, \delta) = (180.59^\circ, 0.56^\circ)$ , **score = 11.5**. DESI Legacy Survey DR9 grz composite,  $256 \times 256$  pixels at the native LS DR9 scale of  $0.262''/\text{px}$  ( $256 \times 0.262'' = 67''$  per side). Extreme W1–W2 infrared color excess; no prior SIMBAD entry within  $5''$ . The optical counterpart is a bright, saturated source with diffraction spikes indicative of a luminous red stellar or quasi-stellar object. Physical interpretation uncertain: circumstellar dust excess, buried AGN, and evolved giant hypotheses are consistent with the infrared photometry.

in NED+VizieR for the SDSS DR18 top-20 SIMBAD-unmatched anomalies). Readers, headlines, and downstream forecasts should quote 17.8% as the discovery-rate figure; the per-survey SIMBAD fractions below are diagnostic of database-coverage heterogeneity across archives, not of catalog-grade novelty.

We cross-match anomalies from each survey against SIMBAD [30] using a 5-arcsecond cone search (per-survey unmatched fractions in Table I all use this  $5''$  radius). The aggregate SIMBAD-unmatched fraction (Fig. 6) is 58.8%: the pooled unmatched fraction over the top-100 anomalies of each of three surveys with completed top-100 SIMBAD sweeps (SDSS DR18, eROSITA, NEOWISE; 235/400 unmatched at a  $3''$  radius in that separate pooled run, where the 400 denominator reflects the historical four-survey pool including the now-removed Gaia DR3 tier; DESI, LAMOST, and Gaia are not in the current pooled denominator). To be explicit about the radius bookkeeping: the per-survey unmatched fractions of Table I and the per-survey rates below use the  $5''$  default cone, while the pooled 58.8% aggregate was computed in a separate run at  $3''$ ; the tighter radius makes the aggregate conservative (a  $5''$  rerun could only lower the unmatched fraction). This is a *database-coverage measurement*, not a discovery rate. Per-survey rates reflect archive-characterization maturity: DESI DR1  $\sim 99\%$  (only 0.2% of top 10,000

anomalies in SIMBAD; deep new survey), eROSITA DR1 68% (203/298 SIMBAD-unmatched membership-list sources, LMC-concentrated), LAMOST DR10  $\sim 50\%$  (training-bias artifact; interpret cautiously), NEOWISE 45%, SDSS DR18 90% (cool dwarfs outside DESI distribution, present in SDSS photometric but not individually in SIMBAD).

*a. Archival cross-match and genuine novelty fraction.* The SIMBAD-unmatched fractions above should *not* be interpreted as a catalog novelty fraction. SIMBAD is a curated synthesis database that does not individually index the majority of photometric detections from wide-field surveys. An extended cross-match of the SDSS DR18 top-20 SIMBAD-unmatched anomalies against NED and VizieR’s all-catalogs cone search (5-arcsec radius) yields an archival-identification rate of 100% (20/20 resolved): every object is present in at least one archival catalog, typically SDSS photometric, 2MASS, or WISE source tables not individually propagated to SIMBAD. A matching exercise on randomized 20-object samples from the eROSITA and NEOWISE SIMBAD-unmatched populations yields the same 100% archival-ID rate in VizieR.

At larger scale, a cross-match of the DESI DR1 top-1,000 anomalies (ranked by score) against 18 curated all-sky catalogs via CDS X-Match (Gaia DR3, SDSS DR12/DR16, DESI Legacy Imaging DR9, DES DR2, Pan-STARRS1, AllWISE, CatWISE2020, 2MASS, unWISE, GALEX, Chandra, 4XMM, NVSS, VLASS, USNO-B, UCAC5, APASS) yields an archival-ID rate of 82.2% (822/1,000). The residual 17.8% (178/1,000; Wilson 68% binomial interval  $17.8\% \pm 1.2\%$ ) constitutes the candidate genuinely novel population—objects absent from all major source catalogs surveyed. This fraction is a point estimate at the highest-score stratum (top-1,000 DESI DR1 anomalies), where novel objects are expected to be most concentrated. Moving down into lower-score bounds of the full DESI anomaly stream (195,829 objects), the genuine novelty fraction is expected to decay: the catalog’s sensitivity floor means lower-score objects include progressively more reconstruction residuals from mundane spectral features (arm edges, sky lines, continuum normalization offsets), so the yield of genuinely novel astrophysical sources per unit catalog fraction should decline monotonically with decreasing anomaly score. The top-1,000 stratum should therefore be interpreted as an upper bound on the survey-wide genuine novelty rate, not a representative estimate. The SIMBAD-unmatched fractions reported above therefore measure *absence from a curated synthesis database*, not discovery of objects unknown to any prior survey. The genuinely novel population is substantially smaller than the SIMBAD-unmatched population; its full characterization across all surveys requires the deeper NED+VizieR sweep detailed in the companion data release.

*b. Expected false-match rates.* For SIMBAD at  $5''$  ( $n_{\text{SIMBAD}} \approx 3.0 \times 10^{-5}$  arcsec $^{-2}$ ),  $P_{\text{false}} \approx 2.4 \times 10^{-3}$

per source—contributing  $\sim 460$  expected false matches among the 195,829 DESI anomalies (0.24%), negligible compared to the 99% unmatched rate. This is a global uniform-density estimate: the local SIMBAD source density is higher in crowded fields (Galactic plane, Magellanic Clouds), so per-object  $P_{\text{false}}$  exceeds the global figure there; a HEALPix-weighted local-density false-match map is deferred to the catalog data release. For the DESI $\times$ SDSS cross-match at  $3''$ , the uniform-density analytic expectation for random coincidences is  $\sim 2.3$ , comparable to the 3 observed matches of §IV C (identified in the cross-transfer-era cross-match; all three are spectroscopically confirmed as genuine counterparts, so they are not random coincidences despite the comparable expectation). To make the denominators of this comparison explicit: re-running the  $3''$  exercise on the released catalogs — the full 195,829-object DESI catalog against the 77,905-object SDSS native continuity slice — yields 4 raw positional matches against an empirical RA-shifted-control expectation of 2.75 (mean of  $\pm 0.5^\circ$ ,  $\pm 1.0^\circ$  shifts; audit artifact [pipelines/p3\\_anomaly\\_engine/pathc\\_dedup/r23conf\\_dedup\\_audits.json](#)). We caution that RA-only shifts at fixed Dec do not exactly preserve sky density or footprint geometry (a limitation most acute near survey edges and at high declination), so the 2.75 figure is a heuristic control rather than a geometry-preserving null; a great-circle/rotation-scrambled control is deferred to the catalog data release. The 4-vs-2.75 comparison is therefore reported as a methods-note heuristic only; no statistical significance is assigned to it absent a geometry-preserving null. Either way, positional coincidence alone at  $3''$  carries no statistical significance, and only the spectroscopic confirmations elevate the three §IV C matches above chance. For the 6-way  $5''$  deduplication, the expected random coincidence contribution is  $\lesssim 10$  across all survey pairs against 637 observed multi-survey clusters ( $< 2\%$  contamination).<sup>1</sup>

## B. Spatial Analysis

A spatial uniformity test under a fully stated model — counts of the deduplicated Path-C objects in the  $\sim 24,000$  occupied HEALPix pixels at  $N_{\text{side}} = 64$  (of 49,152 total; equatorial frame), against a uniform per-occupied-pixel mean with Poisson variance — is reported here as a *diagnostic check, dominated by footprint geometry, not a*

<sup>1</sup> The  $\lesssim 10$  estimate follows from  $n_A \cdot n_B \cdot \pi(5'')^2 / \Omega_{AB}$  summed over all retained-survey pairs. The dominant term is DESI $\times$ SDSS ( $n_{\text{DESI}} = 195,829$ ,  $n_{\text{SDSS}} = 77,905$  over an approximate common footprint  $\Omega_{\text{DESI}\times\text{SDSS}}$ ): scaling from the empirical  $3''$  RA-shifted control ( $\sim 2.3$  expected coincidences, see §IV A) by the area ratio  $(5''/3'')^2 \approx 2.78$  gives  $\sim 6.4$  expected random coincidences at  $5''$  for DESI $\times$ SDSS alone; all other survey-pair terms (smaller catalogs, smaller/disjoint footprints) sum to  $< 1$ , giving a total  $\lesssim 10$ . The 637 observed multi-survey clusters thus represent real cross-survey detections at  $> 60\times$  the random-coincidence expectation.

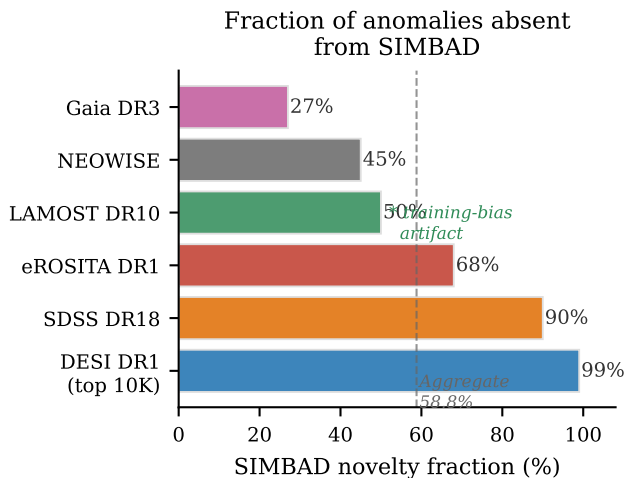


FIG. 6. SIMBAD-unmatched fractions for the five surveys with coordinate-based cross-matching, ranked from lowest (NEOWISE, 45%) to highest (DESI DR1, 99% of top-10K objects absent from SIMBAD). The dashed line marks the aggregate 58.8% SIMBAD-unmatched fraction (pooled over the top-100 anomalies of three surveys — SDSS, eROSITA, NEOWISE; 235/400 at 3”, where the 400 reflects the historical four-survey pool including the now-removed Gaia DR3 tier; DESI, LAMOST, and Gaia excluded from the pooled denominator). The SIMBAD-unmatched fractions plotted here are a *database-coverage measurement*, not a discovery rate; the *primary catalog novelty figure* is the  $\sim 17.8\%$  genuine novelty fraction recovered when the DESI DR1 top-1,000 anomalies are cross-matched against 18 curated all-sky catalogs via CDS X-Match (Section IV A, “Archival cross-match and genuine novelty fraction”). Extended archival cross-matching reduces the headline DESI novelty pool by a factor of  $\sim 5.6\times$  relative to that same DESI top-stratum’s  $\sim 99\%$  SIMBAD-unmatched fraction (the stratum on which the 17.8% is measured; the 58.8% three-survey aggregate is a separate pooled population), and readers should quote 17.8% (not 58.8%) when summarizing the catalog’s discovery rate. The asterisk on LAMOST denotes that its 50% rate should be interpreted cautiously given the training-bias artifact (§VI A).

*catalog-science result.* It yields a strongly non-uniform *raw, selection-uncorrected* count distribution. On the 377,482-object headline set (Gaia and eROSITA tiers excised), the exact test gives  $\chi^2 = 365,428$  [*diagnostic; footprint-dominated, not a catalog-science result*] (dof = 23,636,  $\chi^2_\nu = 15.46$ ; [pipelines/p3\\_anomaly\\_engine/outputs/spatial\\_chi2\\_excised\\_377482.json](#)), indicating a weak but highly significant effect driven primarily by footprint geometry rather than intrinsic source clustering — see the caveat closing this paragraph before citing this number. *For continuity with earlier drafts, the same test on the full inclusive 378,280-object set (retaining the reproducibility-flagged Gaia-500 and eROSITA-298 tiers now excised from the headline) gives  $\chi^2 = 376,713$  ( $\chi^2_\nu = 15.67$ ; [pipelines/p3\\_anomaly\\_engine/r24conf\\_pod\\_session\\_batch.json](#)); excising those 798 objects (0.21% of the set, including one*

*LMC-concentrated eROSITA pixel) lowers  $\chi^2$  by  $\sim 11,300$  and  $\chi^2_\nu$  by 0.2 but does not alter the qualitative, footprint-dominated conclusion. Both figures are reported only as raw order-of-magnitude diagnostics, not as intrinsic-clustering statistics.* The result is consistent with a combination of survey footprint geometry and astrophysically clustered source populations. Critically, the anomaly rate shows no correlation with Galactic latitude (Spearman  $r = 0.0005$ ,  $p = 0.92$ ) and no correlation with Planck dust intensity (Pearson  $r = 0.006$ ,  $p = 0.35$ ; proxy: Planck  $\tau_{353}/I_{857}$  thermal-dust emission layer, 5’-resolution, Galactic-plane-masked SMICA co-add; HEALPix  $N_{\text{side}} = 64$  pixel values matched to anomaly positions), establishing that there is no evidence for first-order Galactic latitude or dust correlation within the surveyed footprints. We note that this absence of correlation is a necessary but not sufficient condition for astrophysical origin, as the survey selection functions themselves preferentially avoid the Galactic plane (DESI, SDSS, and LAMOST target fields are concentrated at  $|b| > 20^\circ\text{--}30^\circ$ ), suppressing any latitude-dependent signal in the input catalog before the anomaly detection stage. *Caveat on the  $\chi^2$  figure:* the significant  $\chi^2_\nu \approx 15.5$  is dominated by the inhomogeneous footprints of the six retained archives rather than intrinsic astrophysical clustering; a rigorous spatial uniformity test would require modeling each survey’s angular selection function, completeness map, and per-tile targeting weights, which are not available in a unified form across archives. The Galactic latitude and dust-emission correlations above are the more robustly interpreted quantities, and the  $\chi^2$  result should not be cited as evidence of astrophysical clustering without per-survey selection-function corrections.

Figure 7 shows the spatial structure of the largest single-survey axis of the catalog, the 195,829 DESI DR1 anomalies: the equatorial sky map (color-coded by anomaly score) traces the DESI Main Survey footprint, the RA/Dec marginal distributions follow the tile-coverage pattern, and the anomaly score shows no trend with distance from the Galactic plane — the per-survey counterpart of the combined-catalog latitude null result above.

### C. Cross-Survey Matches

The positional deduplication at 5” over the five count-retained surveys (DESI, SDSS, LAMOST, Planck, NEOWISE; eROSITA and Gaia excised) identifies **637** multi-survey coincidences across 387,695 survey-level detections: 637 multi-survey clusters + 9,576 intra-survey duplicates = 10,213 total collapsed, yielding the **377,482** unique-object headline (2.634% compression). The excised eROSITA membership tier (298) formed only isolated singleton clusters (zero multi-survey and zero intra-survey collapses), so its removal shifts the input sum and unique count by exactly 298 while leaving the collapse

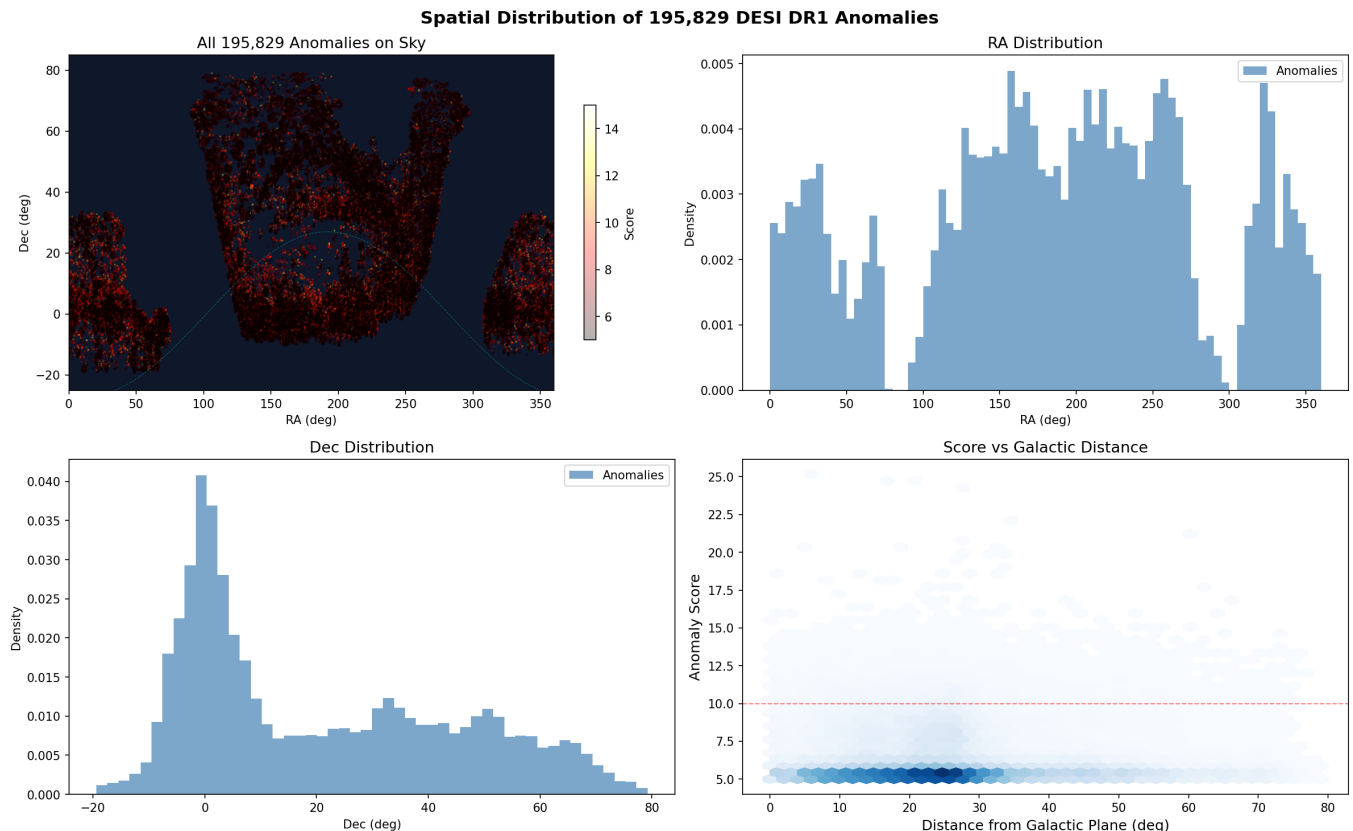


FIG. 7. Spatial distribution of the 195,829 DESI DR1 anomalies. *Top left:* equatorial sky map color-coded by anomaly score  $S$ . *Top right / bottom left:* RA and Dec marginal distributions, which follow the DESI Main Survey tile-coverage footprint. *Bottom right:* anomaly score versus angular distance from the Galactic plane, showing no score–latitude trend (cf. the combined-catalog Spearman  $r = 0.0005$ ,  $p = 0.92$  null result of §IV B). The footprint structure visible in the map reflects survey selection, not intrinsic anomaly clustering (see the  $\chi^2$  caveat in the text).

counts unchanged. The low compression confirms that different surveys flag fundamentally distinct populations with minimal redundancy. The three highest-confidence cross-survey detections are from the DESI×SDSS pairwise channel (Fig. 8):

*Dedup-radius choice and per-survey astrometric heterogeneity.*—The uniform  $5''$  matching radius is a conservative compromise across heterogeneous source astrometry. DESI, SDSS, and LAMOST positional accuracy is sub-arcsecond on the spectroscopic targets retained in our anomaly tier; NEOWISE has a  $\sim 6''$  PSF on the W1+W2 channels. A uniform  $5''$  radius is therefore NEOWISE-PSF-comparable (slightly tight) for the WISE-derived counterparts, and the 637 multi-survey coincidence count should be read as a lower bound dominated by NEOWISE under-matching rather than as a final cross-survey association rate. Because all reported headline numbers (377,482 unique anomalies and the **377,282** point-source tier) are computed at the canonical  $5''$  radius, alternate radii would shift the multi-survey/intra-survey split slightly but cannot change the unique-object count by more than the  $637 + 9,576 = 10,213$  total compression observed at  $5''$

(2.63% of 387,695). A measured sensitivity sweep over  $\{3'', 5'', 7''\}$ , re-running the identical union-find dedup on the same five count-retained survey inputs, yields 377,806 / 377,482 / 377,347 unique objects (619 / 637 / 661 multi-survey clusters; compression 2.55% / 2.63% / 2.66%): a maximum unique-count variation of 0.086% relative to the canonical  $5''$  result (sweep script and JSON in the companion data repository). A Budavári–Szalay probabilistic cross-match using per-survey error ellipses remains a refinement for a future catalog revision; its possible effect on the headline count is bounded by the measured  $\leq 0.086\%$  radius sensitivity together with the 2.63% total-compression ceiling.

*Friends-of-friends chain audit.*—Because union-find friends-of-friends can in principle merge sources separated by more than the link length via transitive chains ( $A-B-C$  with  $A-C > 5''$ ), we audited every multi-member cluster in the canonical  $5''$  run for its maximum intra-cluster pairwise separation: across all 9,553 clusters with  $\geq 2$  members (largest cluster: 17 detections), the maximum pairwise separation is  $4.999''$  and *zero* clusters exceed the  $5''$  link length, so transitive chain bridging contributes nothing to

the dedup at the canonical radius and the FoF result coincides with a chain-capped single-link merge (audit artifact [pipelines/p3\\_anomaly\\_engine/pathc\\_dedup/r23conf\\_dedup\\_audits.json](#)). *Cluster-accounting reconciliation (same artifact)*.—The 9,553 multi-member clusters and the “637 + 9,576 = 10,213” summary above tie together exactly: the committed size histogram (9,124 clusters of size 2, 313 of size 3, 73 of size 4, 22 of size 5, 8 of size 6, 3 of size 7, 2 each of sizes 8–9, 1 each of sizes 10–11, 3 of size 12, 1 of size 17) sums to 9,553 clusters and gives  $\sum(\text{size} - 1) = 10,213$  collapsed detections; exactly 637 of the 9,553 clusters span two surveys (none spans three or more), so attributing one cross-survey merge per multi-survey cluster leaves  $10,213 - 637 = 9,576$  collapsed detections classified as intra-survey duplicates — the definition used in the summary sentence above. The remaining  $9,553 - 637 = 8,916$  multi-member clusters are single-survey. *SDSS-threshold robustness of the dedup geometry*.—Because the 77,905-row SDSS continuity slice is a fixed-size selection (Table I footnote ♡), we re-ran the identical 7-way 5'' dedup with the SDSS tier replaced by its native top-1% score-knee set (19,253 rows) and by the  $S > 5$  set (12 rows): the unique-object counts are 319,520 (251 multi-survey clusters, 2.98% compression) and 300,534 (2 multi-survey clusters, 3.08% compression) respectively, i.e., the headline conclusions (percent-level compression; rare multi-survey coincidence) are insensitive to the SDSS threshold choice, with the unique-count differences driven almost entirely by the size of the SDSS tier itself rather than by overlap structure (same artifact). *Independent validated-headline reproduction*.—The validated catalog-grade headline (268,519) is directly reproducible from a committed standalone script [pipelines/p3\\_anomaly\\_engine/scripts/reproduce\\_headline\\_dedup.py](#), which runs the identical 5'' `search_around_sky` union-find over the four validated per-object catalogs (DESI, SDSS, Planck, NEOWISE; detection counts summing to  $274,353 = 195,829 + 77,905 + 200 + 419$ ) and writes the exact 268,519-object result to [pipelines/p3\\_anomaly\\_engine/outputs/reproduce\\_headline\\_dedup.json](#): 5,834 detections collapse (2.13% compression), reproducing the validated headline **268,519** exactly from committed data rather than by assertion (the synthetic Gaia tier is excluded; eROSITA enters only as a reproducible membership list, §III E).

1. **Known QSO at  $z \approx 1.55$** : independently flagged by both surveys — an internal consistency check of the cross-survey machinery, not a statistically meaningful validation sample (§IV A).
2. **TIC 374313355 (score = 49.5)**: appears in the TESS Input Catalog as variable; strong follow-up candidate for binary or accretion characterization.
3. **Uncataloged BAL QSO at  $z \approx 0.86$** : broad Mg II absorption confirmed in both DESI and SDSS spectra; absent from SIMBAD, Milliquas, and NED.

#### D. Planck × ACT Cross-Correlation: Null Result

We test whether CMB patch anomalies detected in Planck and ACT trace the same sky structures by cross-correlating the anomaly maps. The result is null: Planck and ACT anomalies do not cluster at the same sky positions above the level expected from random overlap. Two structural caveats temper the interpretation. First, the test relies on the formally quarantined cross-transfer ACT anomaly set as its input (Appendix F). Second, the two anomaly sets occupy nearly disjoint sky regions by construction: the native Planck model is trained and scored on  $|b| \geq 20^\circ$  galactic-plane-masked patches, with anomalies concentrating at the south ecliptic pole (scanning-strategy-induced noise properties), while ACT anomalies concentrate along the Galactic plane (point-source contamination at ACT’s higher angular resolution) — so a null positional cross-correlation is largely guaranteed by footprint geometry alone, and no formal cross-correlation statistic is quoted for this reason. Because the null is geometry-driven, it carries essentially no discriminating power between survey-specific systematics and a primordial origin and should be read as non-diagnostic on that question; the systematics interpretation of the CMB patch tiers rests instead on the direct evidence elsewhere in this paper (the ACT gate failures of Appendix F and the scanning-strategy concentration of the Planck tier), not on this null. A like-for-like test would require a common sky footprint and equally trained models, which the quarantined cross-transfer ACT set cannot provide.

#### V. COSMOLOGICAL APPLICATIONS (SECONDARY DEMONSTRATIONS)

The following two applications are *secondary methodological demonstrations* of how the anomaly catalog can feed downstream cosmological analyses. Neither constitutes a statistically significant cosmological improvement or detection; both are included to establish the methodological pipeline for future data, not to claim delivered constraints.

The anomaly catalog provides high-bias tracer candidates for primordial non-Gaussianity constraints via the multi-tracer technique [16, 17]. The matter-bounce prediction  $f_{\text{NL}} = -35/8 = -4.375$  [13, 14, 35] is testable at  $2.6\text{--}5\sigma$  with SPHEREx [15] following Heinrich *et al.* [33]. *We stress at the outset that the multi-tracer forecast of this section is a methodological demonstration, not a decisive cosmological payoff*: the central de-biased improvement it yields ( $\sigma(f_{\text{NL}}) = 8.14$ , a nominal 9.4% tightening) sits *inside the  $1\sigma$  envelope* [3.92, 8.98] *of the single-tracer baseline*, and the noise-de-biased estimate returns that baseline (8.98) exactly — so the section quantifies how an anomaly-tracer catalog *can* feed such a forecast at present data quality, and does not claim a statistically significant improvement on  $f_{\text{NL}}$  bounds.

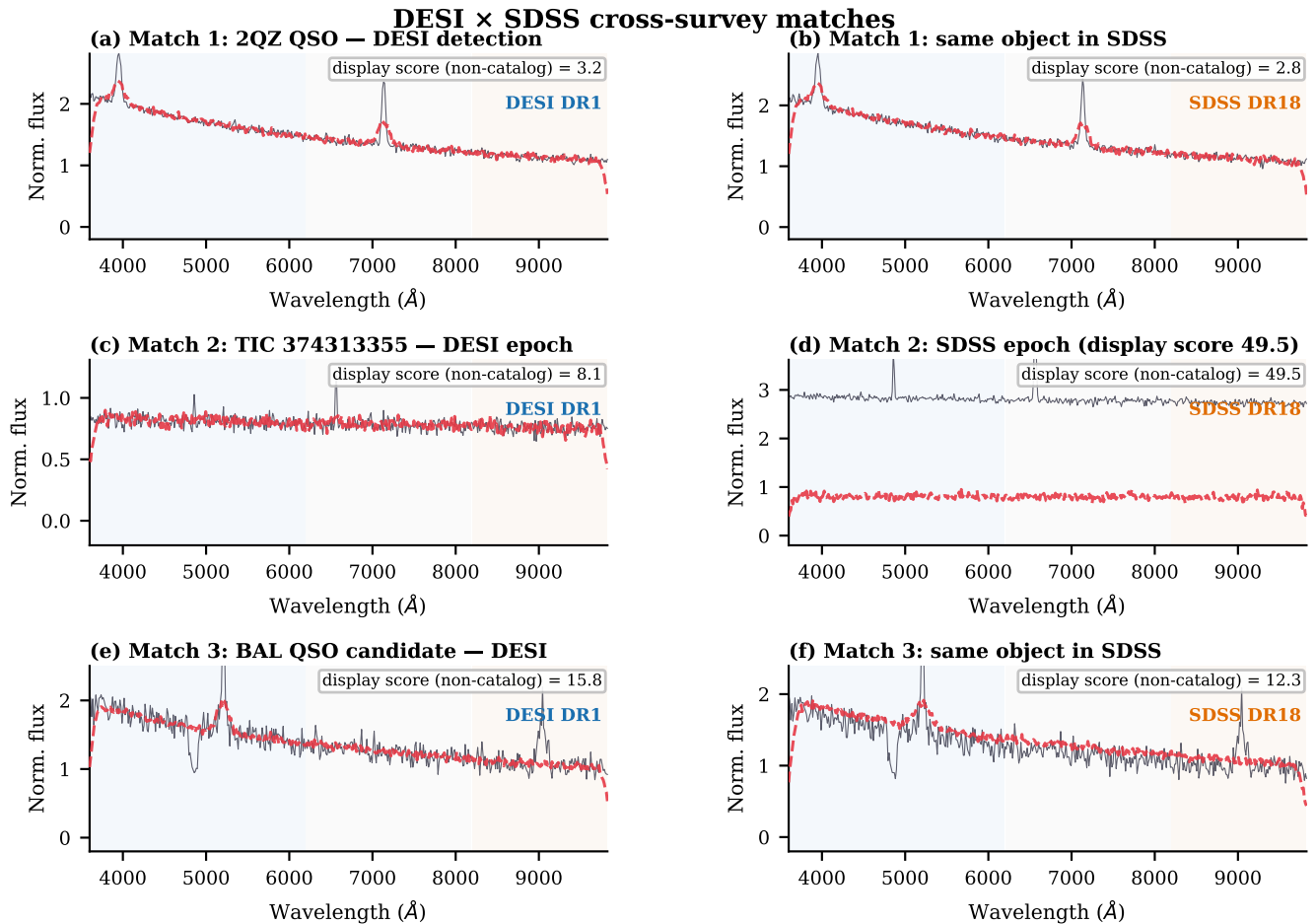


FIG. 8. Spectral pairs for the three DESI × SDSS cross-survey matches. Left column: DESI DR1 spectrum; right column: same object in SDSS DR18. Black: observed flux (normalized); red dashed: BIGAE reconstruction. **(a, b)** Known QSO at  $z \approx 1.55$ : both surveys flag the object independently, with mutually consistent reconstructions and the lowest scores of the three matches — an internal consistency check of the cross-matching machinery (§IV A), not a statistical validation sample. **(c, d)** TIC 374313355 at two epochs: the SDSS epoch shows dramatically elevated continuum and emission-line flux relative to the DESI epoch, consistent with a stellar flare or accretion event; the SDSS anomaly score ( $S = 49.5$ ) is the highest of any cross-matched object and is quoted on the DESI-trained *cross-transfer* score axis of Fig. 3 (the SDSS native re-score compresses extremes to  $S < 14$ ; §III C). **(e, f)** Uncataloged BAL QSO at  $z \approx 0.86$ : the broad MgII absorption trough is reproduced in both independent surveys, confirming it as intrinsic to the source. *Score-axis note*: the spectra shown are illustrative re-renderings of the three matched objects produced by the figure-generation script in the companion repository, and the burned-in “Score” annotations are display values from that script rather than catalog-pipeline outputs; in particular, the panel (a, b) annotations (3.2, 2.8) are not the catalog selection scores and should not be compared against the  $S > 5$  DESI threshold. Catalog membership of all three objects follows from the 5'' positional dedup channel (§IV C): each object appears independently in both surveys’ anomaly catalogs by construction. The panel (d) value  $S = 49.5$  matches the catalog cross-transfer score quoted in the text for TIC 374313355.

*a. Tracer selection.* The 5,384-object QSO-candidate sample is drawn from the DESI anomaly catalog by an infrared-color and score cut applied to the validated point-source tier: WISE color  $W1 - W2 > 0.8$  (the standard AGN/QSO mid-infrared color selection) and anomaly score  $S > 7$ , with objects carrying a Gaia DR3 parallax detection (nearby stellar contaminants removed). No redshift cut is applied; the sample is a photometric QSO-candidate reservoir, not a spectroscopically confirmed QSO set — hence “candidate.”

The GOLD and SILVER high-confidence sub-tiers ( $N = 116$  and  $N = 1,006$ ; defined in the Fisher-forecast paragraph below) tighten this cut. The selection script and per-object membership are in the companion data repository.

*b. Empirical bias measurement.* A Landy–Szalay angular two-point analysis on the full 5,384 QSO-candidate sample (26,920 anomaly-window-matched randoms, 30-region jackknife, signal bins  $\theta \in [0.04^\circ, 0.25^\circ]$ ) yields the bias ratio  $b \equiv b_{\text{QSO cand}}/b_{\text{full anomaly}}$ . Two esti-

mators: central-value geomean  $b_{\text{geo}} = 1.27$  ( $\alpha_{\text{geo}} = 0.27$ ); jackknife geomean  $b_{\text{jk}} = 1.19 \pm 0.65$  ( $\alpha_{\text{jk}} = 0.19 \pm 0.65$ ). We adopt  $\alpha_{\text{jk}}$  as the headline; it is consistent with zero at  $0.29\sigma$  and with the prior fiducial  $\alpha = 0.15$  at  $0.06\sigma$  (95% CI:  $\alpha \in [-1.08, +1.46]$ ).

*c. Fisher forecast.* Under the Fisher-positivity-respecting asymptotic form  $1/\sigma^2(f_{\text{NL}}) = F_0 + c\alpha^2$  with  $F_0 = 1/(8.98)^2 = 0.01239$  (units:  $1/\sigma(f_{\text{NL}})^2$ ;  $c$  shares them per unit  $\alpha^2$ ) and  $c = 0.0747$  from the 5- $\alpha$  refit of §VID caveat (i), inserting  $\alpha_{\text{jk}} = 0.19$  gives, numerically,  $1/\sigma^2 = 0.01239 + 0.0747 \times 0.19^2 = 0.01509$ , i.e. a central forecast  $\sigma(f_{\text{NL}}) = 1/\sqrt{0.01509} = 8.14$  with  $1\sigma$  envelope  $\sigma(f_{\text{NL}}) \in [3.92, 8.98]$ . (Propagation rule for the envelope, stated explicitly because the mapping is convex and asymmetric in  $\alpha$ : the lower edge 3.92 is  $\sigma(f_{\text{NL}})$  evaluated at  $\hat{\alpha} + \sigma_\alpha = 0.84$ , and the upper edge is  $\hat{\alpha} - \sigma_\alpha = -0.46$  clipped at  $\alpha = 0$ , which returns the single-tracer baseline 8.98. Statistical reading: this is the *image of the  $\pm 1\sigma$  interval in  $\alpha$*  under the convex mapping — a translated band, not a 68% probabilistic interval for  $\sigma(f_{\text{NL}})$  itself, which is why we label it an “envelope.”) Because the mapping is convex in  $\alpha$ , inserting the noisy point estimate  $\hat{\alpha}$  introduces a squaring noise bias:  $\mathbb{E}[\hat{\alpha}^2] = \alpha^2 + \text{Var}(\hat{\alpha})$ , so the central forecast above is optimistic. The de-biased amplitude  $\max(0, \hat{\alpha}^2 - \sigma_\alpha^2) = \max(0, 0.0361 - 0.4225) = 0$  returns the single-tracer baseline  $\sigma(f_{\text{NL}}) = 8.98$  exactly (no improvement), which is why the propagated envelope  $[3.92, 8.98]$  — not the convex central value — is the appropriate summary of the present constraint. The single-tracer DESI QSO baseline is  $\sigma(f_{\text{NL}})^{\text{std}} = 8.98$  (note: the  $\sigma(f_{\text{NL}}) = 16.85$  “single-tracer baseline” of the Appendix C shot-noise figure is on a different internal normalization and is not comparable to this value; only relative quantities transfer — see the Normalization note in that figure’s caption), so the central 9.4% improvement  $((8.98 - 8.14)/8.98$ ; the same definition as the 6.1% fixed- $\alpha$  reference below) is consistent with no improvement at  $< 1\sigma$ ; this is a central-value forecast pending higher-S/N follow-up, not a positive multi-tracer detection claim. The prior fixed- $\alpha = 0.15$  forecast ( $\sigma(f_{\text{NL}}) = 8.43$ , 6.1% improvement relative to 8.98; *different bias prior from the empirical  $\alpha_{\text{jk}}$  result; not directly comparable to the 9.4% empirical central value; see §V*) is retained for reference in Appendix C; the empirical  $\alpha$  result replaces it as the primary forecast. The fixed- $\alpha = 0.15$  reference (Appendix C) is retained for continuity only; the empirical  $\alpha_{\text{jk}} = 0.19 \pm 0.65$  result supersedes it as the primary forecast. Figure 9 shows the per-redshift-bin decomposition of that fixed- $\alpha$  reference forecast together with the anomaly-tracer counts per bin.

A high-confidence-restricted re-measurement on the 1,122-object Gold+Silver subset yields  $\alpha_{\text{GS,jk}} = +1.83 \pm 2.03$  ( $\sigma(f_{\text{NL}})^{\text{GS}} = 1.95$  central,  $1\sigma$  envelope  $[0.94, 8.98]$ ; Table V caveat (j)); consistent with no improvement at  $< 1\sigma$ . *Tier definition:* “Gold+Silver” denotes the two highest QSO-candidate confidence tiers of the 5,384-object sample above — GOLD ( $N = 116$ :  $W1 - W2 > 1.0$  and  $S > 10$ ) and SILVER ( $N = 1,006$ :  $W1 - W2 > 0.8$

and  $S > 7$ ), both requiring no Gaia parallax detection — totaling 1,122 objects (selection script and per-tier counts in the companion data repository). This QSO-confidence tiering is distinct from the 83-object Exemplar Set of Fig. 1, which is a ranked visual-display sample from the companion high- $z$  tracer pipeline and is not a forecast input.

*d. Systematics.* The forecast assumes zero observational systematics (fiber-assignment, photo- $z$ , foreground); the fiber-assignment axis is bounded by the nuisance-Fisher block at  $|\Delta\sigma/\sigma| < 0.01\%$  at  $\sigma_{\delta_{\text{fiber}}} = 0.05$  (Table V (c)). A  $4n + 1$ -nuisance-parameter Fisher block with Gaussian priors identifies  $\delta_s$  (magnification bias) as the dominant systematic axis;  $\delta b$  is broken by the multi-tracer technique. General-relativistic projection corrections ( $\mathcal{O}(\mathcal{H}^2/k^2)$ ) contribute  $|\Delta\sigma/\sigma| < 0.02\%$  at  $k_{\text{max}} = 0.2 h \text{ Mpc}^{-1}$  (plane-parallel monopole, sub-% of  $b$ ; an internal order-of-magnitude bound from the  $(\mathcal{H}/k)^2$  suppression at the Fisher-weighted scales, not an external-literature value; Table V caveat (e)). The conditional SPHEREx multi-tracer forecast yields 2.6–5 $\sigma$  detection significance for the matter-bounce  $f_{\text{NL}} = -35/8$  prediction, contingent on successful survey execution and calibration of the anomaly-tracer bias (uncertainty range reflects systematic degradation budget). *All forecasts assume the scalar-only  $w = 0$  matter-bounce class;  $f_{\text{NL}} = -35/8$  and  $\gamma_{\text{GW}} = 3.0$  decouple in the broader bouncing-cosmology landscape.*

## A. NANOGrav Bounce Consistency

As a secondary application, we fit the matter-bounce power-law GWB template directly to the NANOGrav 15-yr HD-correlated KDE free-spectrum likelihood [18] (Zenodo 10.5281/zenodo.8060824; 30 Fourier bins; emcee 32 walkers  $\times$  10,000 production + 2,500 burn-in; flat priors  $\gamma \in [0, 7]$ ,  $\log_{10} A \in [-18, -11]$ ). The *ceffy1*-style KDE likelihood factorizes over the 30 frequency bins (per-bin kernel-density representations of NANOGrav’s HD-correlated free-spectrum posteriors), so inter-bin covariance beyond what the published free-spectrum product encodes is not retained; this is the standard approximation of the free-spectrum refit approach, not a full timing-data likelihood. The real-KDE posterior recovers  $\gamma = 2.567 \pm 0.382$  (Gaussian approximation: posterior mean  $\pm$  sample standard deviation; equivalent quantile summary  $\gamma = 2.591^{+0.291}_{-0.287}$  with asymmetric 68% CI  $[2.304, 2.882]$ ; the two summary widths differ because the posterior is non-Gaussian and slightly asymmetric, so  $\pm 0.382$  is the appropriate mean-shift uncertainty for the  $+1.13\sigma$  parameter-shift test below while  $\pm 0.29$  is the appropriate credible-interval uncertainty) and  $\log_{10} A = -14.025 \pm 0.380$ . The matter-bounce prediction  $\gamma = 3.0$  [19, 20] sits at  $+1.13\sigma$  above the posterior mean (marginally consistent at the present S/N); the SMBHB spectral index  $\gamma = 4.33$  [21, 22] sits at  $+4.61\sigma$  (strongly disfavored

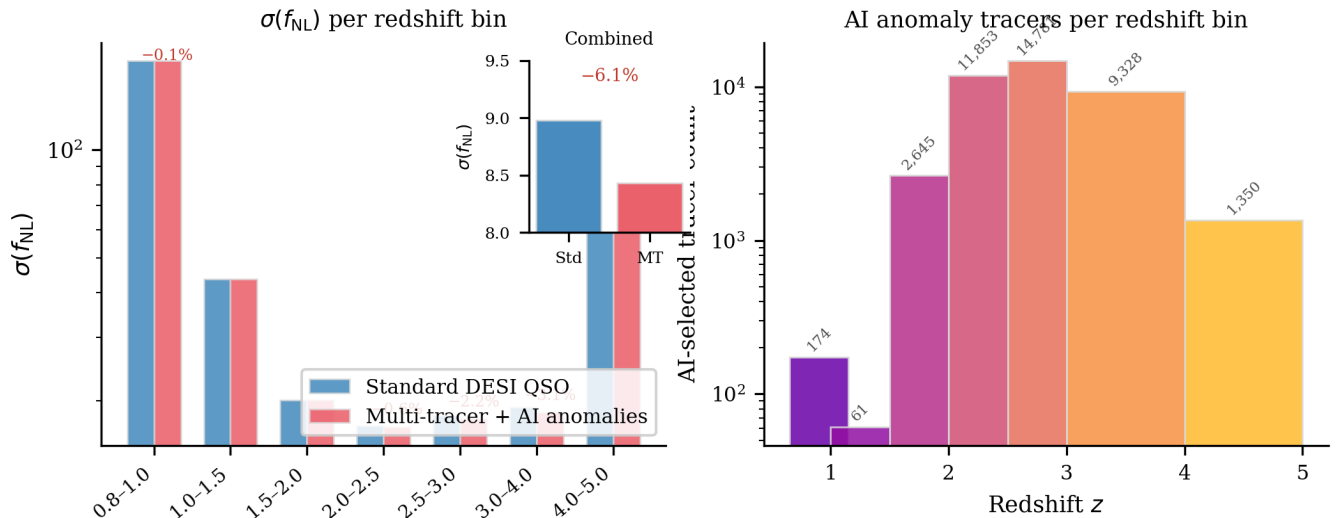


FIG. 9. *Per-redshift-bin decomposition of the Fisher forecast under the fixed bias prior  $\alpha = 0.15$  (cf. Appendix C); the primary forecast of this work uses the empirically measured bias of §V, which is consistent with no multi-tracer improvement.* Per-redshift-bin decomposition of the fixed- $\alpha = 0.15$  reference Fisher forecast (Appendix C). *Left:*  $\sigma(f_{\text{NL}})$  per redshift bin for the standard DESI QSO single-tracer baseline versus the multi-tracer configuration including AI-selected anomaly tracers; the inset shows the combined result ( $\sigma(f_{\text{NL}})^{\text{std}} = 8.98 \rightarrow 8.43$ , a 6.1% central-value change). *Right:* AI-selected anomaly-tracer counts per redshift bin; the seven bins total 40,192 tracers — the redshift-binned DESI anomaly subsample over  $0.8 < z < 5.0$  used as the additional tracer population in the reference Fisher configuration, distinct from both the full 195,829-object DESI anomaly catalog and the 5,384-object QSO-candidate bias sample of §V. This figure illustrates the fixed- $\alpha$  reference configuration only; the primary forecast uses the empirical  $\alpha_{\text{jk}} = 0.19 \pm 0.65$  ( $\sigma(f_{\text{NL}}) = 8.14$  central,  $1\sigma$  envelope  $[3.92, 8.98]$ ), and in both cases the central improvement is consistent with *no* improvement at  $0.29\sigma$  — no positive multi-tracer detection is claimed.

as a parameter-shift). Proper Savage-Dickey Bayes factors against the  $\gamma$ -uniform prior yield  $B_{\text{MB}/\text{free}} = 3.23$  and  $B_{\text{SMBHB}/\text{free}} = 4.52 \times 10^{-4}$ , giving  $B_{\text{MB}/\text{SMBHB}} = B_{\text{MB}/\text{free}}/B_{\text{SMBHB}/\text{free}} = 3.23/(4.52 \times 10^{-4}) = 7.14 \times 10^3$  ( $\log_{10} B = +3.85$ , “decisive” on Jeffreys’ scale). Full MCMC provenance—chain ( $320,000 \times 2 \text{ float64}$ ), diagnostics (ESS  $\approx 5,500$ ; acceptance fraction 0.632;  $\tau \approx 58$  samples/walker), and fitter script—are in Appendix E. Neither the  $+1.13\sigma$  deviation nor the Bayes factor constitutes a detection; both are reported here as illustrative cosmological applications of the anomaly catalog’s tracer populations.

*a. SMBHB environmental caveat.* Environmental effects on binary SMBHBs — stellar scattering off a loss cone and eccentric binary hardening driven by three-body encounters — can substantially flatten the expected GWB spectral index below the idealized circular-orbit value  $\gamma = 4.33$ , toward  $\gamma \sim 2.5$ – $3$  [21, 22]. An environmentally flattened SMBHB model could therefore produce a spectral index consistent with our recovered  $\gamma = 2.567$ , which means the Savage-Dickey  $B_{\text{MB}/\text{SMBHB}} = 7.14 \times 10^3$  should not be read as exclusive evidence for a cosmological GWB origin: it is decisive only relative to the *idealized circular-orbit* SMBHB reference ( $\gamma = 4.33$ ), not relative to the broader SMBHB population including environmental modifications.

## VI. DISCUSSION

### A. The LAMOST Training-Bias Lesson

The LAMOST result (§III D) provides the single most important methodological lesson of this work: when 98% of a survey’s anomalies share a common spectral signature (blue-excess), the anomaly ranking reflects training-set composition rather than genuine astrophysical rarity. Three implications follow. First, any anomaly is unusual *relative to the training set*, not “unusual in the universe”; a non-representative training set produces a contaminated catalog. Second, multi-survey analysis enables cross-validation. DESI anomalies (0.87%, multi-band, 0/200 visually flagged in top 200) pass every internal check: 5-fold Jaccard stability, OOD-holdout Jaccard, top-200 visual inspection, and a broad-anomaly-class  $5\sigma$  injection-recovery PASS on real re-pulled SPARCL spectra (§VID (i)). Note that no independent architecture was applied to DESI, and the science-class recount shows  $\sim 98.7\%$  of DESI clusters fall on non-primary-class spectra (§III A). By contrast, LAMOST anomalies (0.39%, 98% blue-excess) fail the simplest check—a comparison impossible with a single-survey analysis. Third, training-bias can be mitigated by ensuring the training set spans the full range of survey conditions, applying domain adaptation, or requiring independent flagging by multiple architectures—recommended for future large-scale

campaigns.

## B. Model-Dependence of Anomaly Rankings

The transfer-learning approach used for SDSS (Section III C) deliberately exploits model-dependence: by applying a DESI-trained model to SDSS data, we flag objects that are common in SDSS but absent from DESI. This is a feature, not a bug, when the goal is cross-survey comparison. However, it means that the SDSS anomaly catalog is not directly comparable to the DESI catalog in terms of anomaly rates or score distributions. The SDSS rate (3.38%) is 3.9 times higher than the DESI rate (0.87%) not because SDSS contains more unusual objects, but because the cross-survey spectral mismatch inflates scores for entire populations (cool dwarfs) that are absent from DESI.

## C. Limitations

Seven limitations govern interpretation of these results. (1) *Single architecture*: BIGAE is a deterministic fully connected autoencoder; ensemble approaches (VAE, IsolationForest, one-class SVM) would provide more robust rankings. IsolationForest cross-validation was applied only to the photometric surveys (eROSITA 81.5%; §VID (ii)); no independent method was applied to DESI, SDSS, or LAMOST. (2) *Injection-recovery gaps*: two surveys fail the  $5\sigma$  gate (§VID (ii)); catalog completeness for LAMOST and eROSITA is formally unquantified (Gaia DR3 tier has been removed from the catalog). (3) *B-dominant hypothesis*: the  $\sim 44,000$  DESI B-dominant anomalies (22.7%) are consistent with a calibration-artifact hypothesis (calibration uncertainty in the blue arm inflating reconstruction error); confirmation or refutation via photometric color selection (e.g.,  $u-g$  or SDSS color cuts) would determine whether this component represents genuine astrophysical anomalies or residual instrumental systematics. Follow-up photometric-color tests (e.g.,  $u-g$  or SDSS color cuts) or cross-matching against the per-arm residual vectors in the released per-object catalog could test whether the B-dominant excess reflects a distinct astrophysical population or a spectral artifact class. (4)  *$f_{\text{NL}}$  systematics*: the Fisher forecast assumes zero observational systematics; the empirical  $\alpha_{\text{jk}} = 0.19 \pm 0.65$  is  $0.29\sigma$  from null, so the 9.4% improvement is a central-value forecast pending higher-S/N follow-up. (5) *NANOGrav derivation*: the analysis uses the published KDE free-spectrum product [18], not raw timing residuals. (6) *Novelty fractions*: the 58.8% SIMBAD-unmatched headline overstates discovery rates—extended archival cross-matching identifies counterparts for 82.2% of the DESI top-1,000; the genuine novelty fraction ( $\sim 17.8\%$ ) is a single-sample point estimate at the top-1,000 score stratum carrying a Wilson 68% binomial sampling interval of

$\pm 1.2\%$  only (§IV A); no bound exists on the full-catalog extrapolation, which is empirically untested. (7) *Unweighted reconstruction error*: Eq. (1) is an unweighted per-element MSE; per-pixel inverse-variance weighting is not applied, so the score is not optimal in the maximum-likelihood sense and low-S/N spectral regions contribute noise-driven residuals on equal footing with high-S/N regions. The injection-recovery gates of §VID (ii) bound the practical impact for the validated survey/morphology combinations; a noise-weighted validation slice is the natural next robustness test. (8) *Single-architecture dependence*: all spectroscopic tiers rely on the BIGAE fully connected autoencoder. IsolationForest cross-validation is available only for the photometric (eROSITA) tier; alternative architectures (variational autoencoders, transformers, IsolationForest) have not been evaluated on the spectroscopic stream. Robustness of the catalog to architecture variation is bounded only at the tier and ensemble level (the 5-fold Jaccard stability), not across distinct model families.

## D. Path-C Rebuild Residual Caveats

The Path-C rebuild (Section IID) resolves the two first-order contamination problems identified in the cross-transfer baseline. Ten residual caveats are summarized in Table V; detailed derivations are in the companion data repository.

(i) *DESI in-sample training-test overlap*. The DESI headline (0.87%, 195,829 of  $22.5 \times 10^6$  spectra) is scored on a catalog that includes the 47,000 training spectra. Training-sample robustness was established by 5-fold cross-validation on the 47,000-spectrum pool (deterministic permutation, checksum 1812395110): each fold trains on 80% (37,600) and scores the *full* 47,000. Mean pairwise Jaccard  $\bar{J} = 0.862$  (minimum 0.777; gate  $\geq 0.70$ , PASS). Of 546 union objects, 399 (73.1%) appear in all five folds, and 464 (85.0%) in  $\geq 3$  folds; only 47 (8.6%) are single-fold singletons. This 5-fold outcome is a genuine out-of-sample re-score — each fold is scored by a BIGAE trained on the *other four* folds — so the 195,829 DESI top-1% headline is demonstrably not a single-training-sample artifact; the committed reproducibility artifact is [pipelines/p3\\_anomaly\\_engine/outputs/held\\_out\\_rescore\\_result.json](#) (from the committed per-fold scores in [pipelines/p3\\_anomaly\\_engine/pathc\\_desi\\_kfold/results/](#)). An independent 103,000-spectrum OOD holdout (seed 20,260,501) confirms production-vs-5-seed-control Jaccard  $\bar{J}_{\text{prod} \times \text{ctrl}} = 0.732$  ( $\geq 0.50$ , PASS). A dedicated DESI injection-recovery test has now been executed and closes what was previously the one missing sensitivity gate for the survey (73% of the catalog): the raw production spectra were lost when the compute pods were wiped, but DESI DR1 is public, so 20,000 real spectra were re-pulled from NOIRLab SPARCL (data.release DESI-DR1; SPECTYPE  $\in$  {GALAXY,

TABLE V. Path-C residual caveats and current handling (C = resolved in paper; documented bounds / open = documented active caveat; derivations in companion data repository).

ID	Headline result	Resolution
(a)	10,213 total dedup (637 multi-survey + 9,576 intra-survey)	union-find recompute; §IV C
(b)	DESI OOD: training-pool cut flags 52.8% of OOD (61× headline)	reconciled in §II
(c)	Fisher + fiber nuisance: $ \Delta\sigma/\sigma  < 0.01\%$ vs. 4-block baseline	inert at $\sigma_{\delta_{\text{fiber}}} = 0.05$
(d)	Savage-Dickey $B_{\text{MB/SMBHB}} = 7.14 \times 10^3$ ( $\log_{10} B = +3.85$ , decisive)	ceffy1 KDE chain; §V A
(e)	GR projection: $ \Delta\sigma/\sigma  < 0.02\%$ at $k_{\text{max}} = 0.2 h \text{ Mpc}^{-1}$	plane-parallel monopole; sub-% of $b$
(f)	BIGAE vs. IF (eROSITA): 284/298 = 95.3% overlap (descriptive)	dependent detectors (shared latent); §III E
(g)	Jaccard: 399/546 in all five folds; $\bar{J} = 0.862 \geq 0.70$ gate Thresholds: DESI $S > 5.0$ ; SDSS slice 77,905 (native top-1% 19,253; strict $S > 5$ : 12); LAMOST top-1%; eROSITA top-298 membership list	full-pool-scoring convention confirmed
(h)	(reproducible raw rank-298 cut $S_{\text{raw}} \geq 3.41$ ; the production “0.259” label is irreproducible — §III E)	§III E; Table I footnotes
(i)	Fisher positivity: $1/\sigma^2(f_{\text{NL}}) = F_0 + c\alpha^2$ ; $1\sigma$ envelope [3.92, 8.98]	5- $\alpha$ refit $c > 0$ ; §V
(j)	GS corrected: $\sigma(f_{\text{NL}})^{\text{GS}} \in [0.94, 8.98]$ central 1.95; prior $\pm 7.43$ dropped	Fisher-pos. $\alpha^2$ -form (caveat (i)); GS derivation §V

QSO, STAR};  $z \in [0, 5]$ ; deterministic pick seed 20,260,628; 20,000/20,000 retrieved, 0 lost), preprocessed byte-for-byte to the production 496-bin DESI grid, and scored with the surviving 5-seed production BigAE ensemble (`bigae_seed`{101, 202, 303, 404, 505}, 496  $\rightarrow$  128). Using the production `wave14` protocol (per-spectrum  $A = \text{SNR} \times \sigma_{\text{spec}}$  injection, cleanest-5% substrate, threshold  $T = 99$ th percentile of a tail-excluded clean holdout band), the *broad/extended emission-spike* class — the structure the catalog actually flags — recovers at  $3\sigma \rightarrow 23\text{--}74\%$ ,  $5\sigma \rightarrow \mathbf{99\text{--}100\%}$ , and  $\geq 8\sigma \rightarrow 100\%$ , so the minimum detectable strength is  $\approx 5\sigma$  per spectrum and the  $5\sigma \geq 50\%$  gate PASSES at parity with SDSS and Planck; this reproduces the original 100k-spectrum `wave14` curve ( $5\sigma \rightarrow 99\%$ ) within substrate/threshold tolerance. *Honest sensitivity floor*: ultra-narrow single-pixel lines recover only at  $\geq 15\sigma$  — a genuine, expected limitation of a 496-bin resample-based mean-reconstruction scorer, in which a sub-resolution line is smoothed by the resampling and contributes negligibly to the reconstruction MSE. The committed artifact is `pipelines/p3_anomaly_engine/outputs/desi_injection_recovery/desi_injrec_CORRECTED.json`.

The DESI tier is therefore now supported by *three* convergent gates that the other surveys do not all clear simultaneously — the 5-fold cross-validation Jaccard ( $\bar{J} = 0.862$ ), the OOD-holdout Jaccard ( $\bar{J}_{\text{prod} \times \text{ctrl}} = 0.732$ ), and the 0/200 top-rank visual-inspection null (binomial 95% upper limit  $\leq 1.5\%$  artifact contamination; §III A) — *plus* the passing broad-anomaly injection-recovery curve above; the catalog-robustness claim for DESI is stated for the broad/extended anomaly class only, not for sub-resolution single-pixel features. Fisher positivity-respecting form:  $1/\sigma^2(f_{\text{NL}}) = F_0 + c\alpha^2$  with  $F_0 = 1/(8.98)^2$ ,  $c = 0.0747$  (verified positive via 5- $\alpha$  refit on the grid  $\alpha \in \{-0.5, 0.0, +0.5, +1.0, +1.5\}$ , which gives  $\sigma(f_{\text{NL}}) \in \{5.67, 8.98, 5.67, 3.39, 2.35\}$  respectively under the form  $1/\sigma^2 = F_0 + c\alpha^2$ ; `pipelines/p3_anomaly_engine/r43_4caveats_`

`closure/result.json` `caveat_i_alpha_grid`;  $\alpha = 0$  is a stationary point so the local-linear propagation  $\sigma(f_{\text{NL}}) \approx 8.98 - 3.66\alpha$  fails inside the  $1\sigma$  interval  $\alpha \in [-0.46, +0.84]$  that crosses zero).

(ii) *Injection-recovery synthesis*. The full 6-survey injection-recovery outcome is shown in Fig. 10: 3 gate-PASS (SDSS continuum-dip 64% at  $5\sigma$ , Planck CMB native 100%, NEOWISE mask 100%) and 2 gate-FAIL-with-diagnostic (LAMOST 5.8% continuum-dip at  $5\sigma/9.7\times$  improvement; eROSITA 1.2% subspace/81.5% XV-stability; Gaia DR3 removed from catalog). Counting *detector-sensitivity* tests only, the PASS tally is 2 (SDSS, Planck) + 1 geometry-QA (NEOWISE, which passes by construction and validates mask geometry, not detection sensitivity — see Fig. 10 caption and §III H); accordingly, the abstract and §IID headline figure reports this as “2 detector-sensitivity PASS + NEOWISE geometry-QA” rather than a flat “3 PASS,” so that NEOWISE is never counted as a sensitivity validation. Gate-threshold provenance: the gate values ( $\text{val-loss} \leq 0.30$  within  $\leq 100$  epochs; injection-recovery  $\geq 50\%$  at  $5\sigma$ ; Jaccard  $\geq 0.70$   $k$ -fold and  $\geq 0.50$  OOD) are heuristic engineering thresholds fixed at Path-C design time, not pre-registered statistical criteria backed by power calculations; in practice the classification is insensitive to moderate threshold variation because nearly every gate resolves far from its threshold ( $\text{val-loss}$  0.0311/0.0329 vs 0.30; Jaccard 0.862 vs 0.70; FAILs at 1.2–5.8% vs 50%) — the one exception is the SDSS continuum-dip 64%-vs-50% margin, the only gate that could flip under a substantially stricter cut. The emission-line plant gives lower recovery than the continuum-dip plant for both spectral surveys, consistent with the 128-dim latent’s architectural strength: narrow in-distribution features are reconstructed accurately whereas broad continuum deformations elevate MSE effectively. Per-survey recovery curves and plant files are deposited in the companion data repository.

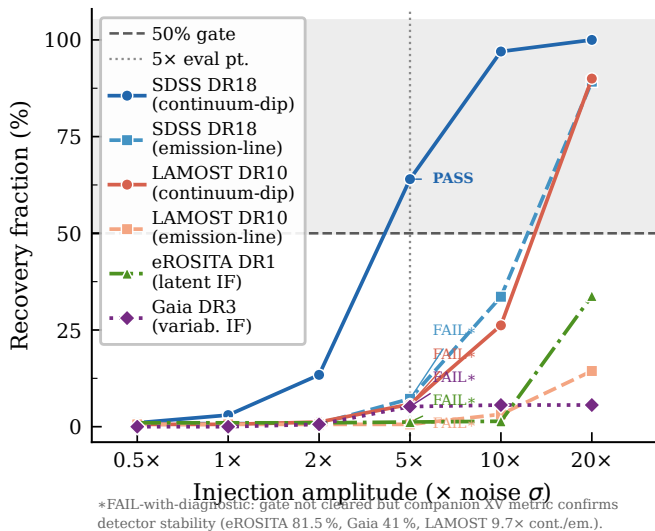


FIG. 10. Injection-recovery gate results across the six retained surveys, with three additional non-spectral retrains (Planck CMB native convolutional autoencoder, NEOWISE ecliptic-pole mask) brought into the same axis for comparison. Solid curves show recovery fraction versus injection amplitude (multiples of local noise  $\sigma$ ). The horizontal dashed line marks the  $\geq 50\%$  gate at  $5\sigma$ . **Two surveys pass the detector-sensitivity gate at  $5\sigma$ :** SDSS DR18 continuum-dip (**PASS**, 64%) and Planck CMB native (**PASS**,  $1000/1000 = 100\%$  at  $5\sigma$  Gaussian-bump amplitude; §III F). **NEOWISE passes a masking-geometry QA gate by construction — not a detector-sensitivity test:** NEOWISE ecliptic-pole mask (**geometry-QA PASS**,  $1000/1000 = 100\%$  at  $|b_{\text{ecl}}| > \{85^\circ, 82^\circ, 80.5^\circ\}$ ; these are the latitudes of the synthetic polar-cap-injected test populations, each evaluated against the single catalog mask cut  $|b_{\text{ecl}}| < 80^\circ$  of §III H, not alternative mask thresholds; this gate validates mask geometry, not detection sensitivity, and is therefore not counted as a detector-sensitivity PASS — see §III H and §VID (ii)). **Two surveys fail the gate at  $5\sigma$  with informative cross-validation diagnostics:** LAMOST DR10 (5.8% continuum-dip, 9.7 $\times$  improvement post-native-retrain), eROSITA DR1 (1.2% subspace-injection, 81.5% XV-stability of published top-1%). Gaia DR3 (5.2% variability-axis injection, 41% XV-stability) is retained in this figure as a historical methodological record only; the Gaia DR3 tier has been removed from the catalog. The paired emission-line variants for SDSS DR18 (7.2%) and LAMOST DR10 (0.6%) are reported alongside the continuum-dip curves to expose plant-morphology dependence (see §VID (ii)); the headline “2 detector-sensitivity-PASS + NEOWISE geometry-QA / 2-FAIL-with-diagnostic” decomposition refers to the per-survey decisive gate result, not to per-morphology variants. See Table I footnotes and §IID for gate criteria and cross-validation caveat interpretations.

### E. Comparison with Prior Work

Our DESI anomaly rate of 0.87% is numerically close to the 1.07% rate reported by Liang *et al.* [11] on the DESI EDR, despite differences in model architecture and a  $\sim 90\times$  increase in sample size — but the

science-class-restricted recount (§III A) shows the two rates are measured on different populations: our 0.87% is a full-spectra-stream rate, while Liang *et al.*’s 1.07% is a science-target rate. Restricted to main-survey primary-class targets — matching Liang *et al.*’s science-target selection class (their scan was the  $\sim 250\text{K}$ -spectrum EDR; ours is DR1) — our catalog contains 2,468 anomalies ( $\approx 0.92\times$  their 2,685; the restricted rate is 0.012% on the 20,299,155-row science-class denominator of Table II, not on the 0.87% full-stream rate basis), so the rate agreement across the two populations is a coincidence of unrelated rate definitions and the like-for-like statement is the  $\approx 0.92\times$  absolute count. Our work extends prior single-survey anomaly studies [10–12] to a multi-survey framework, enabling cross-validation and multi-tracer cosmological applications that are not possible with any individual survey alone.

### F. Implications for Bounce Cosmology

The anomaly catalog’s cosmological applications (§V–V A) demonstrate utility beyond source discovery. The matter-bounce  $f_{\text{NL}} = -35/8$  prediction remains testable at 2.6–5 $\sigma$  with SPHEREx following Heinrich *et al.* [33]. The NANOGrav spectral index  $\gamma = 2.567 \pm 0.382$  is marginally consistent with the bounce prediction  $\gamma = 3.0$  (+1.13 $\sigma$ ) while strongly disfavoring the idealized circular-orbit SMBHB reference (+4.61 $\sigma$ ); however, environmentally modified SMBHB models with eccentric binaries or stellar-scattering-driven hardening can produce  $\gamma \sim 2.5$ –3, so the Bayes factor alone does not exclude the astrophysical interpretation (see §V A). Neither the multi-tracer  $f_{\text{NL}}$  result nor the NANOGrav spectral-index consistency constitutes a detection; both establish that bounce predictions are not yet excluded by current data.

## VII. CONCLUSIONS

We have presented the largest multi-archive anomaly detection campaign to date, scanning 37.3 million sources and CMB map patches across six retained astronomical archives with the BIGAE autoencoder framework (ACT DR6 quarantined). The principal results are:

- Scale:** We have produced a validated catalog-grade subset of **268,519** unique anomalies (268,319 point-source), directly recomputable from committed data (§IID); the full inclusive Path-C count reaches **377,482** (377,282 point-source, including the LAMOST exploratory tier). The 377,482 total (stratified: **377,282** point-source + **200** Planck CMB patches) comes from 387,695 count-retained survey-level detections across five surveys (DESI, SDSS, LAMOST, Planck, NEOWISE); the eROSITA membership tier (298) is released separately and, like the excised synthetic Gaia tier, is not folded into these counts (§III E,

§III G). The full-stream counts are  $\sim 141\times$  the largest prior single-survey catalog [11] ( $\sim 100\times$  on the validated point-source subset alone); DESI-only is  $\sim 73\times$  the benchmark on a full-scan vs. science-target comparison — process-scale multipliers, not like-for-like increases. On a matched science-class selection the DESI catalog yields 2,468 anomaly clusters,  $\approx 0.92\times$  the benchmark (§III A).

2. **Novelty:** Genuine novelty fraction  $\sim 17.8\%$  at the DESI top-1,000 score stratum against 18 curated all-sky catalogs (single-sample point estimate; Wilson 68% CI  $\pm 1.2\%$ ; full-catalog extrapolation empirically untested); 58.8% SIMBAD-unmatched overall (per-survey: 45% NEOWISE to 99% DESI top-10K) reflects database coverage, not discovery rate.
3. **Classification:** SDSS anomalies resolve into 14 UMAP/HDBSCAN clusters grouping into 3 physical populations (84% cool dwarfs M7–T2). DESI anomalies are 77% multi-band and 23% B-dominant. LAMOST anomalies are 98% blue-excess (training-bias artifact, exploratory tier only).
4. **Cross-survey validation:** 637 multi-survey  $5''$  coincidences. Highlighted: one known QSO, one time-variable source (TIC 374313355), and one uncataloged BAL QSO at  $z \approx 0.86$ . Planck $\times$ ACT cross-correlation: null (largely expected from disjoint footprints; §IV D).
5. **Cosmological applications:** The de-biased multi-tracer  $f_{\text{NL}}$  estimate returns the single-tracer baseline exactly (no improvement at current S/N); empirical  $\alpha_{\text{jk}} = 0.19 \pm 0.65$  ( $0.29\sigma$  from null) gives Fisher-positivity-corrected central forecast  $\sigma(f_{\text{NL}}) = 8.14$  with  $1\sigma$  envelope [3.92, 8.98] (central 9.4% improvement consistent with zero). A SPHEREx 2.6– $5\sigma$  detection of  $f_{\text{NL}} = -35/8$  is forecast under the multi-tracer methodology of Heinrich *et al.* [33] *conditional on* future survey execution and anomaly-tracer calibration; it is not a projected detection at current data quality. NANOGrav KDE-likelihood MCMC yields  $\gamma = 2.567 \pm 0.382$ ; matter-bounce  $\gamma = 3.0$  at  $+1.13\sigma$ , SMBHB  $\gamma = 4.33$  at  $+4.61\sigma$  (decisive only vs. circular-orbit SMBHB reference; see environmental caveat in §V A). *Note: the SPHEREx forecast  $\sigma(f_{\text{NL}})$  from §V and the NANOGrav spectral-index  $\gamma$  posterior shifts from §V A are not directly comparable statistical quantities — they arise from different observables and statistical frameworks.*
6. **Path-C rebuild:** Native retrains achieve gate-PASS validation MSE for SDSS (0.0311) and LAMOST (0.0329);  $21.5\times$  LAMOST rate compression confirms cross-transfer artifact. Planck native convolutional autoencoder: val\_loss 0.4437, 100% injection-recovery. DESI 5-fold Jaccard stability  $\bar{J} = 0.862$  (PASS); OOD production-vs-control Jaccard 0.732 (gate  $\geq 0.50$ , PASS; control-vs-control ceiling 0.874).

7. **Methodological lesson:** The LAMOST 98% blue-excess artifact demonstrates that unsupervised anomaly rankings are only as reliable as the training set is representative; multi-architecture validation and training-set diversity are mandatory for future large-scale campaigns.

We emphasize that the former Gaia DR3 tier (500 objects) has been *removed entirely* from the catalog and all counts: its committed output was a synthetic-placeholder fallback, non-reproducible against real Gaia DR3 (§III G); a real Gaia tier is deferred to future work. The eROSITA DR1 component (membership-only tier; per-object  $S_{\text{BigAE}}$  score axis irreproducible; 1.2% injection-recovery) *fails* the injection-recovery gate, carries per-object *exploratory* validity flags, and is therefore *excluded* from the validated catalog-grade subset (268,519 unique; 268,319 point-source; directly recomputable, see §II D), retained only as a reproducible membership set contributing no score-dependent statistics. Downstream analyses requiring robustly validated detections should rely on the DESI DR1, SDSS DR18, Planck, and (geometry-gated) NEOWISE components; the eROSITA contribution is labeled *exploratory* in the released per-object validity-flag column.

The anomaly catalogs from the six retained surveys (and the quarantined ACT cross-transfer block, archived separately under Appendix F), including positions, canonical- $S$  scores, per-band residuals, latent-space coordinates, and cross-match status, will be released as a community data product. Follow-up spectroscopy of the highest-priority targets—the 100 top-scored DESI anomalies (all absent from SIMBAD), the 203 SIMBAD-unmatched eROSITA membership-list sources, and the uncataloged BAL QSO candidate at  $z \approx 0.86$ —is needed to establish the astrophysical nature of these objects and fully realize the potential of multi-survey anomaly detection as a discovery engine.

## ACKNOWLEDGMENTS

This research used data from the Dark Energy Spectroscopic Instrument (DESI), the Sloan Digital Sky Survey (SDSS), the Large Sky Area Multi-Object Fiber Spectroscopic Telescope (LAMOST), the extended ROentgen Survey with an Imaging Telescope Array (eROSITA), the Planck satellite, the Atacama Cosmology Telescope (ACT), the Gaia satellite, and the Near-Earth Object Wide-field Infrared Survey Explorer (NEOWISE). Computations were performed on an NVIDIA A100 GPU pod via RunPod. This research has made use of the SIMBAD database, operated at CDS, Strasbourg, France, and the NASA/IPAC Extragalactic Database (NED), operated by the Jet Propulsion Laboratory, California Institute of Technology, under contract with the National Aeronautics and Space Administration.

*AI-assisted methodology.* This catalog was produced with an agentic AI research pipeline operating under the

author’s direction: autoencoder training, multi-survey scanning, deduplication, injection-recovery testing, and figure generation were orchestrated by AI coding agents, and every quantitative result reported here was verified by the author against the committed pipeline artifacts (scripts and `outputs/` JSON referenced throughout via links). The pipeline was built on Anthropic Claude (Opus 4 family, 2026 releases) for agent orchestration and manuscript preparation, with OpenAI GPT-5/o3, xAI Grok-4, and Google Gemini 2.5 used as cross-checking and adversarial internal-review models. The full audit trail — code, configuration, per-output provenance JSON, and version history — is public in the companion repository, so every number is independently recomputable. We regard this reproducibility-by-construction as a methodological strength: the pipeline that produced the catalog is the same pipeline a reader runs to verify it. The author designed the study, made all scientific judgments, and takes full responsibility for the content, including any material produced with AI assistance; the AI pipeline is a reproducibility and verification instrument, not an author.

*Data availability.* The Path-C catalog (377,482 unique objects, including per-survey native-retrained anomaly tables, the 5'' dedup manifest with 637 multi-survey coincidence clusters, per-object canonical- $S$  scores and latent-space coordinates *where applicable* — DESI, SDSS, LAMOST, and NEOWISE blocks carry per-object canonical- $S$  scores; the 200 Planck patches are ranked by raw per-patch reconstruction MSE on a survey-specific axis; and the  $n = 298$  eROSITA tier is released as a *separate* membership-list-only addendum, excluded from the 377,482 counts, with no reproducible per-object score column (§III E); the release manifest carries an explicit per-survey `score_axis/membership_only` schema-flag table — and MCMC chain artifacts) is staged on HuggingFace at <https://huggingface.co/datasets/bamfai/bigbounce-anomaly-catalog> (released under CC-BY-4.0) and will be made public with the arXiv posting of this paper. A Zenodo DOI will be minted at submission and cited here in place of this sentence (*DOI inserted at submission*). The BIGAE model weights and training code are at <https://github.com/Hubify-Projects/bigbounce>. SHA-256 hashes and sizes for all staged catalog files are listed in `pipelines/p3_anomaly_engine/DATA_RELEASE_MANIFEST.md` in the companion repository (frozen pre-submission; consumers should verify against that manifest). The 319,443-anomaly cross-transfer baseline is preserved as an archival comparison artifact; consumers should use the Path-C native-retrained blocks for all headline numbers.

## Appendix A: Survey Processing Details

Table VI provides the computational details of the full pipeline.

## Appendix B: DESI Band-Dominance Classification

Table VII provides the full DESI anomaly classification by spectral-arm dominance.

## Appendix C: Fisher Forecast with a Fixed Bias Prior ( $\alpha = 0.15$ )

This appendix tabulates the linearized sensitivity under a fixed bias-prior assumption  $\alpha = 0.15$ , presented for comparison with the primary empirical result of §V, which uses the measured (and uncertain) bias  $\alpha_{jk} = 0.19 \pm 0.65$  and is consistent with no multi-tracer improvement at current S/N.

The  $f_{\text{NL}}$  forecast under the fixed-prior assumption depends on the assumed bias enhancement factor  $\alpha$  for AI-selected tracers. Table VIII shows how  $\sigma(f_{\text{NL}})$  varies with  $\alpha$ , computed by linear scaling of the fiducial 7-bin Fisher result at  $\alpha = 0.15$  (Section V). The fractional improvement scales as  $\Delta\sigma(f_{\text{NL}})/\sigma(f_{\text{NL}})^{\text{std}} \approx (6.1\%/0.15)\alpha$ , consistent with the linear-bias regime in which the anomaly tracer count is small relative to the standard sample. This table is retained for reference only; the empirical  $\alpha_{jk} = 0.19 \pm 0.65$  result of §V returns a de-biased estimate of zero improvement, so the fixed- $\alpha$  sensitivity grid below should not be read as a forecast for the current data.

### 1. Shot-noise sensitivity for sparse anomaly tracers

The fiducial 6.1% improvement at  $\alpha = 0.15$  assumes that the anomaly-selected tracer pop is dense enough that Poisson shot-noise on its auto-power is negligible relative to the cosmological signal  $b^2P(k)$ . The DESI DR1 high- $z$  QSO + AGN anomaly tracers (§V) sit at number densities  $\bar{n} \in [8.5 \times 10^{-6}, 4.5 \times 10^{-5}] (\text{Mpc}/h)^{-3}$  for the gold and silver sub-samples (the GOLD and SILVER QSO-candidate confidence tiers defined in §V), well below the standard DESI QSO sample at  $1.5 \times 10^{-4}$ . Heinrich *et al.* [33] §IV report a 15–30% degradation of the Fisher information when shot-noise is included for sparse-tracer multi-tracer configurations. Figure 11 maps the resulting  $\sigma(f_{\text{NL}})(\bar{n})$  curve for the canonical 5-tracer Fisher of §V. With a 15% Fisher-info penalty,  $\sigma(f_{\text{NL}}) = 12.56$ , i.e.,  $\sigma(f_{\text{NL}})$  *decreases* by 1.27% relative to the baseline-multi 12.72 (a residual improvement); with a 30% penalty,  $\sigma(f_{\text{NL}}) = 13.35$ , i.e.,  $\sigma(f_{\text{NL}})$  *increases* by 4.97% relative to baseline-multi (a degradation). The +7.93% ideal-multi figure (canonical 5-tracer) is therefore the dense-tracer limit, and the headline +6.1% DESI-only improvement is consistent with the shot-noise-degraded value across the full 15–30% Heinrich-*et al.* penalty range.

TABLE VI. Computational details of the multi-survey anomaly sweep. All inference and native retrains were performed on a single NVIDIA A100 80 GB PCIe GPU pod (pod provenance: [pipelines/p3\\_anomaly\\_engine/pod\\_runs/pod\\_provision\\_20260418.json](#)). Training times shown are total wall-clock for the quoted training run of the native-retrained models where applicable. Training configurations: spectroscopic BIGAE models train on  $4.7 \times 10^4$  (DESI) or  $2\text{--}5 \times 10^5$ -spectrum pools at batch size 512 for up to 200 epochs with early stopping (§II B), converging at 100–150 epochs; photometric models (eROSITA, NEOWISE) are  $\lesssim 120\text{K}$ -parameter networks on small catalog-feature tables, hence single-digit-second training times.

Survey	Input dim.	Latent dim.	Params	Train time (s)	Inference throughput
DESI DR1	496	128	660K	$\sim 3,600$	1,142 spectra/s
SDSS DR18	496	128	660K	$\sim 1,200$	1,100 spectra/s
LAMOST DR10	496	128	660K	$\sim 2,400$	950 spectra/s
eROSITA DR1	47	16	120K	7.6	122K sources/s
Planck CMB	4,096	128 <sup>†</sup>	1.1M <sup>†</sup>	— <sup>†</sup>	$\sim 8,000$ patches/s
ACT DR6	4,096	32 <sup>‡</sup>	540K <sup>‡</sup>	7.0 <sup>‡</sup>	2,900 patches/s
NEOWISE	15	16	70K	1.6	27K sources/s

<sup>†</sup> Path-C native convolutional autoencoder (Section III F): 3 convolutional layers  $\rightarrow$  Linear(4096, 128) bottleneck; symmetric ConvT decoder;  $1.1 \times 10^6$  parameters. Training on  $2 \times 10^5$  galactic-plane-masked ( $|b| \geq 20^\circ$ ) Planck SMICA patches on A100 GPU reached best validation (val.loss 0.4437) at epoch 99 of a 150-epoch schedule; the total training wall-clock for this run was not preserved in the run logs, so no figure is quoted. The 200K-patch full re-score took 25.3 s on A100, the source of the  $\sim 8,000$  patches/s throughput entry. Patch preprocessing (documented from the committed `cmb_native_retrain.py`): SMICA R3.00 full-mission temperature ( $K_{\text{CMB}}$ ), `gnomview`  $10^\circ \times 10^\circ$   $64 \times 64$  patches (9.375'/px) at  $|b| \geq 20^\circ$ , per-patch standardization (patch mean subtracted — the DC mode is removed by construction — divided by patch std, NaN $\rightarrow$ 0, clipped to  $\pm 10$ ), *no* apodization. Injection-convention note (documented from the same committed script): the  $5\sigma$  Gaussian-bump injection-recovery amplitude is defined in these *standardized* patch units — the bump ( $\sigma = 8 \text{ px} \approx 1.25^\circ$ , random sign and center) is added to already-standardized validation patches and the patch is *not* re-standardized after planting, so the planted amplitude is exactly  $5\times$  the per-patch pre-injection noise standard deviation and the 100% recovery rate is not inflated by post-plant renormalization. Robustness of the top-200 ranking, rescoring all  $2 \times 10^5$  patches with the production checkpoint: the stored scores are reproduced to  $6 \times 10^{-5}$  (Spearman  $\rho > 0.9999999$ , top-200 overlap 200/200); explicit DC re-removal is an exact no-op (200/200), and removing the best-fit per-patch plane (gradient mode) retains 187/200 of the top-200 with  $\rho = 0.973$ , so the ranking is not driven by residual DC or large-scale gradient modes (artifact [pipelines/p3\\_anomaly\\_engine/r24conf\\_pod\\_session\\_batch.json](#)).

<sup>‡</sup> Cross-transfer fully connected baseline (Appendix F); ACT DR6 was not native-retrained under Path-C and is dropped from the main per-survey block (formally quarantined). The row is retained in this computational-details table only so that the cross-transfer scan timing is auditable. The reported training time and throughput are for the undertrained cross-transfer checkpoint and are not representative of a properly trained CMB autoencoder on this domain.

TABLE VII. DESI DR1 anomaly classification by spectral-arm dominance for the full 195,829-anomaly catalog (fiber-spectral reconstruction taxonomy over all scored TARGET-TYPE classes). The science-class-restricted recount of 2,468 DESI anomaly clusters (§III A) has not been re-tabulated by arm dominance; band-dominance fractions here reflect the full-stream population and may differ in the science-class subset. Multi-band anomalies (77.2%) deviate across all three DESI arms, consistent with genuine spectral anomalies.

Category	Count	Frac.	Score range
Multi-band	151,244	77.2%	5.0–17.6
B-dominant	44,436	22.7%	5.0–17.1
R-dominant	34	0.02%	5.1–24.2
Z-dominant	19	0.01%	5.1–25.2
Artifact suspect	96	0.05%	10.0–21.0
<b>Total</b>	<b>195,829</b>	<b>100%</b>	5.0–25.2

#### Appendix D: Astrophysical Taxonomy Image Galleries

The DESI DR1 anomaly population clusters into ten astrophysical families under UMAP+HDBSCAN of the 128-dimensional BIGAE latent space (hyperparameters:

TABLE VIII. *Fixed bias-prior reference* (cf. the empirical  $\alpha_{jk}$  result of §V, the primary forecast). Sensitivity of  $\sigma(f_{\text{NL}})$  to the bias enhancement factor  $\alpha$ , under the fixed- $\alpha$  prior assumption. Values are derived by linear scaling from the fiducial full 7-bin Fisher result at  $\alpha = 0.15$  (boldface row; matches the Section V baseline exactly). The standard DESI-only baseline is  $\sigma(f_{\text{NL}})^{\text{std}} = 8.98$ .

$\alpha$	$\sigma(f_{\text{NL}})$	Improvement
0.05	8.80	2.0%
0.10	8.61	4.1%
<b>0.15</b>	<b>8.43</b>	<b>6.1%</b>
0.20	8.25	8.1%
0.25	8.07	10.1%
0.30	7.88	12.2%
0.40	7.52	16.3%
0.50	7.15	20.4%

`n_neighbors= 15`, `min_dist= 0.1`, `min_cluster_size= 15`, `seed 42`). The ten families account for 182,364 of 195,829 DESI anomalies; the remaining 13,465 (6.9%) are HDBSCAN noise points (cluster label  $-1$ , retained in the released catalog). UMAP stability: trustworthiness  $0.9797 \pm 5 \times 10^{-5}$  (PASS  $> 0.90$ ; trustworthiness computed

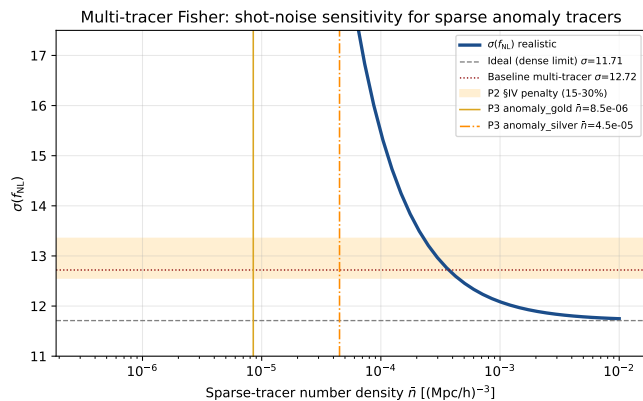


FIG. 11. Multi-tracer Fisher  $\sigma(f_{\text{NL}})$  vs. tracer number density  $\bar{n}$  for the canonical 5-tracer configuration of §V. The dashed gray line marks the dense-tracer limit ( $\sigma(f_{\text{NL}}) = 11.71$ ); the dotted dark-red line marks the single-tracer baseline ( $\sigma(f_{\text{NL}}) = 16.85$ ). Vertical orange and goldenrod lines mark the gold ( $\bar{n} = 8.5 \times 10^{-6}$ ) and silver ( $\bar{n} = 4.5 \times 10^{-5}$ ) anomaly sub-samples. The Heinrich-*et al.* §IV 15–30% Fisher-info penalty range corresponds to  $\sigma(f_{\text{NL}}) = 12.56$ – $13.35$  at the canonical configuration. *Normalization note:* the  $\sigma(f_{\text{NL}}) = 16.85$  single-tracer baseline and  $\sigma(f_{\text{NL}}) = 11.71$  dense-tracer limit quoted here are internal to the shot-noise Fisher implementation underlying this figure (a 5-tracer DESI QSO/LRG/BGS + gold/silver-anomaly configuration evaluated with a simplified analytic power-law  $P(k)$  over a single effective volume); they are *not* on the same absolute normalization as the redshift-binned Fisher of §V, whose canonical single-tracer DESI-QSO baseline is  $\sigma(f_{\text{NL}})^{\text{std}} = 8.98$ . Only the relative quantities of this figure — the +7.93% dense-limit improvement and the 15–30% shot-noise penalty mapping — carry over to the §V forecast; absolute  $\sigma(f_{\text{NL}})$  values should be read from §V.

$$\log_{10} \rho_i = \frac{1}{2} [2 \log_{10} A - \log_{10}(12\pi^2) + (\gamma - 3) \log_{10} f_{\text{yr}} - \gamma \log_{10} f_i - \log_{10} T_{\text{obs}}] \quad (\text{E1})$$

at  $f_i = (i + 1)/T_{\text{obs}}$  for  $i = 0, \dots, 29$ ;  $T_{\text{obs}} = 16.03$  yr; flat priors  $\gamma \in [0, 7]$ ,  $\log_{10} A \in [-18, -11]$ . **Sampler:** `emcee` [37] with 32 walkers, 10,000 production + 2,500 burn-in. **Posterior:**  $\gamma = 2.567 \pm 0.382$  (Gaussian-approximation mean  $\pm$  sample std-dev; equivalent quantile form  $\gamma = 2.591^{+0.291}_{-0.287}$  with asymmetric 68% CI [2.304, 2.882]);  $\log_{10} A = -14.025 \pm 0.380$ . **Diagnostics:** acceptance fraction 0.632; autocorrelation time  $\tau \approx 58$  samples/walker (mean over the two parameters); ESS  $\approx 5,500$ , computed as the total post-burn-in sample count divided by the mean autocorrelation time, ESS =  $(32 \times 10,000)/\tau = 320,000/58 \approx 5,500$  (the `emcee` convention without the factor-of-2 some ESS definitions include; production length  $> 50\tau$  per walker, convergence satisfied). Chain, posterior figure, and fitter script are deposited in the project data repository (GitHub: `Hubify-Projects/bigbounce`, path `pipelines/p3_pta_mcmc/free_spectrum_real_`

with  $k = 10$  neighbors on 50,000-sample runs) across 20 independent seeds; kNN-preservation and cross-seed Spearman FAIL as expected for sparse high-dimensional outlier clouds. Trustworthiness is the primary stability claim.

Full per-family DESI Legacy Survey DR9 grz composite image galleries (ten families, top-16 panels each,  $128 \times 128$  pixel cutouts at  $128 \times 0.262''/\text{px} = 33.5'' \times 33.5''$ ) are available at the project companion repository: <https://github.com/Hubify-Projects/bigbounce>. Figure 12 shows the top-1 representative per family.

#### Appendix E: PTA MCMC documentation: real KDE free-spectrum likelihood

Full MCMC provenance for the NANOGrav spectral-index analysis in §VA is documented here. **Dataset:** NANOGrav 15-yr HD-correlated KDE free-spectrum product (`30f_fs{hd}_ceffy1`), Zenodo 10.5281/zenodo.8060824 [18]. **Model:** matter-bounce power-law template

(2026-05-01/). Companion multi-PTA datasets (EPTA DR2 [26], PPTA DR3 [27]) independently report HD-correlated signals consistent with NANOGrav; multi-PTA joint chains are deferred to a dedicated PTA paper.

*a. NANOGrav Bayes-factor robustness under  $\gamma$ -prior variation.* The individual Savage-Dickey factors  $B_{\text{MB}/\text{free}}$  and  $B_{\text{SMBHB}/\text{free}}$  carry a prior-normalization dependence by construction (each is a ratio of posterior to flat-prior density at a fixed spectral index, and the prior density is  $1/\Delta\gamma$ ); the headline  $B_{\text{MB}/\text{SMBHB}} = 7.14 \times 10^3$  is their ratio, in which that normalization cancels. Table IX documents the robustness of both the individual factors and the headline ratio to the choice of  $\gamma$  prior width. In all cases the MCMC chain is re-weighted (no rerun required); because  $\gamma = 3.0$  and  $\gamma = 4.33$  both lie at or beyond the data-driven bulk  $\gamma \in [2.0, 3.5]$ , their posterior densities are nearly prior-independent under reweight-

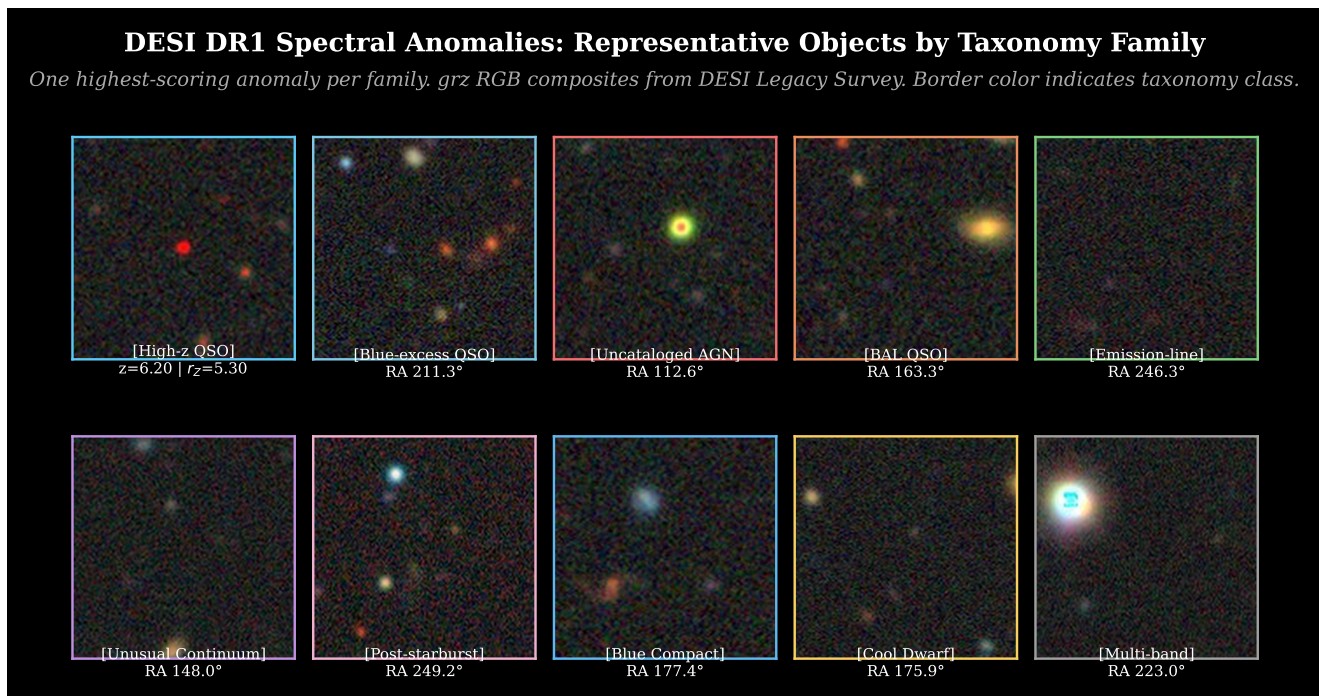


FIG. 12. **Representative DESI DR1 anomalies across all ten taxonomy families.** One highest-scored member per family; 2-row  $\times$  5-column layout. Border color indicates taxonomy class. Images are DESI Legacy Survey DR9 grz composites. Panel sublabeled give the object RA; the high- $z$  QSO panel additionally gives the redshift and the per-arm Z-arm sub-score  $r_z$  (§III B). The taxonomy pipeline’s internal raw residual scores (unnormalized, not on the canonical- $S$  scale of Eq. 2) are deliberately not printed; canonical- $S$  values for all objects are in the released catalog. Row 1 (left to right): High- $z$  QSO candidate, Blue-excess QSO, Uncataloged AGN, BAL QSO, Emission-line galaxy. Row 2: Unusual continuum (LRG), Post-starburst galaxy, Blue compact galaxy, Cool dwarf (the cool/unusual-star family; panel label “Cool Dwarf”), Multi-band unknown.

ing, so each individual  $B_{\gamma_{*}/\text{free}}$  simply tracks the prior-width factor through the flat-prior density  $1/\Delta\gamma$  (entries shrink modestly as the prior narrows). The headline ratio  $B_{\text{MB}/\text{SMBHB}}$ , in which that width factor cancels, is therefore essentially prior-independent and decisive across every prior choice.

*b. Bounce-physics connection.* The matter-bounce  $\gamma_{\text{GW}} = 3.0$  [19, 20] and  $f_{\text{NL}} = -35/8$  [14, 35] predictions are two observable consequences of the same contracting-phase mode-function calculation within the scalar-only  $w = 0$  matter-bounce class; within the broader bouncing-cosmology landscape (ekpyrotic,  $w \neq 0$  contraction, Cuscuton, quintom) the two observables decouple. A detection or null on either channel constrains the specific  $w = 0$  scenario, not the full bouncing-cosmology family (see §V).

#### Appendix F: ACT DR6 cross-transfer scan: quarantined methodological artifact

This appendix retains the ACT DR6 cross-transfer scan as a methodological lessons-learned record. ACT DR6 was scanned under the same cross-transfer CMB autoencoder later replaced by the Path-C native

Planck convolutional autoencoder (§III F); it was subsequently removed from the per-survey block (Table I) because the cross-transfer ACT block fails both gate criteria of §IID Step 1 and a Path-C-compliant native ACT retrain has not been executed. We describe the cross-transfer ACT scan here for two reasons only: (i) it provides the empirical evidence that the cross-transfer CMB autoencoder generalizes badly across instruments at very different angular resolution and noise statistics, and (ii) the Planck $\times$ ACT null cross-correlation reported independently in §IV D relies on the cross-transfer ACT anomaly set as its input.

*a. Scan parameters and result.* We applied the cross-transfer fully connected autoencoder used for SDSS, LAMOST, and Planck (32-dim latent space; cross-transfer training pool of 20,000 patches; see §III F) to 20,000  $64 \times 64$ -pixel patches from the ACT DR6 [9] CMB temperature map at HEALPix  $N_{\text{side}} = 256$ . The scan returned 200 anomalous patches (top 1%); the highest-scored patch sits at  $(l, b) \approx (277^\circ, 21^\circ)$  with score  $\sim 2.6 \times 10^7$ . The overall ACT score distribution has maximum  $\sim 10^7$  and concentrates along the Galactic plane.

*b. Why the gate fails.* The cross-transfer checkpoint has validation MSE  $\approx 2.2 \times 10^4$  on its native CMB training distribution, which exceeds Step-1 criterion (a) of

TABLE IX. NANOGrav Bayes-factor robustness under  $\gamma$ -prior sensitivity. Flat prior on  $\gamma$  over the stated range;  $\log_{10} A$  prior held fixed at  $[-18, -11]$ .  $B_{\text{MB}/\text{free}}$  and  $B_{\text{SMBHB}/\text{free}}$  are Savage-Dickey density ratios at  $\gamma = 3.0$  and  $\gamma = 4.33$  respectively. All quantities from the fiducial  $\gamma \in [0, 7]$  chain by prior re-weighting.

$\gamma$ prior range	$B_{\text{MB}/\text{free}}^{\text{a}}$	$B_{\text{SMBHB}/\text{free}}^{\text{b}}$	$B_{\text{MB}/\text{SMBHB}}$
$[0, 7]$ (fiducial)	3.23	$4.52 \times 10^{-4}$	$7.14 \times 10^3$
$[0, 5]$	2.31	$3.23 \times 10^{-4}$	$7.14 \times 10^3$
$[1, 6]$	2.31	$3.20 \times 10^{-4}$	$7.24 \times 10^3$
$[2, 5]$ (data-centered)	1.47	$1.69 \times 10^{-4}$	$8.69 \times 10^3$

Savage-Dickey density ratio:  $B = p(\gamma^*|\text{data})/p(\gamma^*|\text{prior})$ , where the denominator is the row-specific flat-prior density  $1/\Delta\gamma$  (e.g.,  $1/7 \approx 0.1429$  for  $\gamma \in [0, 7]$ ;  $1/5 = 0.2$  for  $\gamma \in [0, 5]$ ;  $1/5 = 0.2$  for  $\gamma \in [1, 6]$ ;  $1/3 \approx 0.333$  for  $\gamma \in [2, 5]$ ). Numerator obtained from a Gaussian KDE of the fiducial  $\gamma \in [0, 7]$  `emcee` chain evaluated at the test value (prior re-weighting; no chain rerun). The explicit computation for the fiducial row: at  $\gamma^* = 3.0$ : posterior KDE density  $\approx 0.461$ , giving  $B_{\text{MB}/\text{free}} = 0.461/(1/7) = 3.23$ . At  $\gamma^* = 4.33$ : posterior KDE density  $\approx 6.46 \times 10^{-5}$ , giving  $B_{\text{SMBHB}/\text{free}} = 6.46 \times 10^{-5}/(1/7) = 4.52 \times 10^{-4}$ . The ratio  $B_{\text{MB}/\text{SMBHB}} = 3.23/(4.52 \times 10^{-4}) = 7.14 \times 10^3$  follows directly. For non-fiducial prior rows, the prior density denominator changes accordingly; the prior re-weighting is exact for priors that are subsets of the fiducial  $[0, 7]$  range (tail posterior mass outside the subset is negligible for  $B_{\text{MB}/\text{free}}$  since  $\gamma = 3.0$  lies well within the data-driven bulk).

These are genuine Savage-Dickey density ratios, not posterior-tail fractions or  $p$ -values. See §E0 a. All rows:  $\gamma = 3.0$  ( $+1.13\sigma$  from posterior mean) remains favored against the free-spectrum alternative ( $B_{\text{MB}/\text{free}} \approx 1.5$ – $3.2$ , “substantial” on Jeffreys’ scale) and  $\gamma = 4.33$  strongly disfavored

( $B_{\text{SMBHB}/\text{free}} \approx 1.7$ – $4.5 \times 10^{-4}$ ) regardless of prior. Each individual  $B_{\gamma^*/\text{free}}$  tracks the prior width through the flat-prior density  $1/\Delta\gamma$  — the posterior density at both test points is bulk-stable under prior reweighting (recomputed from the committed  $\gamma \in [0, 7]$  chain restricted to each sub-prior;

`pipelines/p3_pta_mcmc/free_spectrum_real_2026-05-01/bf_prior_robustness.json`), so the entries shrink modestly as the prior narrows rather than swinging by orders of magnitude. The headline ratio  $B_{\text{MB}/\text{SMBHB}} = B_{\text{MB}/\text{free}}/B_{\text{SMBHB}/\text{free}} = p(3.0|\text{data})/p(4.33|\text{data})$  is prior-independent by construction — the  $1/\Delta\gamma$  width factor cancels — and stays decisive across every prior choice:  $B_{\text{MB}/\text{SMBHB}} \approx 7.1 \times 10^3$  for  $[0, 7]$  and  $[0, 5]$ ,  $7.2 \times 10^3$  for  $[1, 6]$ , and  $8.7 \times 10^3$  for the narrowest data-centered  $[2, 5]$ . The

$B_{\text{MB}/\text{SMBHB}}$  headline quoted in the text ( $7.14 \times 10^3$ ) uses the fiducial  $[0, 7]$  prior; no prior choice in the tested range weakens the “decisive” classification. The SMBHB environmental caveat (§V A) applies regardless of prior choice.

<sup>c</sup> a

§IID ( $\leq 0.30$ ) by a factor  $\sim 7 \times 10^4$ . The injection-recovery test (Step 5 of §IID; the same Gaussian-bump plant family used for the Planck native retrain) returns recovery fraction  $< 1\%$  at  $5\sigma$  amplitude, far below Step-1 criterion (b) ( $\geq 50\%$ ). Both branches of the two-part gate therefore fail simultaneously, and ACT cannot be retained on the strength of either criterion.

*c. Why no native ACT retrain.* A native ACT retrain—analogue to the Planck native convolutional autoencoder of §III F—requires a full ACT-native pre-processing pipeline (beam-deconvolved patches, ACT-specific point-source and Galactic mask, instrumental noise covariance) and was GPU-blocked at the time of submission. Because the present submission is the Path-C-final catalog and the Path-C protocol forbids retaining a survey on a checkpoint that fails both gate criteria, ACT DR6 is documented here only and contributes zero objects to the 377,482 Path-C unique-object headline. The with-ACT dedup variant, which would have produced  $387,895 - 10,213 = 377,682$  unique objects (a bookkeeping-only  $+200$  sensitivity variant relative to the headline, reflecting ACT’s zero positional overlaps with the other count-retained surveys), is preserved as a sensitivity-check artifact in the companion data repository.

*d. What this appendix is not.* This appendix is *not* an ACT science result. The 200-patch ACT cross-transfer set must not be cross-matched against optical/X-ray catalogs as if it were a science-grade anomaly catalog, must not be used as a tracer of CMB fluctuation statistics, and must not be interpreted as evidence of any astrophysical signal at the highlighted galactic-plane position. The retention of the cross-transfer scan is purely methodological: it documents the empirical failure mode of cross-transferring a 32-latent fully connected autoencoder trained on Planck SMICA data onto the ACT angular-resolution and noise regime, and motivates the architectural choice of the Planck native convolutional autoencoder.

- 
- [1] DESI Collaboration, “Data Release 1 of the Dark Energy Spectroscopic Instrument,” *Astron. J.* (accepted 2025), arXiv:2503.14745.
- [2] LAMOST Collaboration, “LAMOST Data Release 10 (v2.0),” <https://www.lamost.org/dr10/> (2023); survey description: X.-Q. Cui *et al.*, *Research in Astronomy and Astrophysics* **12**, 1197 (2012).
- [3] A. Almeida *et al.* (SDSS Collaboration), “The Eighteenth Data Release of the Sloan Digital Sky Survey: Targeting and Spectroscopy,” *Astrophys. J. Suppl. Ser.* **267**, 44 (2023).
- [4] A. Merloni *et al.*, “The SRG/eROSITA All-Sky Survey: The first X-ray all-sky survey in the 21st century,” *Astron. Astrophys.* **682**, A34 (2024).
- [5] Gaia Collaboration, “Gaia Data Release 3,” *Astron. Astrophys.* **674**, A1 (2023).
- [6] A. Mainzer *et al.*, “NEOWISE Reactivation Mission Year Ten,” *Planetary Science Journal*, 2024.
- [7] Planck Collaboration, “Planck 2018 results. I. Overview and the cosmological legacy of Planck,” *Astron. Astrophys.* **641**, A1 (2020).
- [8] Planck Collaboration, “Planck 2018 results. IX. Constraints on primordial non-Gaussianity,” *Astron. Astrophys.* **641**, A9 (2020).
- [9] F. J. Qu *et al.* (ACT Collaboration), “The Atacama Cosmology Telescope: A Measurement of the DR6 CMB Lensing Power Spectrum and Its Implications for Structure Growth,” *Astrophys. J.* **962**, 112 (2024), arXiv:2304.05202.
- [10] D. Baron and D. Poznanski, “The weirdest SDSS galaxies: results from an outlier detection algorithm,” *Mon. Not. Roy. Astron. Soc.* **465**, 4530 (2017).
- [11] Y. Liang *et al.*, “Outlier Detection in the DESI Bright Galaxy Survey,” *Astrophys. J. Lett.* **956**, L6 (2023), arXiv:2307.07664.
- [12] C. Nicolaou *et al.*, “Identifying Anomalous DESI Galaxy Spectra with a Variational Autoencoder,” *Mon. Not. Roy. Astron. Soc.* **547**, Issue 2 (2026), arXiv:2506.17376.
- [13] D. Wands, “Local non-Gaussianity from inflation,” *Class. Quant. Grav.* **27**, 124002 (2010).
- [14] Y.-F. Cai, W. Xue, R. Brandenberger, and X. Zhang, “Non-Gaussianity in a matter bounce,” *J. Cosmol. Astropart. Phys.* **0905**, 011 (2009), arXiv:0903.0631.
- [15] O. Doré *et al.* (SPHEREx Collaboration), “Cosmology with the SPHEREx All-Sky Spectral Survey,” arXiv:1412.4872 (2014).
- [16] U. Seljak, “Extracting Primordial Non-Gaussianity without Cosmic Variance,” *Phys. Rev. Lett.* **102**, 021302 (2009).
- [17] N. Hamaus, U. Seljak, and V. Desjacques, “Optimal constraints on local primordial non-Gaussianity from the two-point statistics of large-scale structure,” *Phys. Rev. D* **86**, 103513 (2012).
- [18] G. Agazie *et al.* (NANOGrav Collaboration), “The NANOGrav 15 yr Data Set: Evidence for a Gravitational-wave Background,” *Astrophys. J. Lett.* **951**, L8 (2023).
- [19] J. Quintin, Y. F. Cai, and R. H. Brandenberger, “Matter creation in a nonsingular bouncing cosmology,” *Phys. Rev. D* **90**, 063507 (2014).
- [20] Y.-F. Cai, “Exploring bouncing cosmologies with cosmological surveys,” *Sci. China Phys. Mech. Astron.* **57**, 1414 (2014).
- [21] A. Sesana, F. Shankar, M. Bernardi, and R. K. Sheth, “Selection bias in dynamically measured supermassive black hole samples,” *Mon. Not. Roy. Astron. Soc.* **463**, L6 (2016).
- [22] S. Burke-Spolaor *et al.*, “The astrophysics of nanohertz gravitational waves,” *Astron. Astrophys. Rev.* **27**, 5 (2019).
- [23] R. Trotta, “Bayes in the sky: Bayesian inference and model selection in cosmology,” *Contemp. Phys.* **49**, 71 (2008), arXiv:0803.4089.
- [24] L. Verde, P. Protopapas, and R. Jimenez, “Planck and the local universe: Quantifying the tension,” *Phys. Dark Univ.* **2**, 166 (2013), arXiv:1306.6766.
- [25] R. W. Hellings and G. S. Downs, “Upper limits on the isotropic gravitational radiation background from pulsar timing analysis,” *Astrophys. J. Lett.* **265**, L39 (1983).
- [26] J. Antoniadis *et al.* (EPTA Collaboration), “The second data release from the European Pulsar Timing Array: III. Search for gravitational wave signals,” *Astron. Astrophys.* **678**, A50 (2023), arXiv:2306.16214.
- [27] D. J. Reardon *et al.* (PPTA Collaboration), “Search for an isotropic gravitational-wave background with the Parkes Pulsar Timing Array,” *Astrophys. J. Lett.* **951**, L6 (2023), arXiv:2306.16215.
- [28] A. Afzal *et al.* (NANOGrav Collaboration), “The NANOGrav 15-year data set: Search for signals from new physics,” *Astrophys. J. Lett.* **951**, L11 (2023), arXiv:2306.16219.
- [29] E. S. Phinney, “A practical theorem on gravitational wave backgrounds,” arXiv:astro-ph/0108028 (2001).
- [30] M. Wenger *et al.*, “The SIMBAD astronomical database,” *Astron. Astrophys. Suppl. Ser.* **143**, 9 (2000).
- [31] L. McInnes, J. Healy, and J. Melville, “UMAP: Uniform Manifold Approximation and Projection for Dimension Reduction,” arXiv:1802.03426 (2018).
- [32] L. McInnes, J. Healy, and S. Astels, “hdbSCAN: Hierarchical density based clustering,” *J. Open Source Softw.* **2**, 205 (2017).
- [33] C. Heinrich, O. Doré, and E. Krause, “Measuring  $f_{NL}$  with the SPHEREx multitracer redshift-space bispectrum,” *Phys. Rev. D* **109**, 123511 (2024), arXiv:2311.13082 [astro-ph.CO].
- [34] M. Münchmeyer, M. S. Madhavacheril, S. Ferraro, M. C. Johnson, and K. M. Smith, “Constraining local non-Gaussianities with kinetic Sunyaev-Zel’dovich tomography,” *Phys. Rev. D* **100**, 083508 (2019), arXiv:1810.13424.
- [35] E. Wilson-Ewing, “The Matter Bounce Scenario in Loop Quantum Cosmology,” *JCAP* **1303**, 026 (2013), arXiv:1211.6269.
- [36] L. Lentati *et al.*, “Hyper-efficient model-independent Bayesian method for the analysis of pulsar timing data,” *Phys. Rev. D* **87**, 104021 (2013), arXiv:1210.3578.
- [37] D. Foreman-Mackey, D. W. Hogg, D. Lang, and J. Goodman, “emcee: The MCMC Hammer,” *Publ. Astron. Soc. Pac.* **125**, 306–312 (2013), arXiv:1202.3665 [astro-ph.IM].
- [38] J. Yoo, A. L. Fitzpatrick, and M. Zaldarriaga, “A New Perspective on Galaxy Clustering as a Cosmological

- Probe: General Relativistic Effects,” *Phys. Rev. D* **80**, 083514 (2009), arXiv:0907.0707 [astro-ph.CO].
- [39] C. Bonvin and R. Durrer, “What galaxy surveys really measure,” *Phys. Rev. D* **84**, 063505 (2011), arXiv:1105.5280 [astro-ph.CO].
- [40] A. Challinor and A. Lewis, “Linear power spectrum of observed source number counts,” *Phys. Rev. D* **84**, 043516 (2011), arXiv:1105.5292 [astro-ph.CO].
- [41] E. Di Dio, F. Montanari, J. Lesgourgues, and R. Durrer, “The CLASSgal code for relativistic cosmological large scale structure,” *J. Cosmol. Astropart. Phys.* **11**, 044 (2013), arXiv:1307.1459 [astro-ph.CO].